

point of the map, where $\text{II} = \text{III} = 0$, hence the anisotropy vanishes.

For the present analysis the trace on the invariant map along a constant radius $r^*/R_{pipe}^* = 0.95$ is shown in Fig. 77 for all four cases. For comparison the figures also show the state of turbulence for the unladen flow. In this case the flow in the pipe is axisymmetric and thus all data along the fixed radius are found at one (blue) point in the invariant map. The strongest changes of the state of turbulence for horizontal particle-laden pipe flows appears for the flow in the glass pipe at $\eta = 70\%$. As obvious in Fig. 77(c) the trace in the map is significantly extended and strongly tends towards the one-component limit. As already mentioned before, in the top part of the glass pipe the flow is not substantially altered by the particles because of their low concentration (see Fig. 75(c)). Consequently, the turbulent properties should be similar to the unladen flow which is confirmed by the invariant map shown in Fig. 77(c). Furthermore, the anisotropy of turbulence strongly increase by the influence of the particles on the continuous flow. The tendency to tend towards the one-component limit is typically found for relaminarizing flows and this observation is consistent with the low levels of the turbulent kinetic energy k found in the bottom part of the glass pipe (see Fig. 76(c)). In this case the dominant component of the Reynolds stress tensor is $\langle u_{fz}' u_{fz}' \rangle / U_B^{*2}$, i.e., the fluctuations in streamwise direction being at least one order of magnitude higher than all other components of the tensor. This specific region of the map is highly interesting for drag reduction investigations (see, e.g., Frohnafel et al., 2007). Moving down the side wall the trace of the map approaches the two-component limit, which is typical for the near-wall region, where the wall-normal fluctuations decrease faster compared with the fluctuations in the other two directions. This supports the observation made above of a partially relaminarized boundary layer in the bottom part: At the same distance from the wall the flow in the lower part has a near-wall behavior. On the other hand, in the top part the turbulence shows a behavior typical for buffer layers, where the trace of the invariant map is found near the axisymmetric border (see, e.g., Frohnafel et al., 2007). That means that the boundary layer at the same radial position near the bottom is much thicker than at the top. Compared with the glass pipe the modifications of turbulence in the steel pipe (Fig. 77(d)) at the same mass loading are qualitatively similar but much less pronounced. Regarding the dependency from the mass loading η it is obvious that the changes induced by the presence of the particles in the anisotropy map at constant radius are less pronounced for the lower mass loading than for the higher mass loading (compare Fig. 77(a) with (c) and Fig. 77(b) with (d)). These observations are consistent with the smaller modifications of the other quantities (e.g., $\langle u_{f\theta}' u_{f\theta}' \rangle / U_B^{*2}$ or k) studied before and the lower strength of the resulting secondary flow.

Pressure Distribution

For completeness, Fig. 78 shows the mean pressure $\langle p \rangle = \langle p^* \rangle / \rho_f^* U_B^{*2}$ for the glass (Figs. 78(a) and (c)) and the steel pipe (Fig. 78(b) and (d)). It is evident that for all four cases the contribution by the negative gradient of the circumferential Reynolds stress near the wall is partially balanced by a positive pressure gradient. However, the sum leads anyway to a net contribution of the driving forces in circumferential direction as will be shown by a more detailed analysis in the following section. Note that the positive circumferential direction is defined here in clockwise direction, i.e., in the direction of the secondary flow along the wall for the right part of the pipe. For the four cases considered the maximum pressure is observed near the concentration maximum (see Fig. 75(a)–(d))

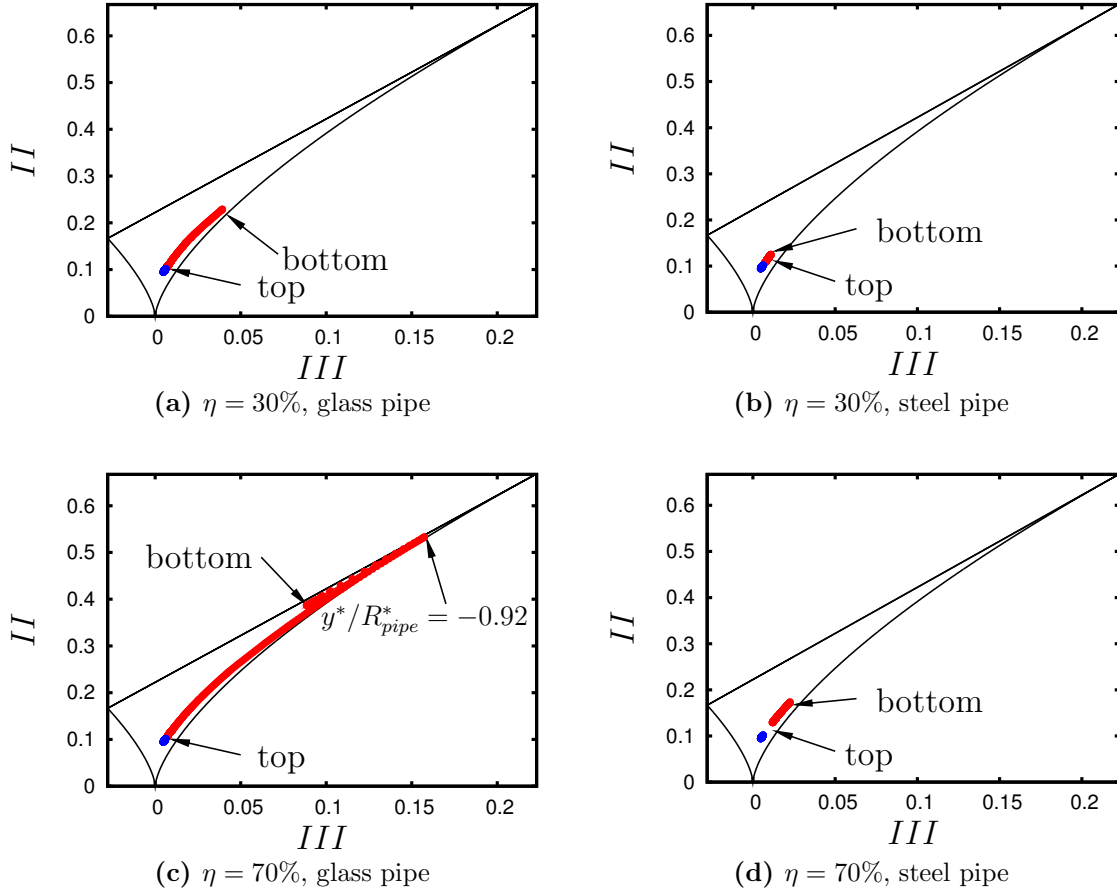


Figure 77: Invariant mapping along the constant radial coordinate $r^*/R_{pipe}^* = 0.95$, data of the particle-laden flow in red, data of the unladen flow (for comparison) in blue, poly-disperse particles for both pipes and two mass loadings.

and therefore also near the region in the pipe cross-section with the highest turbulence attenuation. That means that for the glass pipes (Fig. 78(a) and (c)) the maximum pressure is located at the bottom of the pipe leading to a pressure gradient along the wall against the gravitational acceleration. With respect to the symmetry plane the negative pressure gradient acts in the direction of the secondary flow. Furthermore, it is noticeable that for the glass pipe the maximum pressure increases with increasing mass loading. For the steel pipe (Figs. 78(b) and (d)) on the other hand, the maximum pressure is located near the pipe center, i.e., near the symmetry plane the pressure has a decelerating effect in the lower half of the pipe and an accelerating effect in the upper half. In contrary to the glass pipe, for the steel pipe the maximum pressure does not increase with increasing mass loading but has similar values for both cases. Unfortunately, no comprehensive explanation for this observation can be given. However, the maximum pressure seems to be correlated with the degree of turbulence attenuation. For the glass pipe (especially for the $\eta = 70\%$ case) a strong turbulence attenuation can be observed at the bottom of the pipe leading to almost vanishing turbulence fluctuations in this region (see Fig. 74(c) and also Fig. 76(c)). Therefore, a strong reduction of the turbulence fluctuations in comparison with the unladen flow can be observed. For the lower mass loading computed for the glass pipe, the turbulence attenuation (see Fig. 74(a) and also Fig. 76(a)) is smaller than

for the $\eta = 70\%$ case and therefore also the pressure is smaller. For the steel pipe the particles concentration shows a maximum near the pipe center, i.e., in the region where the turbulence fluctuations for the unladen flow have a minimum. Therefore, in contrast to the glass pipe, no big difference between the $\eta = 30\%$ and $\eta = 70\%$ case regarding the degree of turbulence attenuation provoked by the particles can be observed. For this reason no big difference between the two cases regarding the maximum pressure can be noticed.

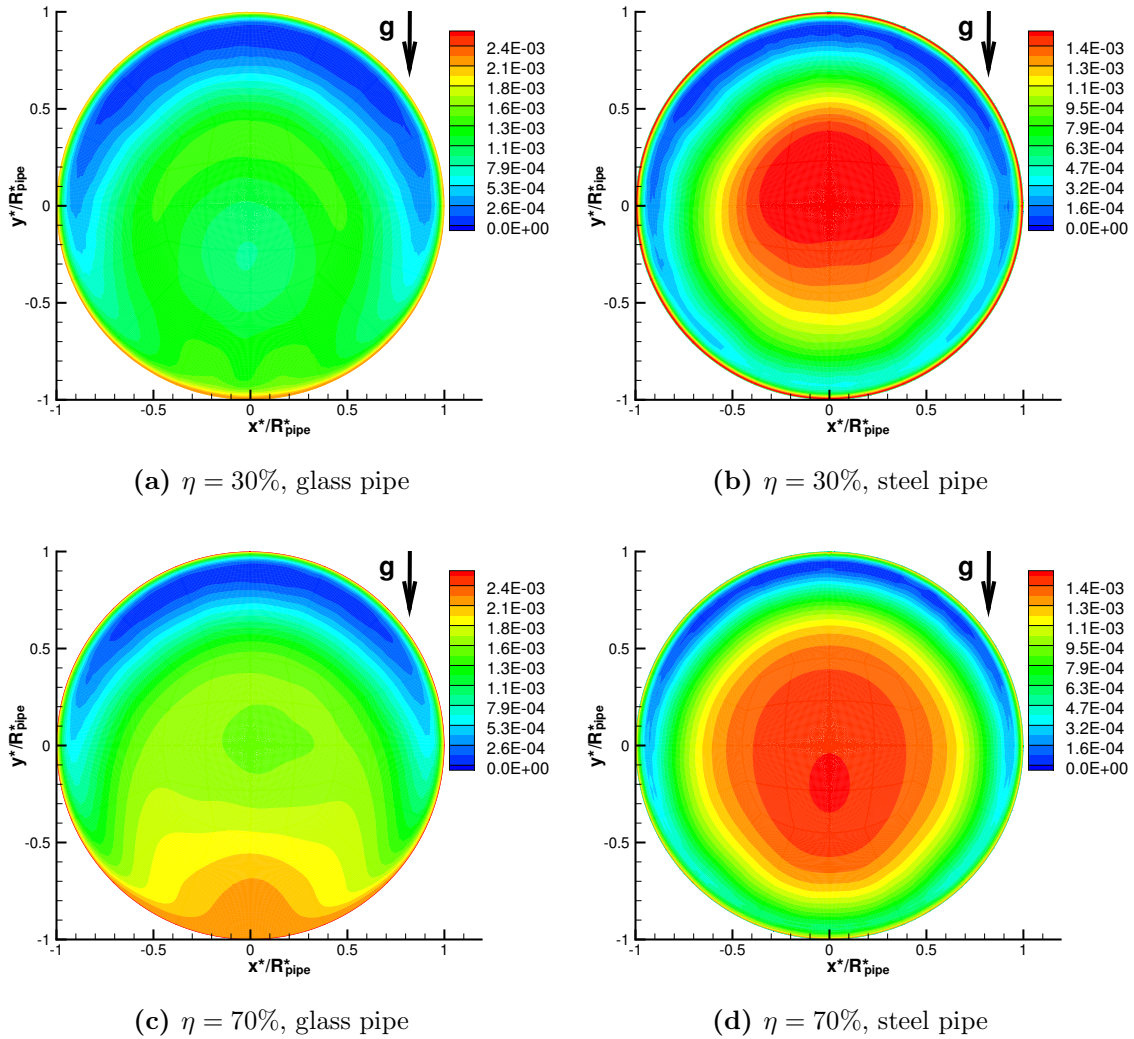


Figure 78: Contours of the mean pressure $\langle p^* \rangle / \rho_f^* U_B^{*2}$, poly-disperse particles for both pipes and two mass loadings.

8.6.4.2 Quantitative Analysis

In order to quantify the driving mechanisms pushing the flow along the pipe walls, the filtered velocity field \tilde{u}_{fi} predicted by LES is decomposed according to Reynolds in a time-averaged value $\langle \tilde{u}_{fi} \rangle$ and the superimposed turbulent fluctuations u'_{fi} : $\tilde{u}_{fi} = \langle \tilde{u}_{fi} \rangle + u'_{fi}$. The resulting velocity field is casted into the LES equations and after time-averaging (the time-averaging operation is denoted by the brackets $\langle \dots \rangle$) the Reynolds-averaged equation of motion in circumferential direction are obtained. Assuming that the resolved flow field

contains the major part of the turbulent spectrum, the subgrid-scale contributions can be neglected for this rough analysis leading to the following dimensionless equation:

$$\begin{aligned} \langle \tilde{u}_r \rangle \frac{\partial \langle \tilde{u}_\theta \rangle}{\partial r} + \frac{\langle \tilde{u}_\theta \rangle}{r} \frac{\partial \langle \tilde{u}_\theta \rangle}{\partial \theta} + \frac{\langle \tilde{u}_r \rangle \langle \tilde{u}_\theta \rangle}{r} = -\frac{1}{r} \frac{\partial \langle \tilde{p} \rangle}{\partial \theta} + \\ \frac{1}{\text{Re}} \left[\frac{1}{r} \frac{\partial}{\partial r} \left(r \frac{\partial \langle \tilde{u}_\theta \rangle}{\partial r} \right) + \frac{1}{r^2} \frac{\partial^2 \langle \tilde{u}_\theta \rangle}{\partial \theta^2} + \frac{2}{r^2} \frac{\partial \langle \tilde{u}_r \rangle}{\partial \theta} - \frac{\langle \tilde{u}_\theta \rangle}{r^2} \right] \\ - \frac{\partial \langle u'_r u'_\theta \rangle}{\partial r} - \frac{1}{r} \frac{\partial \langle u'_\theta u'_\theta \rangle}{\partial \theta} - \frac{2 \langle u'_r u'_\theta \rangle}{r} - \langle F_{pf\theta} \rangle \end{aligned} \quad (8.10)$$

Note that the derivatives in axial direction are omitted a-priori since they are equal to zero because of the homogeneity of the flow and the resulting spatial averaging in this direction. To estimate the driving forces leading to the secondary flow, the above equation is evaluated in a radial slice parallel to the pipe wall ranging from $r_1^*/R_{pipe}^* = 0.91$ ($\Delta r^+ = 210$ based on the skin friction velocity of the unladen flow) to $r_2^*/R_{pipe}^* = 0.98$ ($\Delta r^+ = 51$). By this way the effect of the viscous forces can be neglected since the outer border of the slice is clearly outside of the viscous sublayer. Furthermore, by analyzing the averaged data it turns out that $2 \langle u'_r u'_\theta \rangle / U_B^{*2}$ is of the order $\mathcal{O}(10^{-5})$ and hence, can also be neglected with respect to $\partial \langle u'_\theta u'_\theta \rangle / \partial \theta = 1/U_B^{*2} \partial \langle u'_\theta u'_\theta \rangle / \partial \theta$ (see Fig. 74(c) and (d)). The derivative $\partial \langle u'_r u'_\theta \rangle / \partial r$ is retained since it cannot be neglected a-priori. Hence, the above equation can be simplified to:

$$\langle \tilde{u}_r \rangle \frac{\partial \langle \tilde{u}_\theta \rangle}{\partial r} + \frac{\langle \tilde{u}_\theta \rangle}{r} \frac{\partial \langle \tilde{u}_\theta \rangle}{\partial \theta} + \frac{\langle \tilde{u}_r \rangle \langle \tilde{u}_\theta \rangle}{r} = -\frac{1}{r} \frac{\partial \langle \tilde{p} \rangle}{\partial \theta} - \frac{\partial \langle u'_r u'_\theta \rangle}{\partial r} - \frac{1}{r} \frac{\partial \langle u'_\theta u'_\theta \rangle}{\partial \theta} - F_{pf\theta} \quad (8.11)$$

To get smoother data, we integrate the above equation with respect to θ :

$$\begin{aligned} \int_0^\theta \left(\langle \tilde{u}_r \rangle \frac{\partial \langle \tilde{u}_\theta \rangle}{\partial r} + \frac{\langle \tilde{u}_\theta \rangle}{r} \frac{\partial \langle \tilde{u}_\theta \rangle}{\partial \theta} + \frac{\langle \tilde{u}_r \rangle \langle \tilde{u}_\theta \rangle}{r} \right) d\theta = \underbrace{-\frac{1}{r} \left(\langle \tilde{p} \rangle(\theta) - \langle \tilde{p} \rangle(0) \right)}_{\mathbf{P}} \\ - \underbrace{\int_0^\theta \frac{\partial \langle u'_r u'_\theta \rangle}{\partial r} d\theta}_{\mathbf{UR}\Theta} - \underbrace{\frac{1}{r} \left(\langle u'_\theta u'_\theta \rangle(\theta) - \langle u'_\theta u'_\theta \rangle(0) \right)}_{\mathbf{UU}} - \underbrace{\int_0^\theta F_{pf\theta} d\theta}_{\mathbf{FP}} \end{aligned} \quad (8.12)$$

Note that as mentioned before the positive circumferential direction is defined in clockwise direction starting from the top of the pipe. Since derivatives cannot be disregarded a-priori the computation of the first derivative of the shear stress $\partial \langle u'_r u'_\theta \rangle / \partial r$ was performed by means of a central difference scheme. To integrate the particle force and the derivative of the shear stress $\partial \langle u'_r u'_\theta \rangle / \partial r$ the trapezoidal rule was applied.

Figure 79 shows the terms of the right-hand side of eq. (8.12) for the glass (Figs. 79(a) and (c)) and the steel pipe (Figs. 79(b) and (d)). For the steel pipe the terms at the right-hand side of eq. (8.12) are multiplied by a factor of 2 in order to use the same scaling as for the glass pipe. Comparing the glass with the steel pipes it is evident that (i) the gradient of the circumferential Reynolds stress **UU** forces the flow in circumferential direction, (ii) the pressure gradient **P** partially balances this effect, (iii) the particles and the gradient of the shear stress $\partial \langle u'_r u'_\theta \rangle / \partial r$ exert a force against the direction of the secondary flow but the effect is almost negligible and (iv) the sum of the four effects leads to a net contribution in circumferential direction. Note that the sum of the right-hand

side of eq. (8.12) for the glass pipes is approximately doubled compared with the steel pipes explaining the difference in the magnitude of the secondary flow between both cases. Furthermore, comparing Fig. 79(a) with (c) it can be observed that the sum of the terms on the right-hand side of eq. (8.12) are similar in magnitude for the flow in the glass pipe at different mass loadings. This is consistent with the observation that the intensity of the secondary flow is similar in the two glass pipes considered (see Figs. 72(a) and (c)). An analogous observation can be made regarding the flow in the steel pipe at $\eta = 30\%$ and 70% . A further observation which can be made by comparing the main forces driving the secondary flow at the walls consisting of the same material but different mass loading, is that the pressure \mathbf{P} behaves inversely proportional to the integral of the Reynolds stress in circumferential direction \mathbf{UU} . For the low mass loadings (see Fig. 72(a) and (b)) \mathbf{UU} does not increase as rapidly as for the intermediate mass loading (see Fig. 72(c) and (d)). The reason is that the turbulence attenuation for $\eta = 30\%$ is not as pronounced as for $\eta = 70\%$. In conclusion, the wall roughness drastically changes the particle distribution in the cross-section. Consequently, the anisotropy of the Reynolds stress is reduced and thus a weakened secondary flow of second kind is observed for the rough pipe compared with the smooth pipe.

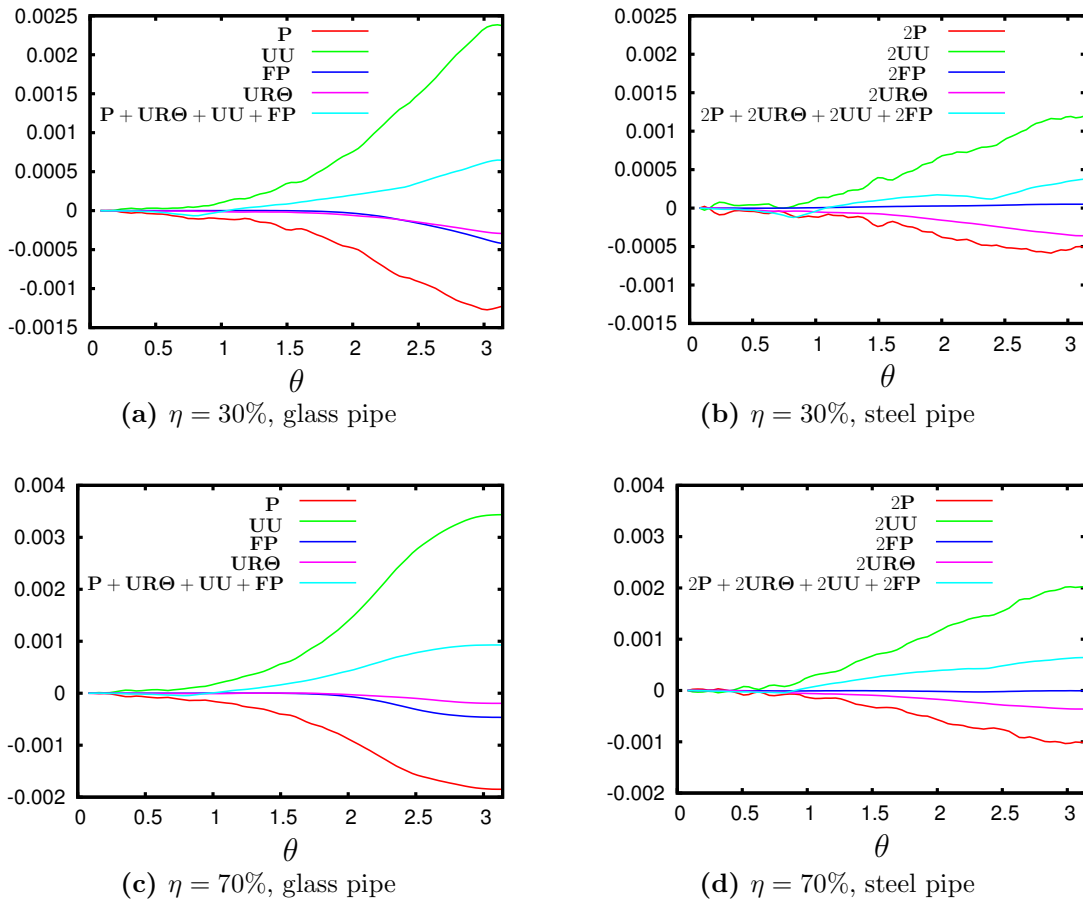


Figure 79: Quantitative analysis of the driving forces in circumferential direction for both pipes and both mass loadings.

8.6.5 Comparison with the Literature

Concerning experimental studies, unfortunately, no investigations reported explicitly the existence of a secondary flow in the cross-section of a particle-laden pipe flow. Very recently, however, Belt et al. (2012) performed LDA measurements of water flow in a vertical Plexiglas pipe with a diameter of 50 mm. The peculiarity was that at the bottom half of the pipe three layers of spheres separated from each other by 10 mm with a sphere diameter of 1 mm were fixed in a staggered arrangement along the entire pipe length. The objective was to mimic the effect of the increased particle concentration at the bottom of a horizontal pipe under the influence of gravity. Two different Reynolds numbers, $Re = 5494$ and $10,864$, were investigated. The pipe had a length of 120 diameters before the measurement section to ensure a fully developed flow and a length of 40 diameters after the measurement section to avoid exit effects. The main outcome was that for both Re two elongated secondary flow regions at the bottom part and two much smaller ones with a very low intensity at the top part of the pipe developed. The intensity of the cross-sectional flow increased with increasing Re and reached about 9% of the bulk velocity in case of the high Reynolds number. Belt et al. (2012) attributed the presence of the secondary flow to the particle-induced changes of the turbulent flow. In case of inhomogeneously distributed particles observed for horizontal pipe flows these changes lead to an anisotropy in the Reynolds stresses in the cross-section causing the secondary flow, i.e., a secondary flow of second kind is approved. In the present study an intensity of about 2% of the bulk velocity is found for the glass pipe and of about 1% for the steel pipe. Despite the differences in the setup between the study of Belt et al. (2012) and the present research, the overall structure and the direction of the secondary flow near the pipe wall is found to agree well between both investigations. Furthermore, in both studies the secondary flow coincides with the negative gradient of the circumferential Reynolds stress $\langle u_{f\theta}' u_{f\theta}' \rangle / U_B^{*2}$. However, it is worth to mention that in Belt et al. (2012) the gradient of the circumferential Reynolds stress $\langle u_{f\theta}' u_{f\theta}' \rangle / U_B^{*2}$ along the sidewall was much more pronounced than in the present work explaining the higher magnitude of the secondary flow. Hence, both observations concerning the flow direction and the gradient of $\langle u_{f\theta}' u_{f\theta}' \rangle / U_B^{*2}$ give a clear hint that the physical mechanism responsible for the circulation in the pipe cross-section is the same.

A similar structure of the secondary flow, i.e., the flow moves upwards at the symmetry plane and downwards at the walls, was also found in the RANS prediction of a rough steel pipe with a mass loading of 30% and the same poly-disperse particle distribution as described in § 7.6 performed by Huber and Sommerfeld (1998). In contrast to the present study, no secondary flow in the pipe cross-section was detected by Huber and Sommerfeld (1998) in their smooth glass pipe simulations at the same mass loading. The intensity of the secondary flow in the case of the steel pipe was about 3% of the bulk velocity and hence tripled with respect to the same setup of the present simulation. Differences to the present simulation can also be found in the explanation of the occurrence of the secondary flow, i.e., Huber and Sommerfeld (1998) argued that the particles push the flow upwards because of the difference between the top and bottom wall of the wall-normal momentum transferred by the particles to the fluid. Hence, the explanation of the driving mechanism of the secondary flow given by Huber and Sommerfeld (1998) is completely different to the mechanism found in Belt et al. (2012) and in the present work, i.e., that the origin of the secondary flow is the gradient of the circumferential Reynolds stress arising between the bottom and the top wall. The aforementioned discrepancies are difficult to explain,

especially since in the present work it is found that the particles have a decelerating effect on the steady vortex developing in the pipe cross-section.

Lain and Sommerfeld (2012) recently obtained in their two-way coupled RANS simulations two circulation cells symmetric about the midplane. In their four-way coupled simulation Lain and Sommerfeld (2012) reported a four-cell structured secondary flow symmetric about the midplane and the plane perpendicular to the gravitational acceleration almost cutting the pipe center. The intensity of the cross-sectional flow increased with increasing wall roughness and was about 0.2% for a standard deviation of the wall inclination of $\Delta\gamma = 0.8^\circ$ and about 0.3% for $\Delta\gamma = 5.0^\circ$. However, compared to the study of Huber and Sommerfeld (1998) and the present work, the predictions of Lain and Sommerfeld (2012) were carried out for rather large inertial mono-sized particles and for a higher mass loading of $\eta = 100\%$. In order to compare the present methodology with the results of Lain and Sommerfeld (2012) and to investigate whether it is possible to achieve a secondary flow of first kind, supplementary four-way coupled simulations with particles ($d_p^* = 134 \mu\text{m}$ and $\eta = 100\%$) hitting two different rough surfaces were performed. (For the setup see § 7.6.) The secondary flow structures developing in the pipe cross-section are shown in Figs. 80(a)–(b). It is obvious that for both roughnesses investigated only one symmetry plane can be observed and hence the picture of the flow is in striking difference to the one observed by Lain and Sommerfeld (2012). Furthermore, the same analysis about the direction of the force exerted by the particles on the fluid as carried out in the previous section, was performed and it can be concluded that the driving force is still the anisotropy of the Reynolds stress tensor even for the high roughness. Furthermore, the intensity of the cross-sectional flow decreases with increasing roughness and is approximately equal to 0.2% of the bulk velocity for the lower roughness (see Fig. 80(a)) and about 0.1% of the bulk velocity for the higher roughness (see Fig. 80(b)). Thus the intensity of the cross-sectional flow has an opposite dependence on the roughness than in the studies performed by Lain and Sommerfeld (2012). The trend observed in the present simulations is in line with the findings made in in the previous section. For increasing roughness the particles are more affected by rough-surface collisions and hence the gravity plays a minor role. Therefore, the particle concentration shows an almost axisymmetric distribution. This becomes clear by comparing the particle concentrations for $k_s^* = 30 \mu\text{m}$ (see Fig. 80(c)) with the particle concentration for $k_s^* = 150 \mu\text{m}$ (see Fig. 80(d)). It is obvious that for increasing surface roughness the concentration profile shows a more homogeneous distribution and becomes almost axisymmetric. Furthermore, it is evident that bigger particles hitting the same rough surface are less influenced by the gravity than smaller particles (compare Fig. 80(c) with 75(b) or (d)). Due to the almost axisymmetric distribution of the particles the turbulence is almost equally affected along a constant radius and the gradient of the circumferential Reynolds stress $\langle u_{f\theta}' u_{f\theta}' \rangle / U_B^{*2}$ in circumferential direction almost vanishes (see Figs. 80(e)–(f)). That explains why the strength of the secondary flow in the rough steel pipe ($k_s^* = 30 \mu\text{m}$) reduces from about 1% of the bulk velocity to about 0.2% of U_B^* for the large mono-disperse particles. In case of even higher wall roughness ($k_s^* = 150 \mu\text{m}$) the secondary flow almost vanishes completely for the mono-disperse particles. Summing up, the present simulations delivers quite different results, both concerning the origin of the secondary flow and concerning its pattern, compared with the study by Lain and Sommerfeld (2012). The discrepancies remain difficult to explain.

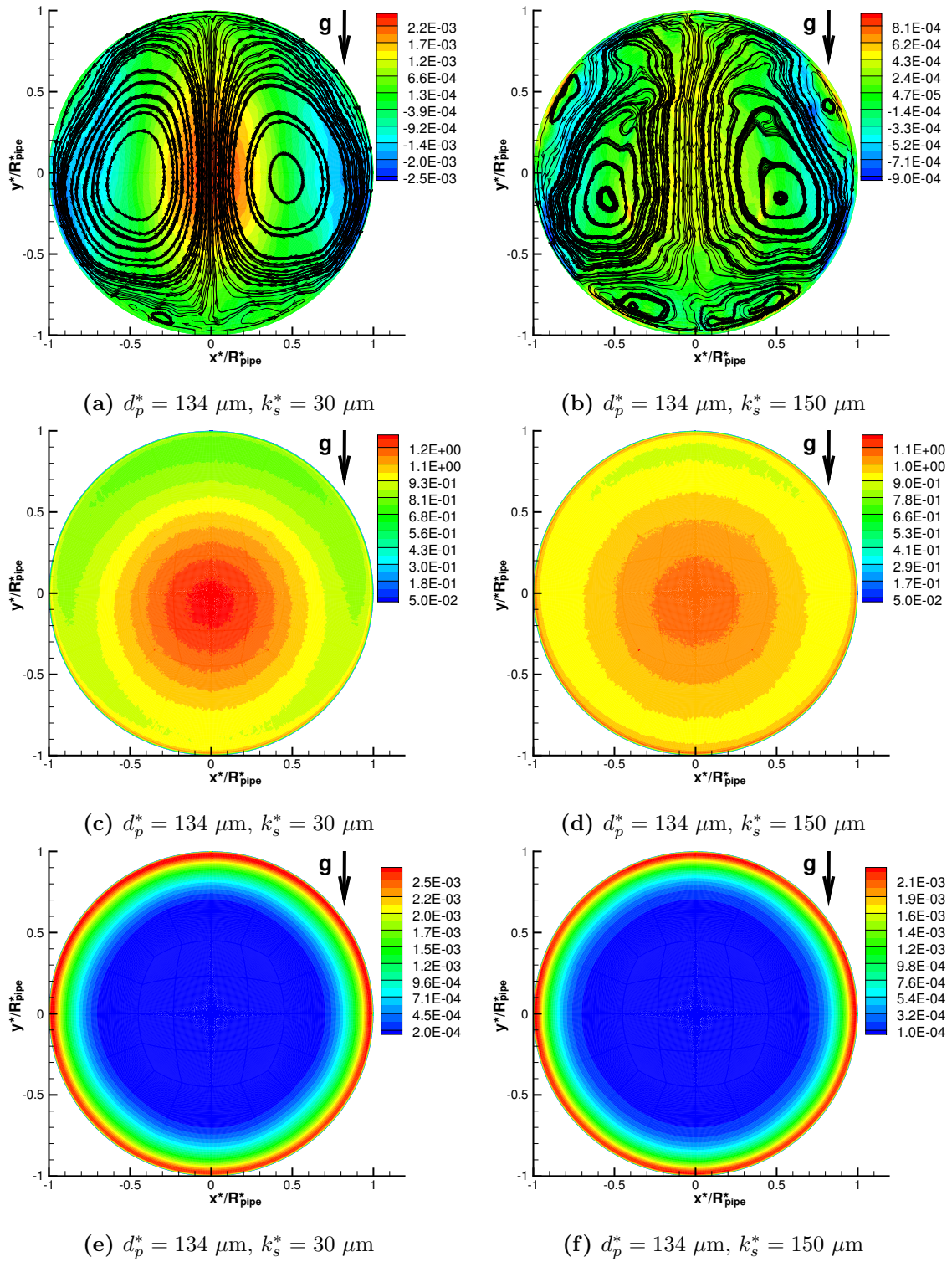


Figure 80: Influence of the wall roughness seen by the particles on (a)-(b) the projected streamlines and the fluid velocity component $\langle u_{fy}^* \rangle / U_B^*$ against the gravitational acceleration (averaged flow), (c)-(d) the mean particle concentration and (e)-(f) the circumferential Reynolds stress $\langle u_{f\theta}^* u_{f\theta}^* \rangle / U_B^{*2}$, mono-disperse distribution.

8.6.6 Summary and Conclusions

Secondary flow structures in turbulent flows through horizontal pipes with circular cross-sections were investigated numerically based on large-eddy simulation and an Euler-Lagrange approach. The objective was to prove whether the particle-driven secondary flow is of first or second kind and to isolate the most important physical contributions. In order to validate the numerical tool and to achieve confidence in the results, first the unladen turbulent flow was checked based on cross-comparisons with experimental and DNS data. In the second step a particle-laden flow through a glass and a steel pipe were predicted and compared with the experimental measurements of Huber (1997) and Huber and Sommerfeld (1998). All results were found to be in good agreement with the reference data. Thus the analysis of the secondary flow structures was carried out for poly-disperse particle with two different mass loadings and both, a smooth (glass) and a rough (steel) surface. Furthermore, the flow with rather inertial mono-disperse particles at a mass loading of $\eta = 100\%$ hitting two different rough surfaces was additionally analyzed for a direct comparison with RANS predictions from the literature.

The main results of this study are:

- A two-cell secondary flow structure symmetric to the midplane is observed for all cases studied.
- An analysis of the drag forces exerted by the particles on the flow yields the finding that the secondary flow of the continuous phase is not driven by the particles, but the particles are pushed by the fluid flow. Thus, a secondary flow of first kind can be excluded in the present cases.
- The strongly inhomogeneous particle distribution when rather small particles hit a smooth or rough surface leads to major variations of the Reynolds stresses. Especially, the circumferential Reynolds stress varies significantly in circumferential direction.
- Analyzing the Reynolds-averaged Navier-Stokes equation in circumferential direction identifies three main driving contributions, the circumferential gradient of the circumferential Reynolds stress $\partial\langle u'_\theta u'_\theta \rangle / \partial\theta$, the circumferential pressure gradient $\partial\langle p \rangle / \partial\theta$ and the forces exerted by the particles. The first contribution has the largest magnitude and is directed in the direction of the secondary flow observed. The second contribution, i.e., the pressure gradient in circumferential direction partially balances the gradient of the Reynolds stress in circumferential direction. Furthermore, it is found by analyzing the pipe flow at different mass loadings that $\partial\langle p \rangle / \partial\theta$ is proportional to $\partial\langle u'_\theta u'_\theta \rangle / \partial\theta$. However, since the absolute values of the sum of the pressure gradient and the force exerted by the particles on the fluid are smaller in magnitude than the gradient of the circumferential Reynolds stress and directed against the secondary flow, the circumferential Reynolds stress is clearly identified as the driving mechanism.
- The magnitude of the secondary flow velocity in the glass pipe is about 2% of the bulk velocity for the low and medium mass loading for the poly-disperse particle size distribution. Furthermore, the wall roughness has a significant effect leading to a more homogeneous distribution of the particle concentration. That reduces the gradients of the Reynolds stresses in the cross-section and consequently the

anisotropy of the Reynolds stresses. For this reason the magnitude of the secondary flow decreases to about 1% of the bulk velocity in the steel pipe.

- In comparison with the results found by Belt et al. (2012) for fixed particles and two much lower Reynolds numbers (up to 9 % of the bulk velocity), the magnitude of the secondary flow velocity in the present case is significantly smaller. However, in both studies the direction of the secondary flow at the wall coincides with the direction of the negative gradient of the circumferential Reynolds stress $\langle u_{f\theta}' u_{f\theta}' \rangle / U_B^{*2}$. The higher magnitude of the secondary flow found in the experimental setup with fixed particles can be explained by the higher gradient of $\langle u_{f\theta}' u_{f\theta}' \rangle / U_B^{*2}$ at the wall measured by Belt et al. (2012).
- Contrary to the investigations of Huber and Sommerfeld (1998) and Lain and Sommerfeld (2012) no evidence for the appearance of a secondary flow of first kind, i.e., where the particles pushing the flow inducing a secondary motion of the fluid, can be found. This statement is also affirmed for rather large inertial particles hitting quite rough surfaces of different roughnesses. Thus a discrepancies in the results remained which could not be resolved.

8.7 Cold Flow in a Combustion Chamber Model

This section shows the results obtained from the particle-laden flow simulation from the combustion chamber model. This section is organized as follows: First, the influence of the coupling assumption is analyzed in detail on a coarser grid in § 8.7.1. The results are compared and validated by means of the experiment of Borée et al. (2001). Furthermore, in this section also the influence of the particle diameter on the particle statistics is analyzed and a physical explanation for the minor importance of the four-way coupling even for the high mass loading $\eta = 110\%$ is given. After that, in § 8.7.2 the influence of the resolution and the inflow boundary conditions is studied. Finally, conclusions regarding the flow in the combustion chamber model are drawn in § 8.7.3. Note that a part of the results presented here were already published by the author in Alletto and Breuer (2012), Breuer and Alletto (2012a,b).

8.7.1 Influence of the One-, Two- and Four-Way Coupling

8.7.1.1 Overview of the Flow Structure

In order to provide a first overview on the general flow structure, Fig. 81 depicts the streamlines of the averaged continuous fluid flow for the four-way coupled simulations, the contour plots of the radial velocity fluctuations $\langle u_{fr}^{*'} \rangle_{rms} / U_{jet}^*$, the averaged particle paths for particles with a diameter of $d_p^* = 60 \mu\text{m}$ and the mean volume fraction Φ of the particles at both mass loadings $\eta = 22\%$ and 110% . Note that the measurement planes where the simulations are later compared with the experiments of Borée et al. (2001) are visualized as red dashed lines. The path lines are obtained by averaging the particle statistics of different particle classes separately in time and in circumferential direction. Based on the averaged velocities of the particles belonging to the same class, the path lines in a cross-section can be displayed. No big differences between the one-, two- and four-way coupled cases for the moderate mass loading and the two- and four-way coupled cases for the high mass loading can be observed. Therefore, Figs. 81(a) and (b) provide an illustration of how the momentum additionally injected by the particles changes the mean continuous fluid flow in the combustion chamber.

As visible in Figs. 81(a) and (b), due to the central jet J a second counter-clockwise rotating recirculation region R2 is formed inside the wake characterized by a clockwise rotating recirculation R1 generated by the sudden expansion of the annular flow A. In the case of the moderate mass loading the momentum injected by the central jet is not high enough to penetrate through the recirculation region R1. Thus, the first stagnation point S1 is formed located at $z^*/R_{pipe}^* = 12.56$ and 13.99 for the unladen and the M4 case, respectively. The same flow structure is found in combustion devices where the central fuel jet is not able to overcome the bluff-body recirculation region leading to a recirculation type flame (Chen et al., 1990, 1998b). In this case the main combustion occurs in the recirculation bubble. As pointed out by Namazian et al. (1989) the location of the first stagnation point S1 depends on the normalized momentum-flux ratio $M_{jet}^*/M_e^* = (U_{jet}^*/U_e^*)^2 \cdot (\rho_{jet}^*/\rho_e^*)$. To allow a comparison of the location of S1 with experiments available in the literature, for the present simulation this quantity is estimated as follows: $M_{jet}^*/M_e^* \approx (U_{jet}^*/U_e^*)^2 \cdot (1 + \eta)$. The values corresponding to the unladen case, the moderate mass loading case and the high mass loading case are 0.31, 0.38 and 0.66, respectively. A direct analogy with the single-phase flow is, however, only possible for fully responsive particles whose characteristic time of momentum exchange is much

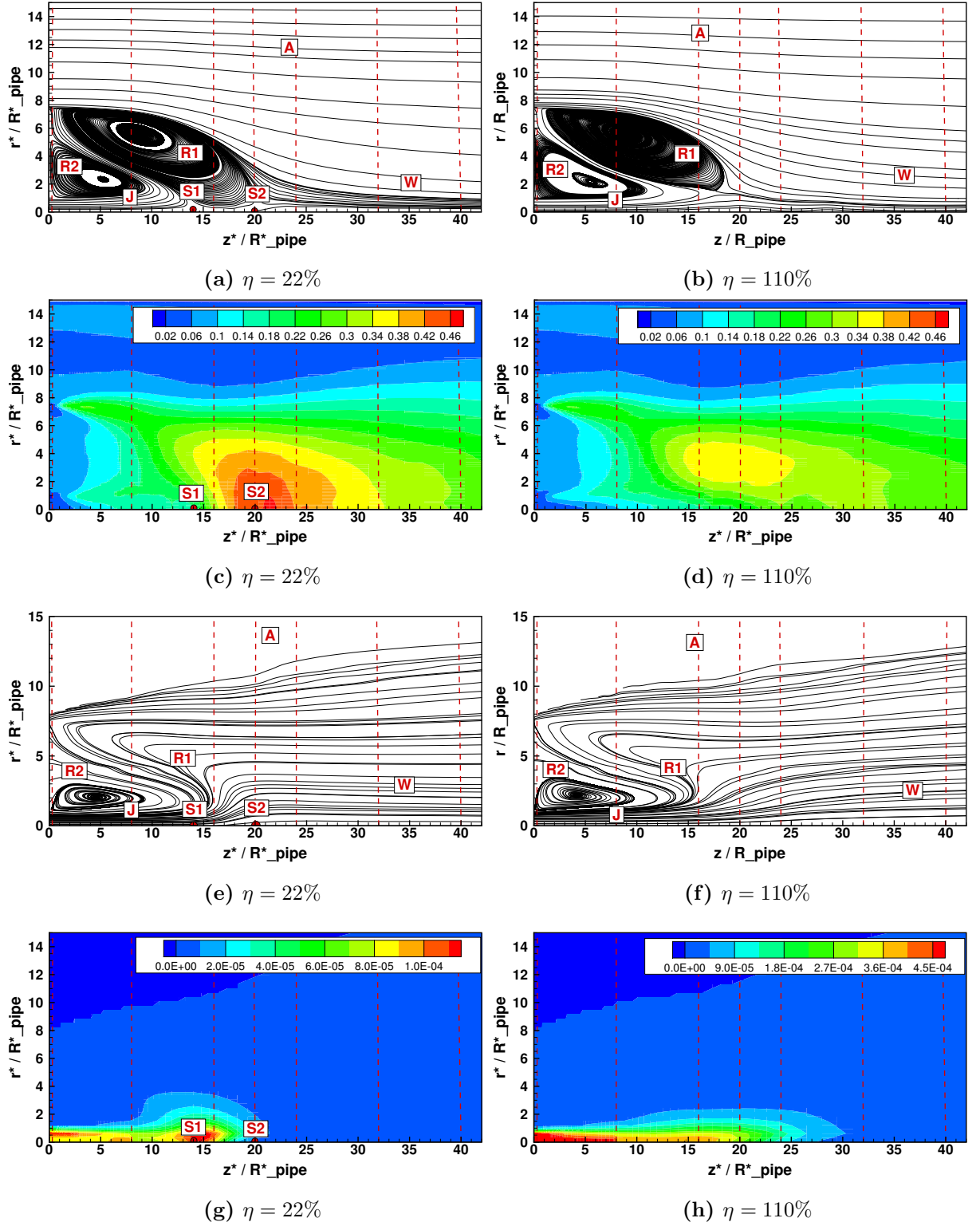


Figure 81: Combustion chamber flow: Averaged data of the four-way coupled cases M4 and H4: (a, b) Streamlines of the continuous flow; (c, d) contour plots of the radial velocity fluctuations $\langle u_{fr}^{*'} \rangle_{rms} / U_{jet}^*$; (e, f) path lines of the particles with a diameter of $d_p^* = 60 \mu\text{m}$; (g, h) contour plots of the mean particle volume fraction Φ .

smaller than the time scales of the flow (Borée et al., 2001). Namazian et al. (1989)

measured the location of S1 at a dimensionless distance from the entrance $z^*/R_{pipe}^* \approx 14$ for a normalized momentum–flux ratio of $M_{jet}^*/M_e^* = 0.36$, whereas Schefer et al. (1987) measured the location of S1 at $z^*/R_{pipe}^* \approx 15$ for $M_{jet}^*/M_e^* = 0.46$. Hence the M4 case is in good agreement with the former possessing about the same momentum–flux ratio¹⁶. The momentum–flux ratios M_{jet}^*/M_e^* provided by Borée et al. (2001) are 0.69, 0.84 and 1.44 for the unladen, the moderate mass loading and the high mass loading case, respectively. For $M_{jet}^*/M_e^* = 0.68$, however, Schefer et al. (1987) reported a flow structure where only one stagnation point on the axis remains, i.e., significantly different from the flow structure with two stagnation points S1 and S2 on the axis reported by Borée et al. (2001) for nearly the same momentum–flux ratio. Combined with the deviations found in the measurements of Borée et al. (2001) between the specified mean velocity at the entrance and the integrated velocity profile of the annular flow at $z^*/R_{pipe}^* = 0.3$ this probably indicates an erroneous specification of the volume flux of the annular flow in Borée et al. (2001).

The second stagnation point S2 found for $\eta = 22\%$ is formed due to the upstream directed flow in the bluff–body recirculation region. The location of S2 depends prevalently on the radius R_a (Schefer et al., 1987; Chen et al., 1998b). In case of the high mass loading (Fig. 81(b)) the recirculation R2 is elongated compared to M2/M4 (Fig. 81(a)). Additionally, it is shifted slightly away from the axis, since in contrast to M2/M4 the central jet penetrates through the recirculation region. Thus, the two stagnation points visible in Fig. 81(a) disappear for $\eta = 110\%$ depicted in Fig. 81(b). Furthermore, the downstream extension of R1 is slightly reduced for H2/H4. In combustion devices a similar flow picture can be found if the momentum injected by the fuel jet is high enough to overcome the recirculation bubble, i.e., a central–jet dominated flame is formed (Chen et al., 1990, 1998b). For this flow configuration the combustion occurs in the recirculation bubble R1 and downstream of it on the axis (Chen et al., 1998b). Finally, behind both recirculation bubbles R1 and R2 a flow field is generated which is typical for the region in the far–field of a bluff body (see, e.g., Zdravkovich (1997)). This region is denoted W in Figs. 81(a) and (b).

Even more drastic than on the mean flow are the effects induced by the disappearance of the two stagnation points S1 and S2 on the radial velocity fluctuations $\langle u_{fr}^* \rangle_{rms}/U_{jet}^*$ (see Figs. 81(c) and (d)) which characterize, especially for the near–axis region, the particle dispersion by turbulence. For M2/M4 (see Fig. 81(c)) the maximum of the radial velocity fluctuations $\langle u_{fr}^* \rangle_{rms}/U_{jet}^*$ is located in a region around the second stagnation point S2 and this region is therefore where most of the particles are dispersed from the axis in radial direction. For H2/H4 (see Fig. 81(d)) the distribution of the radial velocity fluctuations $\langle u_{fr}^* \rangle_{rms}/U_{jet}^*$ is completely different. Here the maximum of the radial velocity fluctuations $\langle u_{fr}^* \rangle_{rms}/U_{jet}^*$ is shifted away from the axis and its magnitude is smaller compared to M2/M4. Both effects lead to a decrease of the particle dispersion by turbulence from the axis towards the outer flow.

The path lines displayed in Figs. 81(e) and (f) provide a first overview of the mean particle motion in the model combustion chamber. At first the M4 case is discussed. As visible from Fig. 81(e) particles with a diameter of $60 \mu\text{m}$ possess enough inertia to pass the recirculation region R1 without being stopped by the upstream directed flow.

¹⁶The momentum–flux ratio in Schefer et al. (1987) and Namazian et al. (1989) is defined as $M_{jet}^*/M_e^* = (U_{jet}^*/U_e^*) \cdot (\rho_{jet}^*/\rho_e^*)^{0.5}$ and hence the square of the indicated values is taken to compare them with the present simulation.

Nevertheless, some particles are entrained by turbulent diffusion into both recirculation regions R1 and R2 following different path lines depending on the recirculation region in which they end up: The particle path lines present in R2 are still closed indicating a mean rotatory motion of the particles. Contrarily, the particles entrained into R1 can follow the fluid motion while they are directed upstream but, due to their inertia, they leave the recirculation bubble almost tangentially when they regain a positive streamwise velocity. It is noticeable that particles, which are able to reach the annular flow A, are still transported radially outwards in spite of the inward curved streamlines (see Figs. 81(a) and (b)). This indicates that the numerical prediction is capable to reproduce the effect of turbophoresis on the particle motion. Turbophoresis is the tendency of particles to migrate in the direction of decreasing turbulence level (Caporaloni et al., 1975). A similar behavior can be observed for the H4 case (see Fig. 81(f)) with the difference that the region where the particles follow a closed path line is marginally larger and the region on the axis where the particles follow nearly a straight path is slightly more extended radially outwards due the absence of the stagnation points S1 and S2.

The effect of the mean upstream directed flow on the axis on the particle dispersion is elucidated by the mean particle volume fraction Φ depicted in Fig. 81(g) for the M4 case. For the moderate mass loading the particles are efficiently dispersed by the recirculation region R1 which extends until the axis. Furthermore, the particles accumulate in the region on the axis between the two stagnation points S1 and S2. The same results were obtained by the LES of Riber et al. (2009). Borée et al. (2001) qualified the local maximum of the particle volume fraction as natural near stagnation points. For the H4 case (Fig. 81(h)), however, the central jet penetrates through the recirculation region R1 and the particles are only gradually dispersed in radial direction by the turbulent fluctuations.

8.7.1.2 Influence of the One-, Two- and Four-way Coupling Assumption on the Particle and Fluid Statistics for $\eta = 22\%$

Continuous Phase

Figure 82 shows the axial evolution of the mean streamwise velocity, the streamwise velocity fluctuations and the radial velocity fluctuations of the continuous phase. Note that the presentation of the simulated cases (MH1, M2, M4) and of the single-phase and two-phase measurements of Borée et al. (2001) is not changed in this section and therefore the legend is displayed only in Fig. 82. Figure 82(a) depicts the axial velocity of the fluid along the axis. As visible, the flow field of the continuous phase is influenced by the particulate phase already at this moderate mass loading. The jet developing at the exit of the pipe is stopped rapidly in the recirculating flow forming a first stagnation point S1 on the axis already depicted by the streamlines in Fig. 81(a). In the unladen case MH1 the first stagnation point S1 is found at about $z^*/R_{pipe}^* = 12.56$, whereas for the two-way and four-way coupled cases M2/M4 this point is shifted downstream to about $z^*/R_{pipe}^* = 13.99$ and 14.09 , respectively. The same trend even more pronounced can be observed between the single-phase and two-phase experimental data by Borée et al. (2001). Contrarily, the deviation between the two-way and four-way coupled cases is minor, indicating that the role of particle-particle collisions is of less importance for this mass loading. However, the influence of the particles on the fluid is of major interest. A second stagnation point S2 of the mean fluid flow is located at the end of the recirculation bubble R1 at $z^*/R_{pipe}^* = 20.3$. Here the differences between the three predicted cases are

minor. Figure 82(b) depicts the axial evolution of the streamwise velocity fluctuations. No significant differences can be found between the one-, two- and four-way coupled predictions. The maximum is observed in accordance with the experiments in the region of the maximum axial velocity gradient and is slightly underpredicted and shifted upstream. Figure 82(c) illustrates the radial velocity fluctuations along the axis. These Reynolds stresses are overpredicted in the region past the recirculation region R2, but the maximum is found similar to the experiments at the end of the recirculation region R1 near S2 (see also Fig. 81(c)). It is worth noting that, if the influence of the particles on the fluid is taken into account, the maximum is slightly diminishing with respect to the one-way coupled case and furthermore marginally shifted downstream. The maximum deviation between the predictions and the measurements is observed quite far away from the entrance, i.e., near the second stagnation point S2.

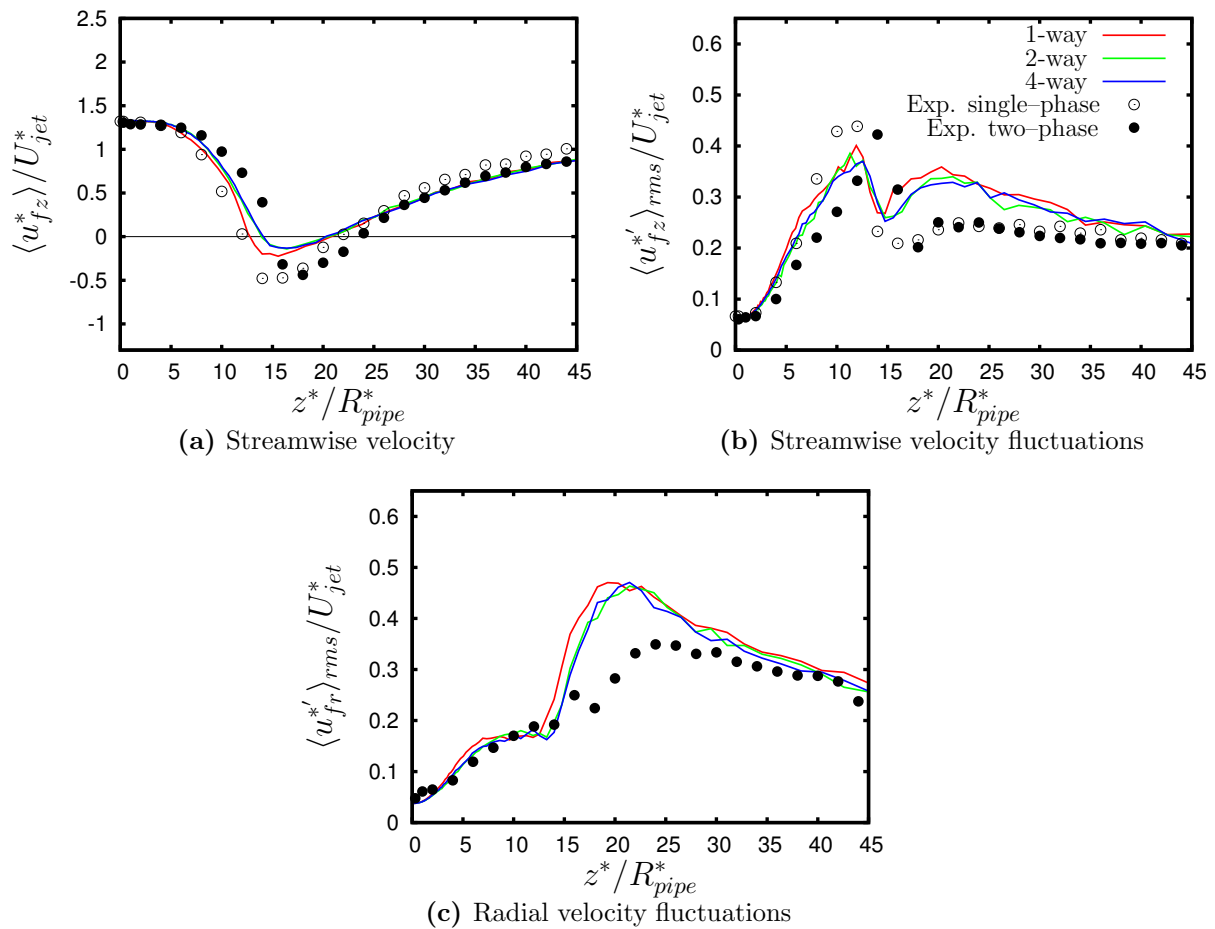


Figure 82: Axial evolution of the streamwise velocity and the streamwise and radial velocity fluctuations of the continuous phase at $\eta = 22\%$; experimental data by Borée et al. (2001).

Figure 83 shows the mean axial fluid velocity at all measurement planes investigated by Borée et al. (2001) for this mass loading, i.e., $z^*/R_{pipe}^* = 0.3, 8, 16, 20, 24, 32$ and 40 . To provide a better overview of how the flow develops along the chamber, the profiles are plotted at their corresponding dimensionless locations of the measurement planes z^*/R_{pipe}^* and additionally scaled by a factor of 3. In all figures using this presentation the location of the measurement planes is characterized by vertical dashed lines. The horizontal dashed

lines denote the location where the pipe and the annular flows are discharged into the combustion chamber. The first measurement plane analyzed by Borée et al. (2001) is located at $z^*/R_{pipe}^* = 0.3$, i.e., shortly behind the inlet. A good agreement is found between the experiment and the simulations for the central pipe flow. Here, according to the experimental set-up the development section was long enough to ensure a fully developed turbulent pipe flow (Borée et al., 2001) as assumed in the present simulations by the additional predictions for the inflow generation. Differences between the experiments and the simulations in this measurement plane are restricted to the annular fluid flow where the measured profile is slightly asymmetric. The asymmetric experimental profile can probably be traced back to the rather short development section of the annular flow (Borée et al., 2001) which yields a non-fully developed turbulent flow and consequently is difficult to reproduce by a separate simulation for the inflow generation applying periodic boundary conditions. Regarding all other measurement planes in general good agreement is found between the experiments and the simulations except for the outer radii where the predicted mean velocity is too high. As will be shown in § 8.7.2.2 this discrepancy between the simulation and the experiment can be removed by improving the accordance of the inflow data used in the simulation with the one measured by Borée et al. (2001). Note, however, that there are also certain discrepancies between the measurements of the mean velocity in the unladen case and in the case of $\eta = 22\%$ at the outer radii. These deviations are difficult to explain since the influence of the particles on the carrier phase at $\eta = 22\%$ is expected to be localized to a region near the axis and not too far downstream of the chamber entrance, i.e., where the particle concentration is high enough to justify a feedback on the continuous phase (see Fig. 81(g)). However, good agreement with the unladen measurements in the outer radii can be detected. Minor differences between the one-, two- and four-way coupled simulations are found only in the near-axis region of the measurement plane $z^*/R_{pipe}^* = 16$ where the mean fluid velocity is slightly higher for the two- and four-way coupled fluid flow due to the momentum transferred from the disperse to the continuous phase.

Figure 84 shows the mean radial fluid velocity at the measurement planes $z^*/R_{pipe}^* = 0.3, 16, 20, 24, 32$ and 40 . The same presentation as for the mean axial velocity is chosen but with a larger scaling factor of 10 since the magnitude of this component is much lower. It is obvious that there are no significant differences observable between the one-, two- and four-way coupled simulations. Very good agreement between the experiment and the simulations can be found in the measurement plane cutting the two recirculation regions R1 and R2 located at $z^*/R_{pipe}^* = 8$. The mean radial velocity is directed away from the axis until slightly above the center of R1 (see Fig. 81(a)) and becomes negative near the mixing layer between the annular flow and R1. At the measurement plane located at $z^*/R_{pipe}^* = 16$, it is visible that the mean radial fluid velocity is very well captured near the axis, where both, experiment and simulations, show a flat slope of the radial profile indicating streamlines almost parallel to the axis (see also Fig. 81(a)). The magnitude of the radial velocity in the center of the annular flow is underestimated indicating that the simulated recirculation bubble is flatter than the one present in the experiments. The same observation (smaller magnitude of the simulated radial velocity) can be made at all following measurement planes indicating that the influence of the bluff body (inward directed streamlines) is visible far beyond the recirculation bubble. Note, however, that deviations can also be observed between the unladen and laden measurements for this velocity component at $z^*/R_{pipe}^* = 24$ and 32 similar to the mean streamwise velocity.

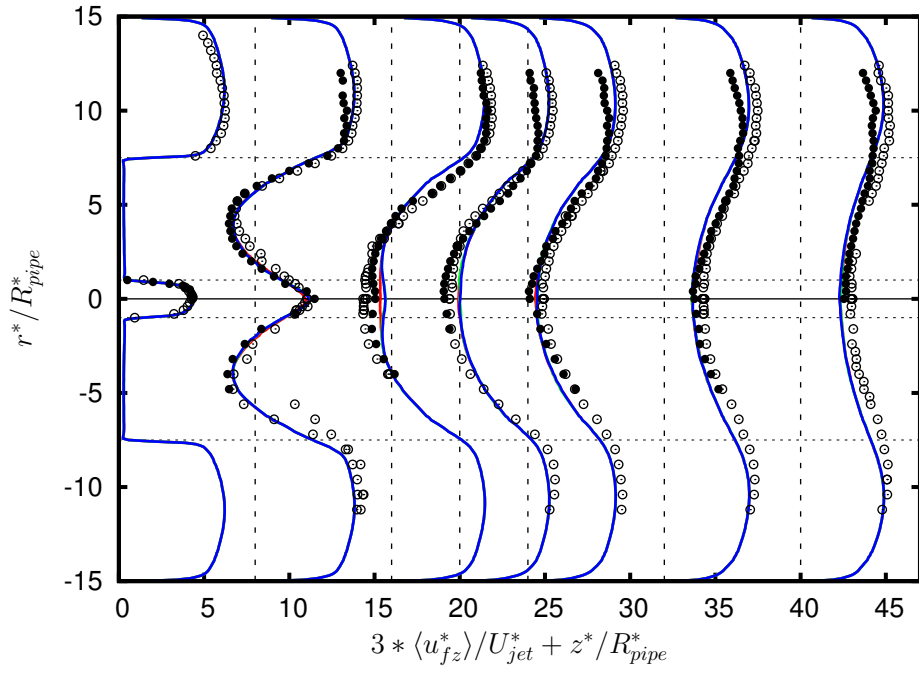


Figure 83: $\eta = 22\%$: Streamwise fluid velocity at the measurement planes $z^*/R_{pipe}^* = 0.3, 8, 16, 20, 24, 32$ and 40 . Red line: 1-way, green line: 2-way, blue line: 4-way, open symbols: Exp. single-phase, filled symbols: Exp. two-phase (Borée et al., 2001).

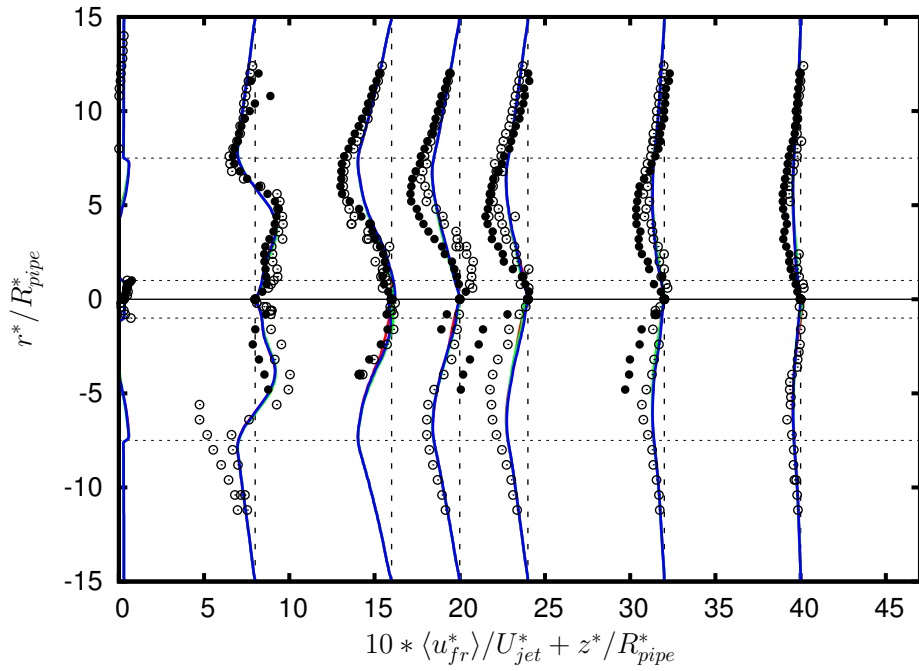


Figure 84: $\eta = 22\%$: Radial fluid velocity at the measurement planes $z^*/R_{pipe}^* = 0.3, 8, 16, 20, 24, 32$ and 40 . Red line: 1-way, green line: 2-way, blue line: 4-way, open symbols: Exp. single-phase, filled symbols: Exp. two-phase (Borée et al., 2001).

Figure 85 shows the streamwise velocity fluctuations of the continuous phase at all measurement planes z^*/R_{pipe}^* using a scaling factor of 18. As obvious from Fig. 85 good agreement can be seen between simulations and experiment at the measurement plane

$z^*/R_{pipe}^* = 0.3$. From the data at the measurement plane $z^*/R_{pipe}^* = 8$ it is evident that two local maxima are present at the shear layers between the central jet J and the recirculation region R2 as well as between R1 and the annular flow A (see Fig. 81(a)). Good agreement with the experiments is found here. At the remaining measurement planes the following observations can be made: (i) Since the jet flow is not perceptible far downstream of the inlet, only one local maximum is present as it is typical for the flow in the far-field of a bluff body. (ii) The fluctuations are decreasing in streamwise direction. (iii) Reasonable agreement with the experiments can be observed. (vi) Again major unexpected deviations are observed in the outer region between the single-phase and two-phase flow in the experiment of Borée et al. (2001).

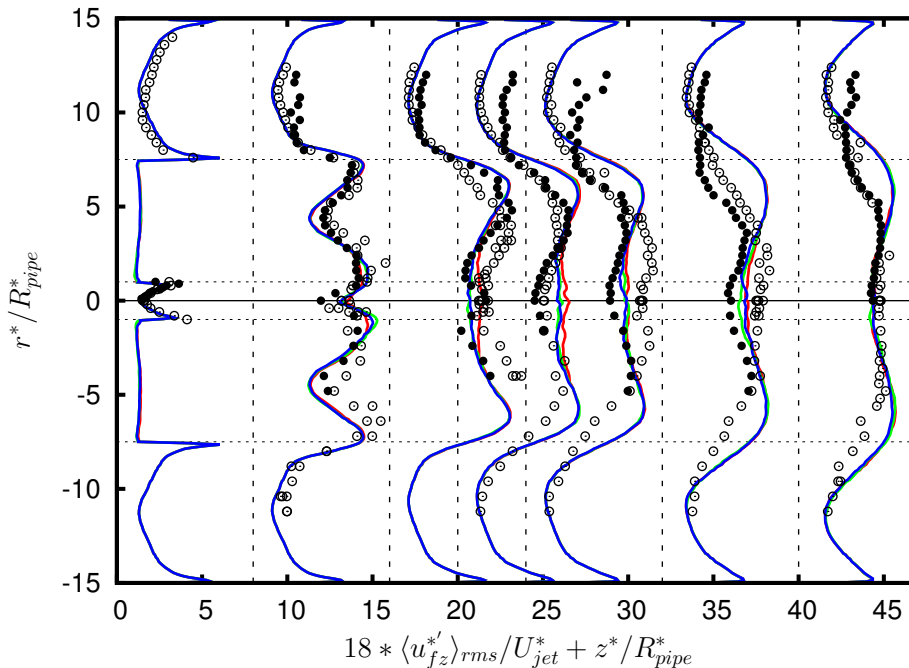


Figure 85: $\eta = 22\%$: Streamwise fluid velocity fluctuations at the measurement planes $z^*/R_{pipe}^* = 0.3, 8, 16, 20, 24, 32$ and 40 . Red line: 1-way, green line: 2-way, blue line: 4-way, open symbols: Exp. single-phase, filled symbols: Exp. two-phase (Borée et al., 2001).

Figure 86 shows the radial velocity fluctuations of the continuous phase at the measurement planes with the same scaling factor as in Fig. 85. Observing this quantity at $z^*/R_{pipe}^* = 0.3$, i.e., close to the inlet, good agreement is found with the experiments. As for the velocity fluctuations in streamwise direction also the radial velocity fluctuations at $z^*/R_{pipe}^* = 8$ show two local maxima at the border region between the central jet J and R2 as well as R1 and the annular flow A. Interestingly, while at the plane $z^*/R_{pipe}^* = 16$ the maximum of the radial velocity fluctuations is located at the edge of the shear layer between R1 and the annular flow, for all planes located further downstream the maximum is found on the axis which is typical for a flow in the far-field of a bluff body (Zdravkovich, 1997) where the shear layers merge. Except in the near-axis region at the plane $z^*/R_{pipe}^* = 20$, good agreement is found with the experiments. The differences between experiment and simulations for this plane coincide with the deviations found for this component of the Reynolds stress in the region between the two stagnation points S1 and S2 (see Fig. 82(c)).

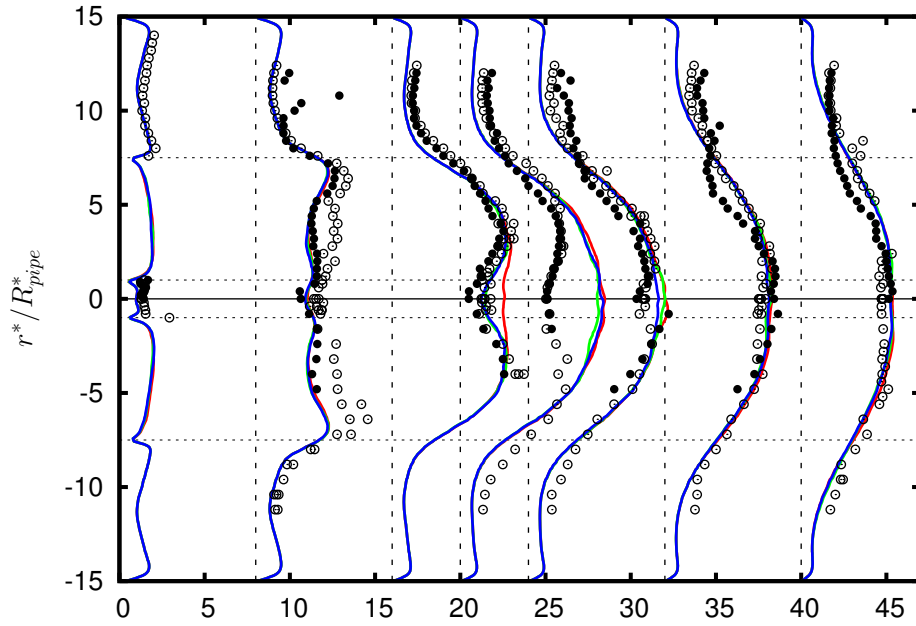


Figure 86: $\eta = 22\%$: Radial fluid velocity fluctuations at the measurement planes $z^*/R_{pipe}^* = 0.3, 8, 16, 20, 24, 32$ and 40 . Red line: 1-way, green line: 2-way, blue line: 4-way, open symbols: Exp. single-phase, filled symbols: Exp. two-phase (Borée et al., 2001).

Particulate Phase ($d_p^* = 60 \mu\text{m}$)

Figure 87 shows the axial evolution of the mean particle velocity and the streamwise and radial particle fluctuations. As for the continuous phase the legend is shown only in this figure, since the presentation of the different cases does not change throughout the section. Particles with a diameter of $d_p^* = 60 \mu\text{m}$, i.e., comparable to the mass-averaged diameter $\overline{d_{p,M}^*} = 63 \mu\text{m}$, are chosen to illustrate the effect of inertia on the particle motion. Generally good agreement is found between the simulated mean particle velocity on the axis (see Fig. 87(a)) and the experiments of Borée et al. (2001). Minor difference can be already observed at the entrance, where the measured mean particle velocity is smaller than the mean fluid velocity even though the gravitational acceleration pointed in flow direction. This effect cannot be reproduced by the simulation, because the effect of the rough pipe walls on the particle motion is not considered for the evaluation of the influence of the coupling assumption. As will be shown in § 8.7.2.2, the accordance between the simulations and the experiment in the near-axis region close to the entrance can be improved by accounting for the effect of the wall roughness seen by the particles in the pipe flow feeding the chamber. Furthermore, similar to the mean fluid velocity on the axis (see Fig. 82(a)) the minimum of the particle velocity on the axis is shifted upstream compared to the experiments. The effect of inertia is clearly visible based on the particle behavior on the axis: While for the fluid flow two stagnation points are present, the particles with this specific diameter are not decelerated as fast as the continuous phase and thus they are able to pass the recirculation region R1 without inverting their mean direction of motion. Similar to the mean particle axial velocity (Fig. 87(a)) the differences between the simulated and measured particle velocity fluctuations at the chamber entrance (see Figs. 87(b) and (c)) can be explained by the disregard of the wall roughness effect on the particles motion in the pipe flow. Wall roughness typically leads to a decrease of the

mean particle velocity and an increase of the particle axial and wall-normal fluctuations of the particles (Kussin and Sommerfeld, 2002; Vreman, 2007; Breuer et al., 2012) which is consistent with the observations made. Similar to the fluid velocity fluctuations on the axis (see Fig. 82(b)) the peak of the particle streamwise velocity fluctuations on the axis is slightly shifted upstream with respect to the experiments but the magnitude is captured very well, especially for the two- and four-way coupled simulations. In contrast to the radial fluid velocity fluctuations on the axis (Fig. 82(c)), there are only minor discrepancies between the simulations and the experiment for the radial particle velocity fluctuations (Fig. 87(c)) in the region $15 < z^*/R_{pipe}^* < 25$, i.e., in the domain, where the recirculation is secluded by the outer annular flow.

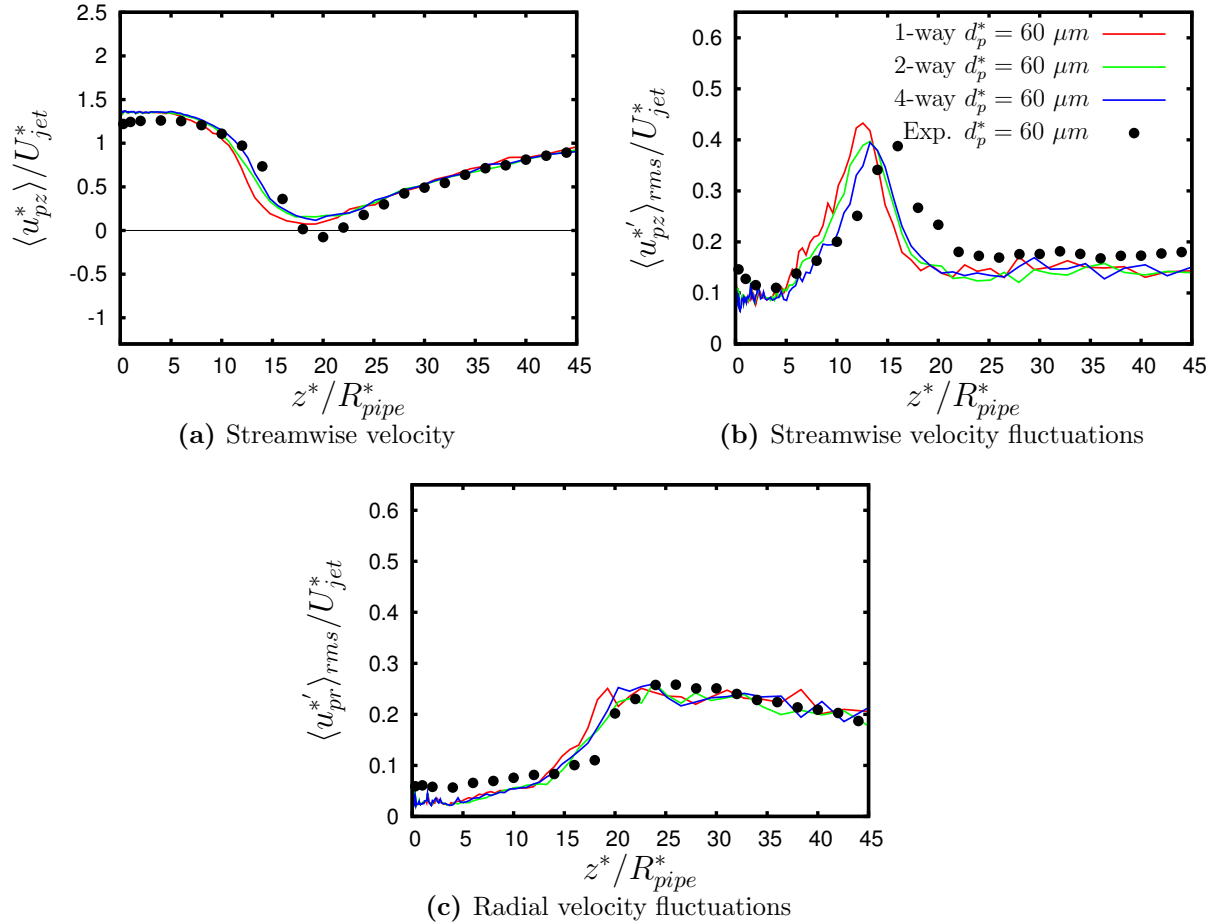


Figure 87: Axial evolution of the streamwise velocity and the streamwise and radial velocity fluctuations of the particulate phase with a diameter of $d_p^* = 60 \mu m$ at $\eta = 22\%$; experimental data by Borée et al. (2001).

Figure 88 shows the mean streamwise particle velocity at all measurement planes z^*/R_{pipe}^* . The same presentation as used for the mean fluid velocity (Fig. 83) is applied to visualize the evolution of the mean particle velocity in the chamber. Good agreement is found between the simulations and the experiment except for the axial region of the measurement plane around $z^*/R_{pipe}^* = 20$. The reason is the upstream shift of the minimum particle mean velocity on the axis in the prediction depicted in Fig. 87(a): In the experiment this measurement plane is located at the minimum of the particle mean velocity on the axis, whereas in the simulations the particles are already accelerated by the

surrounding fluid. Note that the effect of inertia on the particle motion is manifested by a smaller or even not existing region of negative particle velocities with respect to the central region of negative fluid velocities (Compare the mean particle velocities with the mean fluid velocity at the measurement planes $z^*/R_{pipe}^* = 8$ and 16 and the streamlines depicted in Fig. 81(a) with the particle paths shown in Fig 81(e)).

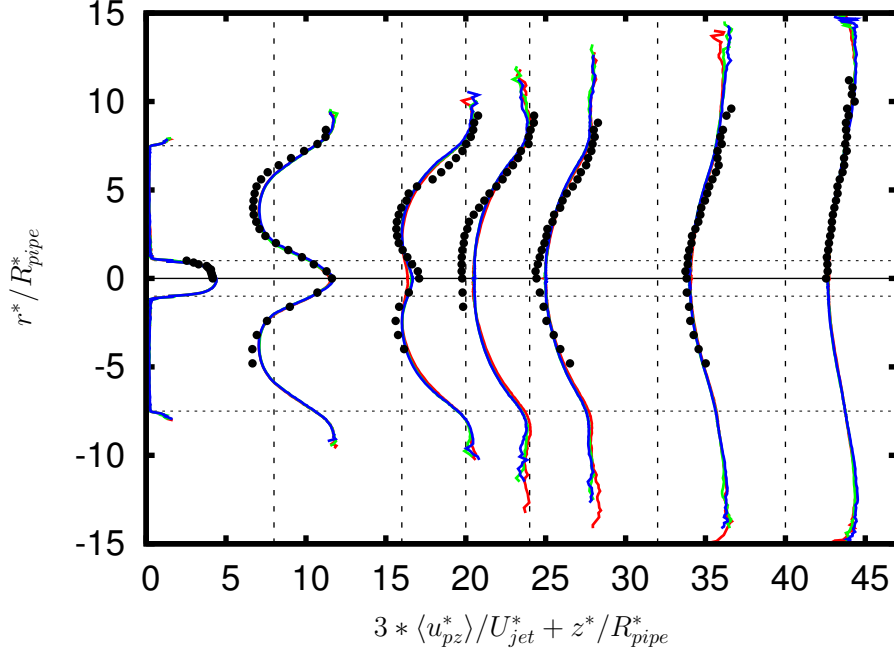


Figure 88: $\eta = 22\%$: Streamwise velocity of particles with a diameter of $d_p^* = 60 \mu\text{m}$ at the measurement planes $z^*/R_{pipe}^* = 0.3, 8, 16, 20, 24, 32$ and 40 . Red line: 1-way, green line: 2-way, blue line: 4-way, filled symbols: experiment by Borée et al. (2001).

Figure 89 shows the mean radial velocity of the particulate phase using the same scaling factor as for the continuous flow. At $z^*/R_{pipe}^* = 8$ it is visible that in this measurement plane the particles are transported outwards following the fluid motion throughout the jet and R2, but when they reach the upper part of R1 (see Figs. 81(a) and (e)) they are not anymore able to follow the continuous phase and tangentially leave the recirculation bubble with a mean trajectory still pointing away from the axis. Contrarily, in the measurement planes $z^*/R_{pipe}^* = 16, 20$ and 24 there still exist regions in which the particles are directed towards the inner part of the chamber. Noticeable is that although in the annular flow region the mean fluid flow is directed towards the axis (see Figs. 81(a) and 83), the particles are still transported due to turbophoresis in the direction of the chamber walls. This effect can be reproduced in accordance with the experiments in all measurement planes of Fig. 89. Note, since solely the drag force on the particles is considered, the only effect leading to a transport of the particles towards the wall is the negative gradient of the radial fluid velocity fluctuations (see Fig. 86).

Figures 90 and 91 show the axial and radial particle velocity fluctuations. The difference in magnitude between measured and simulated particle streamwise velocity fluctuations at the measurement planes $z^*/R_{pipe}^* = 16, 20$ and 24 can be attributed to the shifted location of the peak value of the particle streamwise velocity fluctuations, whereas the agreement is good in the planes located at $z^*/R_{pipe}^* = 8, 32$ and 40 . Comparing the radial velocity fluctuations of the particulate phase shown in Fig. 91 with the experiments of Borée et al.

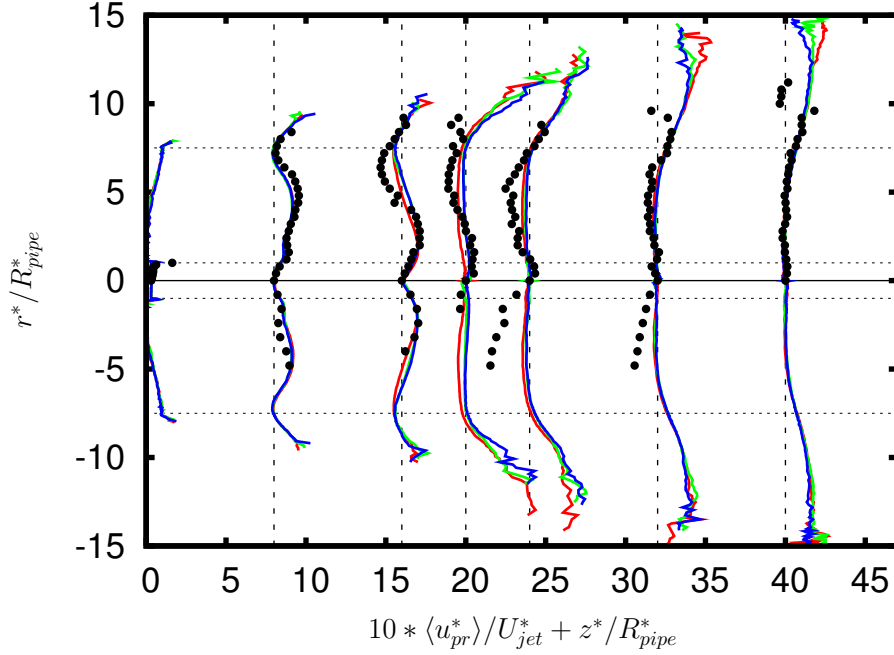


Figure 89: $\eta = 22\%$: Radial velocity of particles with a diameter of $d_p^* = 60 \mu\text{m}$ at the measurement planes $z^*/R_{pipe}^* = 0.3, 8, 16, 20, 24, 32$ and 40 . Red line: 1-way, green line: 2-way, blue line: 4-way, filled symbols: experiment by Borée et al. (2001).

(2001), it is evident that good agreement is found in all presented measurement planes. Minor differences can be observed only at the inlet, which as mentioned above, can be attributed to the disregard of the wall roughness effect in the pipe flow used to generate the inflow data.

8.7.1.3 Influence of the One-, Two- and Four-way Coupling Assumption on the Particle and Fluid Statistics for $\eta = 110\%$

Continuous Phase

Figure 92 shows the axial evolution of the streamwise velocity and the streamwise and radial velocity fluctuations of the continuous phase for the $\eta = 110\%$ case. From the mean fluid velocity on the axis depicted in Fig. 92(a) it is clearly visible that the one-way coupling assumption does not hold anymore for this mass loading. The particles injected into the chamber carry enough momentum to cause the disappearance of the two stagnation points S1 and S2. Additionally, the central jet extends further downstream compared to the one-way coupled simulation and the minimum of the streamwise velocity is located at the end of the recirculation region R1 at about $z^*/R_{pipe}^* = 21.4$ (see also Fig. 81(b)). On the other hand, the deviations between the two- and four-way coupled simulations are hardly noticeable indicating the minor importance of the particle-particle collisions. This is consistent with the mean particle volume fraction Φ at the entrance visualized in Fig. 81(h). Here, a maximum value of $\Phi \approx 4.5 \cdot 10^{-4}$ is observed, which is slightly below the threshold ($\Phi = 10^{-3}$) specified by Sommerfeld et al. (2008) above which the particle-particle interactions become important. Along the axis Φ further decreases rapidly to about half of its maximum at the end of the recirculation bubble R1. Since in

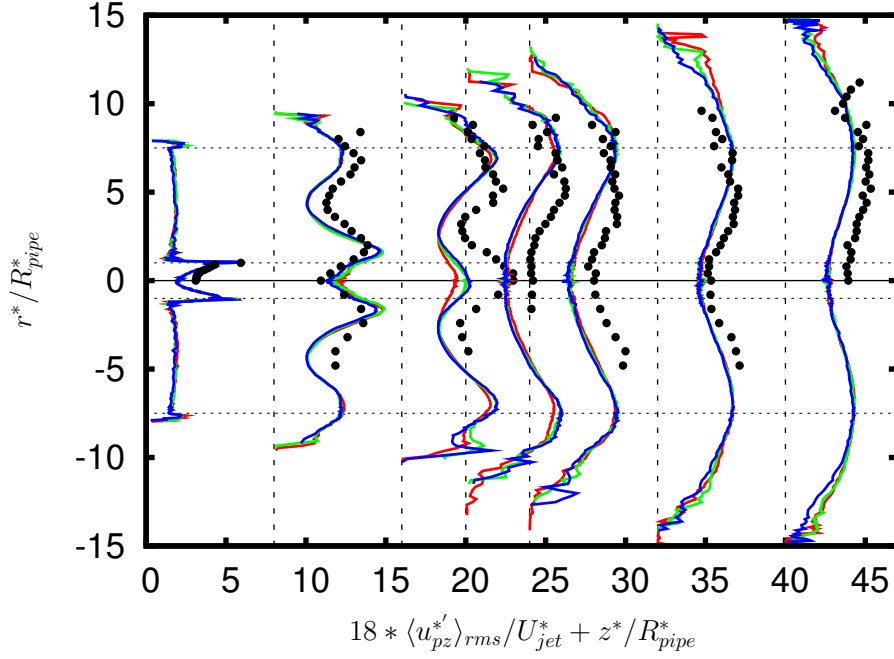


Figure 90: $\eta = 22\%$: Streamwise velocity fluctuations of particles with a diameter of $d_p^* = 60 \mu\text{m}$ at the measurement planes $z^*/R_{pipe}^* = 0.3, 8, 16, 20, 24, 32$ and 40 . Red line: 1-way, green line: 2-way, blue line: 4-way, filled symbols: experiment by Borée et al. (2001).

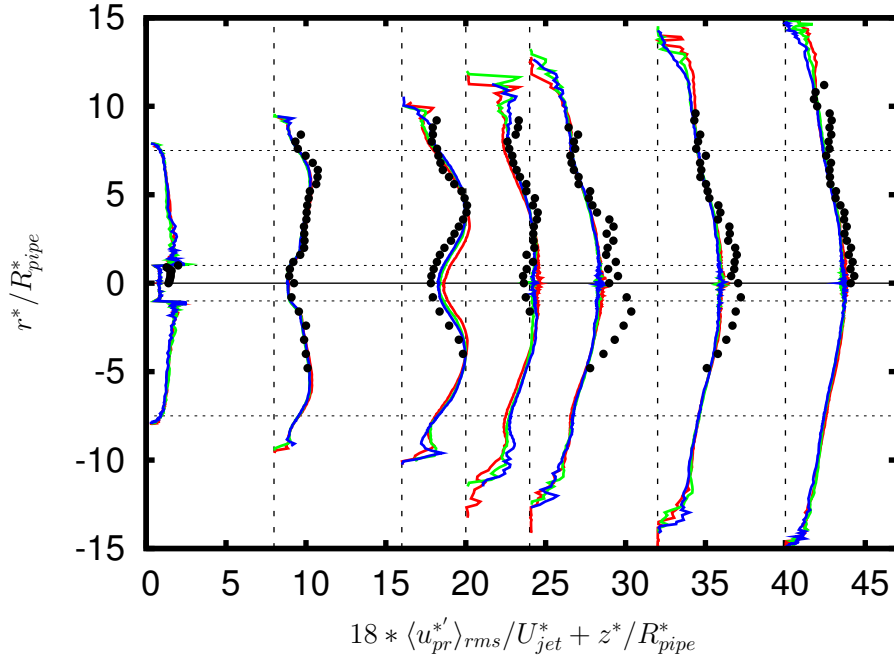


Figure 91: $\eta = 22\%$: Radial velocity fluctuations of particles with a diameter of $d_p^* = 60 \mu\text{m}$ at the measurement planes $z^*/R_{pipe}^* = 0.3, 8, 16, 20, 24, 32$ and 40 . Red line: 1-way, green line: 2-way, blue line: 4-way, filled symbols: experiment by Borée et al. (2001).

contrast to $\eta = 22\%$ no stagnation points exist in this case, a local maximum of Φ does

not appear and thus Φ remains low.

Figure 92(b) shows the fluid velocity fluctuations on the axis. For both, the experiment and the simulations, the maxima of the fluid velocity fluctuations are shifted downstream with respect to the maxima of the fluid velocity fluctuations obtained for the unladen case. Furthermore, the maxima of the fluid velocity fluctuations on the axis coincide with the maximum slope of the mean streamwise velocity on the axis. The maximum also coincides with the end of the axial extension of the second recirculation bubble R2 (see Fig. 81(b)) and is underpredicted in comparison with the experiments. Note, however, that the grid is axially stretched away from the entrance and therefore it becomes coarser in the region of the maximum velocity gradient (see Fig. 92(a)) compared to the inlet region.

For the radial velocity fluctuations (Fig. 92(c)) the two-phase data of Borée et al. (2001) with a mass loading of $\eta = 22\%$ are shown for comparison because there are no single-phase data available. Observing the evolution of this component of the Reynolds stress tensor on the axis, it is evident that the disappearance of the two stagnation points S1 and S2 on the axis leads to a strong reduction of this quantity in the simulations. In the experiments, however, no significant difference between the moderate and high mass loading case can be reported. This is surprising since the penetration of the jet through the recirculation region R1 should also affect this quantity as visible in the experiment of Schefer et al. (1994). They reported a strong decrease of the radial velocity fluctuations on the axis if the stagnation points S1 and S2 are shifted away from the axis. Nevertheless, a good agreement is found between the simulations H2/H4 and the experimental data of Borée et al. (2001) for $\eta = 110\%$.

Figure 93 shows the mean streamwise fluid velocity at all measurement planes. Note that for this case there exist only experimental two-phase data for the planes $z^*/R_{pipe}^* = 0.3, 8, 16$ and 20 . It is clearly visible that in the H2 and H4 cases a jet-like flow structure on the axis is retained further downstream with respect to the MH1 case and is still visible at the plane located at $z^*/R_{pipe}^* = 20$. Differences to the MH1 case are restricted in analogy to the experiments to the near-axis region. Good agreement with the experiments is found in all measurement planes. In this case the deviations between the single-phase and the two-phase measurements of Borée et al. (2001) found in the outer radii are not as pronounced as for the moderate mass loading (see Fig. 83). Furthermore, the centerline velocity of the measured velocity profile at $z^*/R_{pipe}^* = 0.3$ (see also the entrance region of Fig. 92(a)) for the high mass loading is reduced compared to the measured centerline velocity of the unladen case. The same effect could be reproduced by Vreman (2007) by his four-way coupled DNS considering the wall roughness effect on the particle motion.

Figure 94 shows the mean radial fluid velocity at all measurement planes. The further downstream extension of the jet-like flow structure near the axis compared with the MH1 case is also noticeable in this statistical moment. The jet-like flow structure is characterized by a positive radial velocity and is visible until the measurement plane located at $z^*/R_{pipe}^* = 20$. Good agreement is found with the experiments of Borée et al. (2001).

Figures 95 and 96 show the fluid velocity fluctuations in streamwise and radial directions, respectively. As for all other fluid statistics presented, also for the second-order statistics the influence of the additionally injected momentum by the particles is restricted to a region near the axis which spreads in downstream direction. It is clearly visible that the local minimum of the fluid streamwise velocity fluctuations (Fig. 95) on the axis of

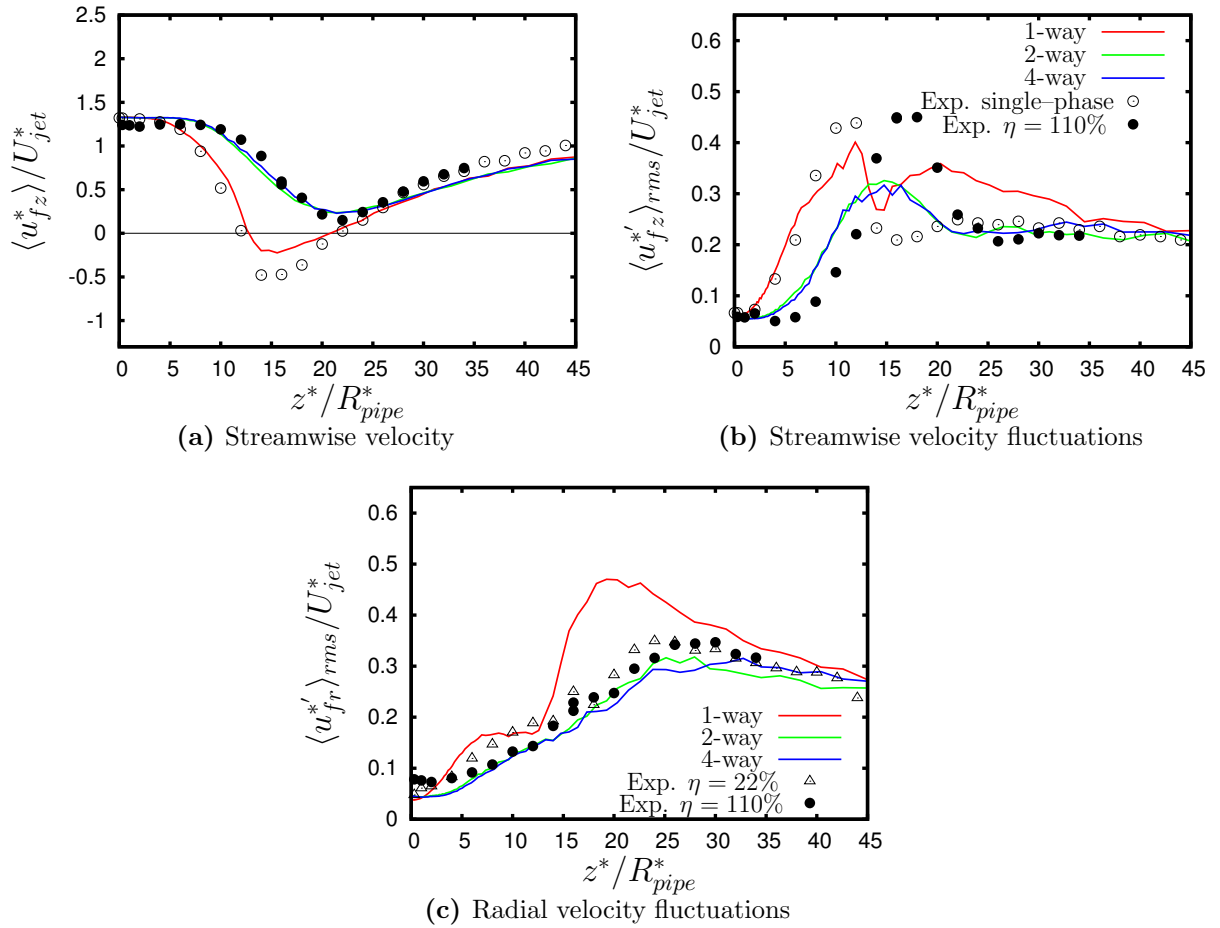


Figure 92: Axial evolution of the streamwise velocity and the streamwise and radial velocity fluctuations of the continuous phase at $\eta = 110\%$; experimental data by Borée et al. (2001)

the jet surrounded by the local maximum present at the shear layer between the jet J and the recirculation region R1 extends beyond the measurement plane $z^*/R_{pipe}^* = 16$. The deviations near the axis found for the measurement planes $z^*/R_{pipe}^* = 16$ and 20 are consistent with the deviation observed in Fig. 92(b) and indicate that the radial extension of the recirculation bubble R1 is slightly underpredicted in the simulation with respect to the experiment. Note that in the experiment of Borée et al. (2001) the measurement plane at $z^*/R_{pipe}^* = 20$ coincides with the location where the local maxima of the streamwise velocity fluctuations (shear layer) merge on the axis, whereas in the simulation at this axial position already a wake-like distribution of this quantity is found. For the radial fluid velocity fluctuations (Fig. 96) very good agreement is found with the experiments at $z^*/R_{pipe}^* = 8$. For $z^*/R_{pipe}^* = 16$ and 20 deviations are visible in the region between the axis and the outer shear layer developing between R1 and the annular flow. Note that for this component of the Reynolds stress the local minimum present on the axis at $z^*/R_{pipe}^* = 8$ is still visible at $z^*/R_{pipe}^* = 24$ and the local maximum of the radial velocity fluctuations typical for the far-field of a bluff body develops only further downstream. For all other statistics presented, interestingly at this location already typical wake-like distributions are found near the axis.

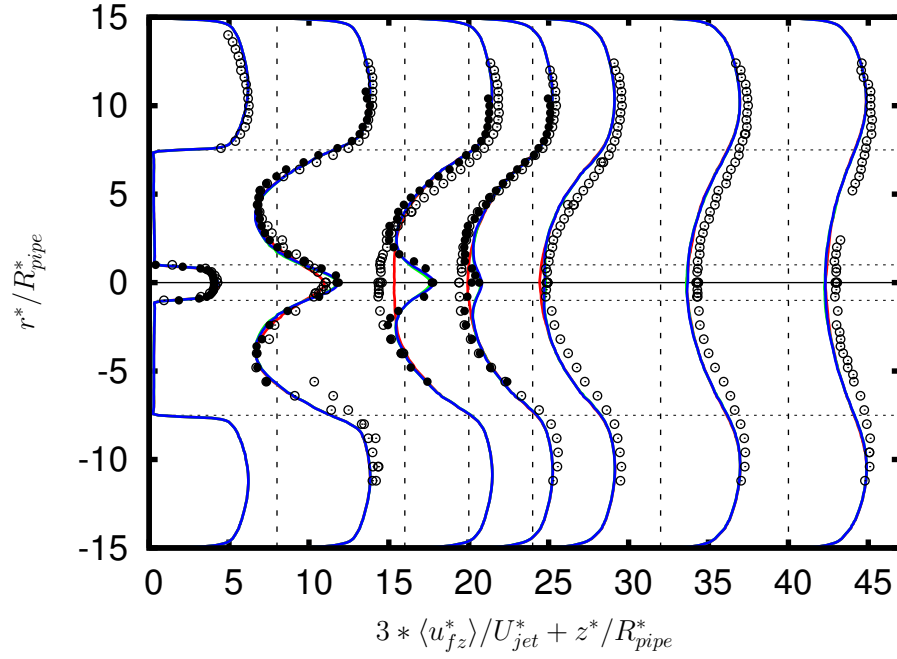


Figure 93: $\eta = 110\%$: Streamwise fluid velocity at the measurement planes $z^*/R_{pipe}^* = 0.3, 8, 16, 20, 24, 32$ and 40 . Red line: 1-way, green line: 2-way, blue line: 4-way, open symbols: Exp. single-phase, filled symbols: Exp. two-phase (Borée et al., 2001).

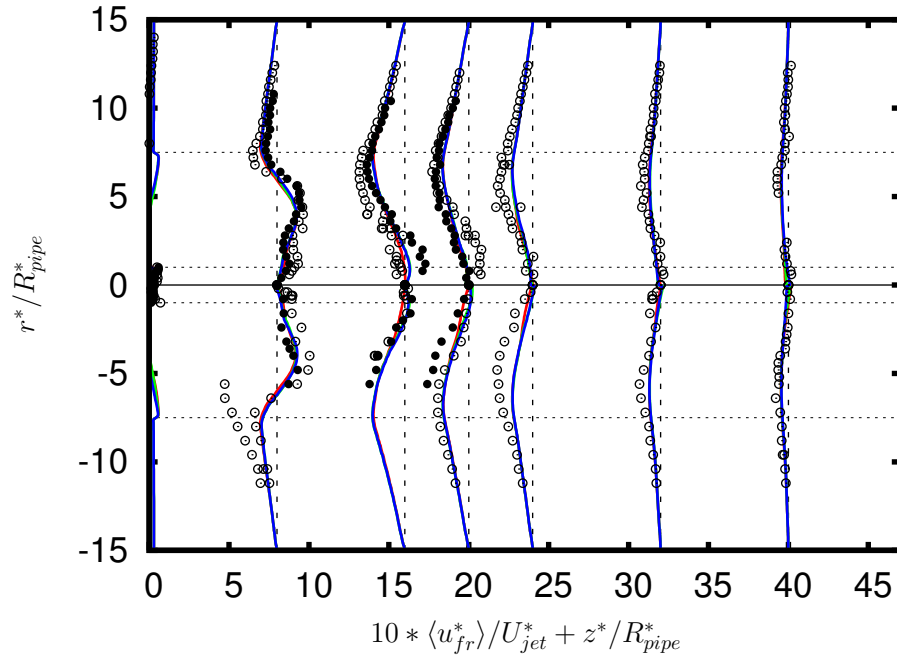


Figure 94: $\eta = 110\%$: Radial fluid velocity at the measurement planes $z^*/R_{pipe}^* = 0.3, 8, 16, 20, 24, 32$ and 40 . Red line: 1-way, green line: 2-way, blue line: 4-way, open symbols: Exp. single-phase, filled symbols: Exp. two-phase (Borée et al., 2001).

Particulate Phase ($d_p^* = 60 \mu\text{m}$)

Figure 97 shows the axial evolution of the mean streamwise velocity and the streamwise and radial fluctuations for the $60 \mu\text{m}$ particles. It is evident that also for a reliable

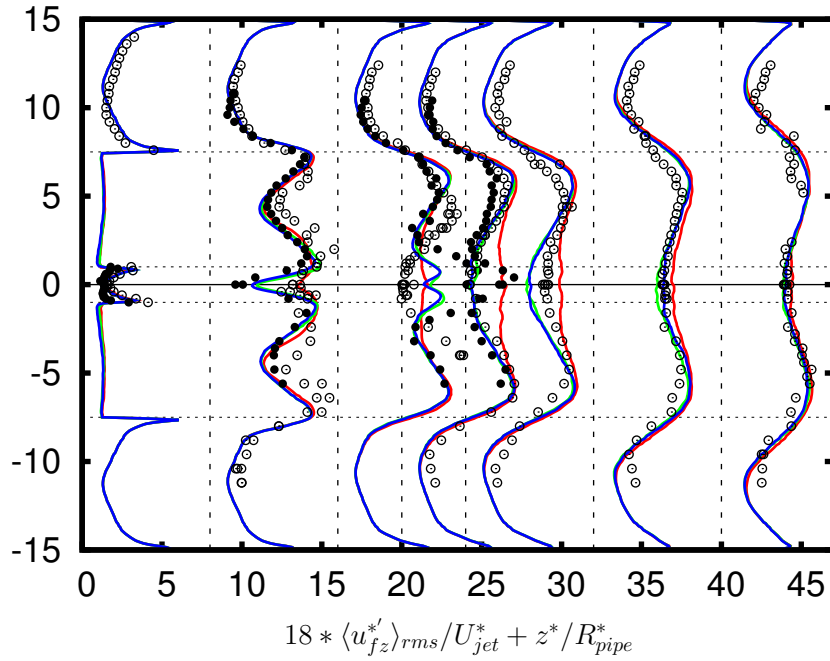


Figure 95: $\eta = 110\%$: Axial fluid velocity fluctuations at the measurement planes $z^*/R_{pipe}^* = 0.3, 8, 16, 20, 24, 32$ and 40 . Red line: 1-way, green line: 2-way, blue line: 4-way, open symbols: Exp. single-phase, filled symbols: Exp. two-phase (Borée et al., 2001).

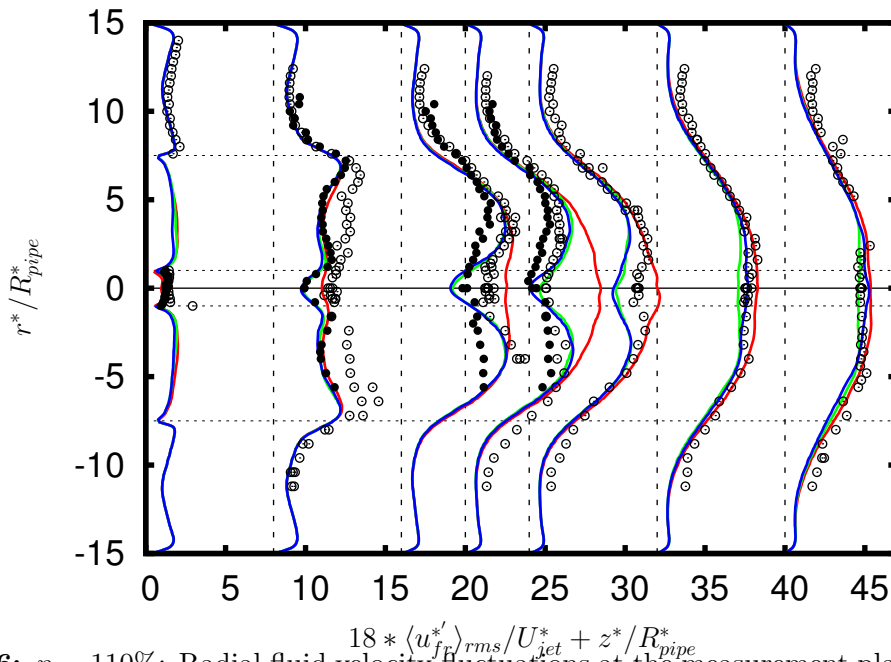


Figure 96: $\eta = 110\%$: Radial fluid velocity fluctuations at the measurement planes $z^*/R_{pipe}^* = 0.3, 8, 16, 20, 24, 32$ and 40 . Red line: 1-way, green line: 2-way, blue line: 4-way, open symbols: Exp. single-phase, filled symbols: Exp. two-phase (Borée et al., 2001).

prediction of the particulate phase the correct choice of the particle–fluid interaction is crucial: Taking the two-way or four-way coupling assumption into account the minimum

axial velocity of the 60 μm particles (Fig. 97(a)) is considerably shifted downstream due to the absence of the two stagnation points S1 and S2. Furthermore, the magnitude is higher than for the MH1 case. Figure 97(b) shows the axial evolution of the streamwise particle velocity fluctuations. It is obvious that the maximum is shifted downstream for the H2 and H4 cases and the position corresponds in analogy to the experiment with the maximum slope of the mean streamwise particle velocity. The maximum is located at the end of R1. The reduction of the particle velocity fluctuations in radial direction (Fig. 97(c)) for the H2 and H4 cases compared to MH1 additionally underlines the minor particle dispersion in the case where the stagnation points S1 and S2 are shifted away from the axis. Furthermore, looking at the statistics (Fig. 97) in the region near the entrance it is evident that the simulated mean particle velocity is slightly higher and the fluctuations are slightly lower than the experimental data. As will be shown in § 8.7.2.3 the particle statistics can be improved by taking the effect of the rough pipe walls on the particle motion into account.

Figures 98 and 99 display the mean streamwise and mean radial velocity of the 60 μm particles. It is clearly visible that for the H2 and H4 computations a jet-like structure is retained by the particles further downstream compared to the one-way coupled simulations. Independent of whether inter-particle collisions are considered or not, the results of both LES predictions are in excellent agreement with the measurements. Interestingly, for the H2 and H4 cases the particles still have a positive radial velocity (Fig. 99) at the measurement plane $z^*/R_{pipe}^* = 32$. Contrarily, for the MH1 case the particles located close to the axis in the shear layer behind R1 are directed towards the chamber center by the inward curved streamlines (Fig. 81(b)).

Figure 100 depicts the streamwise velocity fluctuations of the 60 μm particles. Similar to the streamwise velocity fluctuations of the continuous phase (Fig. 95) the deviations between the experiment of Borée et al. (2001) and the H2 and H4 cases found in the planes $z^*/R_{pipe}^* = 16$ and 20 are consistent with the shift of the maximum particle velocity fluctuations observed on the axis (Fig. 97(b)). This again indicates that the axial extension of the recirculation zone R1 is slightly underpredicted in the simulations. For the radial velocity fluctuations of the 60 μm particles (Fig. 101) good agreement of the H2/H4 predictions with the experiments is found in all planes investigated by Borée et al. (2001).

8.7.1.4 Influence of the Particle Diameter d_p^* on the Particle Motion

In this section the axial evolution of the mean streamwise velocity, the streamwise and radial fluctuations for three different particle classes are compared with the same quantities of the continuous flow. Furthermore, the mean drift between the size classes for the H4 case are also shown in Fig. 102. The mean drift between the size classes i and j is defined as the difference between the mean streamwise particle velocity $\langle u_{pzi}^* \rangle$ of the class i and the mean streamwise particle velocity $\langle u_{pzj}^* \rangle$ of the class j at a given point of the domain. The high mass loading is selected because the particle statistics on the axis are smoother than those at the moderate mass loading case. The reason is that a higher number of particles are available to generate the statistics. Note, however, that the same trends with respect to the diameter d_p^* to be discussed for H4 can be observed for the M4 case. The size classes chosen are $d_p^* = 20, 40$ and $60 \mu\text{m}$ which allow to outline the effect of inertia on the particle motion since the particle Stokes numbers St differ an order of magnitude between the smallest diameter ($d_p^* = 20 \mu\text{m}$, $St = 0.4$) and the biggest diameter ($d_p^* = 60 \mu\text{m}$, $St = 3.9$) selected (see Table 5). Unfortunately, due to the

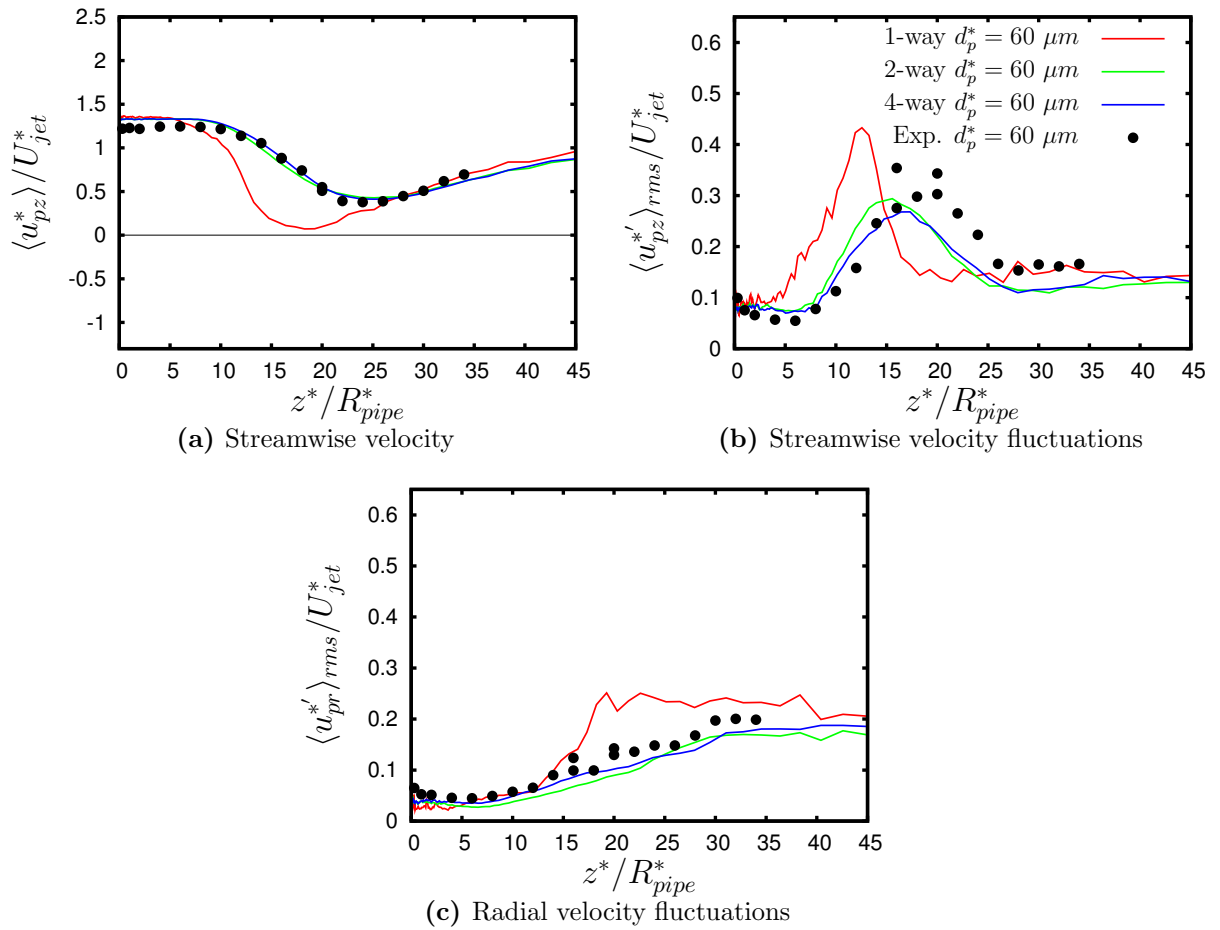


Figure 97: Axial evolution of the streamwise velocity and the streamwise and radial velocity fluctuations of particles with a diameter of $d_p^* = 60 \mu m$ at $\eta = 110\%$; experimental data by Borée et al. (2001).

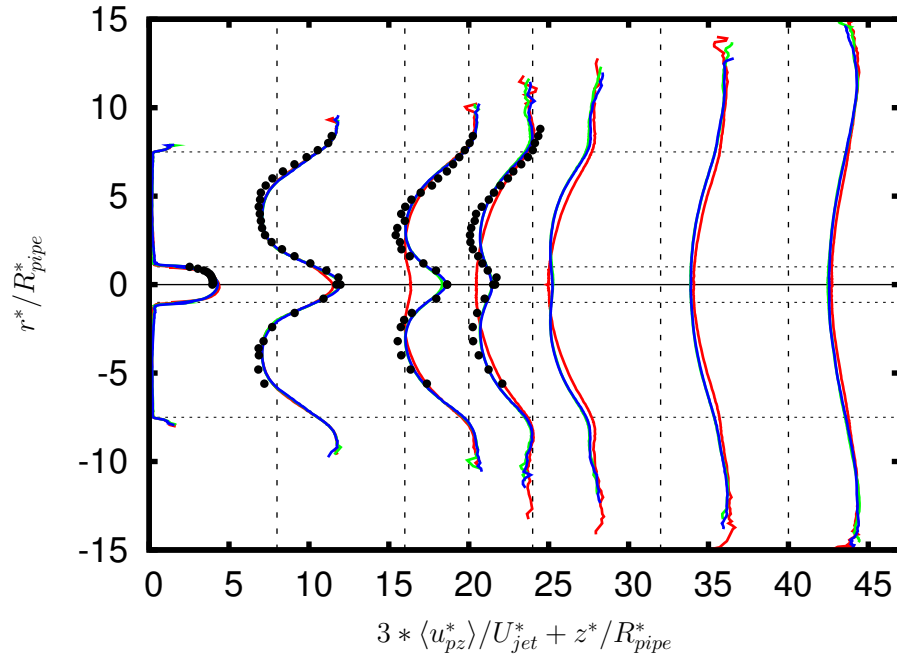


Figure 98: $\eta = 110\%$: Streamwise velocity of particles with a diameter of $d_p^* = 60 \mu\text{m}$ at the measurement planes $z^*/R_{pipe}^* = 0.3, 8, 16, 20, 24, 32$ and 40 . Red line: 1-way, green line: 2-way, blue line: 4-way, filled symbols: experiment by Borée et al. (2001).

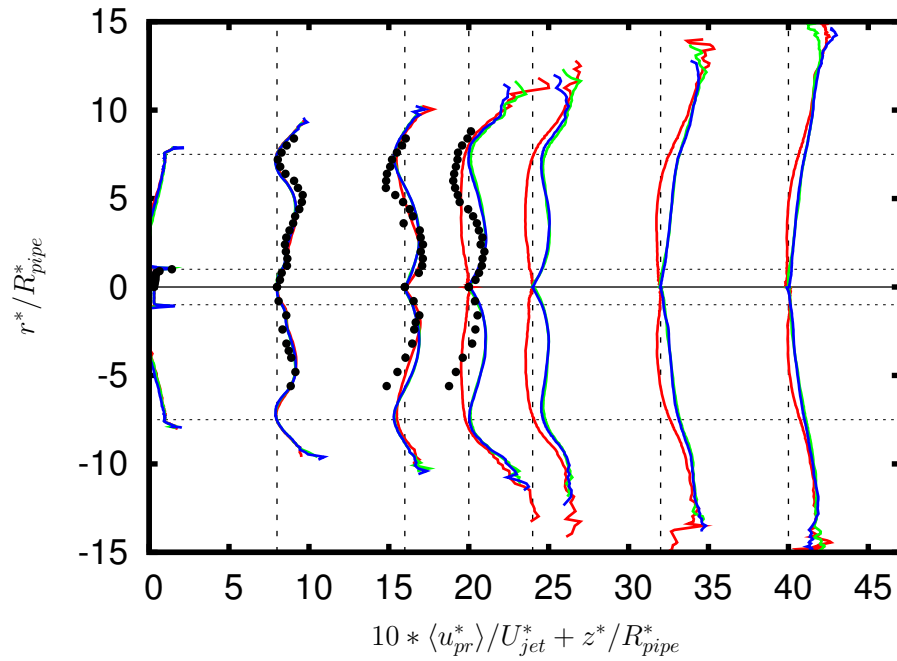


Figure 99: $\eta = 110\%$: Radial velocity of particles with a diameter of $d_p^* = 60 \mu\text{m}$ at the measurement planes $z^*/R_{pipe}^* = 0.3, 8, 16, 20, 24, 32$ and 40 . Red line: 1-way, green line: 2-way, blue line: 4-way, filled symbols: experiment by Borée et al. (2001).

small number frequency $\tilde{f}_N(d_{p,i})$ of the particles larger than $d_p^* = 60 \mu\text{m}$ it is not possible to obtain reasonably converged statistics for these classes (Table 5). The objective is

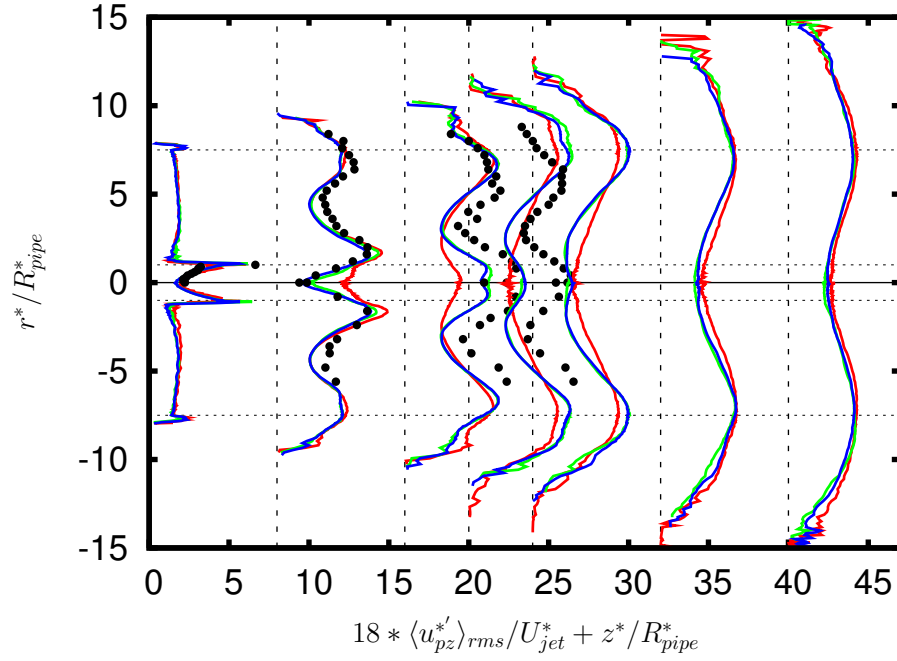


Figure 100: $\eta = 110\%$: Streamwise velocity fluctuations of particles with a diameter of $d_p^* = 60 \mu\text{m}$ at the measurement planes $z^*/R_{pipe}^* = 0.3, 8, 16, 20, 24, 32$ and 40 . Red line: 1-way, green line: 2-way, blue line: 4-way, filled symbols: experiment by Borée et al. (2001).

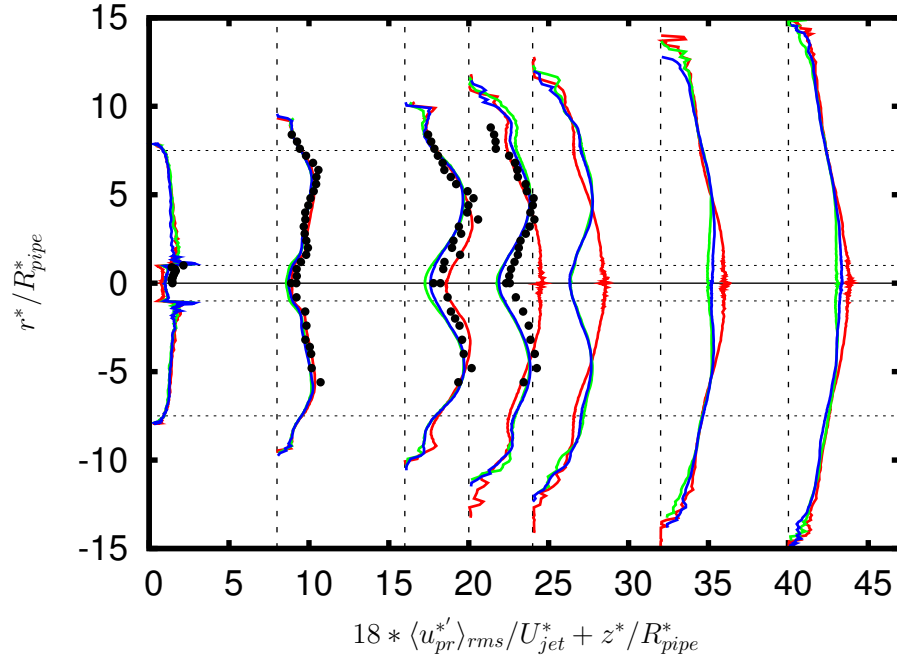


Figure 101: $\eta = 110\%$: Radial velocity fluctuations of particles with a diameter of $d_p^* = 60 \mu\text{m}$ at the measurement planes $z^*/R_{pipe}^* = 0.3, 8, 16, 20, 24, 32$ and 40 . Red line: 1-way, green line: 2-way, blue line: 4-way, filled symbols: experiment by Borée et al. (2001).

to demonstrate that the whole numerical methodology presented works well for different

particle sizes.

Figure 102(a) shows the axial evolution of the mean particle velocity compared with the mean streamwise fluid velocity¹⁷. It is obvious that after being injected into the chamber both fluid and particles keep a nearly constant velocity until $z^*/R_{pipe}^* \approx 8$. The influence of inertia is clearly manifested with increasing particle diameter d_p^* . While the 20 μm particles closely follow the fluid motion, the 60 μm particles retain for a longer distance the initial velocity of the entrance and reach their minimum velocity further downstream than the smaller particles. This trend is clearly visible for both data, the experimental and the numerical results. Figure 102(b) depicts the axial evolution of the particle streamwise velocity fluctuations compared with the streamwise fluid velocity fluctuations. Here a clear trend is observed in the wake region W behind R1 (see Fig. 81(b)). The smallest particles considered can closely follow the fluid motion and the amplitude of the streamwise particle velocity fluctuations is similar to the magnitude of the fluid velocity fluctuations. Owing to their higher inertia the 60 μm particles, however, are less influenced by the small turbulent scales leading to a reduction of the fluctuations. A similar trend is observed for the fluctuations in radial direction (Fig. 102(c)). The smallest particles can closely follow the small turbulent structures leading to higher fluctuations than for bigger particles. Overall, good agreement with the experiment of Borée et al. (2001) is found.

Figure 102(d) displays the mean drift between particle classes. As already judged from the mean streamwise particle velocity (Fig. 102(a)), the mean drift is nearly zero in the jet region close to the entrance and reaches its maximum in the region between the end of R1 and R2. Here the 20 μm particles closely follow the fluid motion while the 60 μm particles still preserve partly the initial velocity at the entrance yielding the largest drift. In the wake region, where the streamwise fluid velocity gradient is small enough that also the bigger particles can readjust to the carrier phase, the mean drift almost vanishes. These observations are underpinned by both, simulations and experiment.

8.7.1.5 Influence of the Collisions on the Particle Dynamics

In this section an explanation for the minor importance of the particle–particle collisions on the particle dynamics even for the high mass loading case is given. For this purpose, the total number of particle–particle collisions N_{ctot} found in each control volume (CV) during the averaging period $N \Delta t$ ($N = 90,000$ averaging time steps) is determined. Furthermore, the total number of particles N_{ptot} found in the same CV is counted during the same averaging period. That allows to predict an average number of particles $N_{pcv} = N_{ptot}/N$ in the CV. Note that no distinction between classes is made. The ratio N_{ctot}/N_{pcv} describes the total number of collisions found per particle in each CV of the computational domain. The dimensionless collision frequency $f_c = f_c^* R_{pipe}^*/U_{jet}^*$, i.e., the number of collisions per particle and time, is obtained by dividing the total number of collisions per particle in a CV (N_{ctot}/N_{pcv}) by the averaging time $N \Delta t$:

$$f_c = \frac{N_{ctot}/N_{pcv}}{N \Delta t} = \frac{N_{ctot}}{N_{ptot} \Delta t}. \quad (8.13)$$

According to Sommerfeld (2000) the threshold between dilute and dense two–phase flows is at $f_c^* \cdot \tau_p^* \approx 1$. For $f_c^* \cdot \tau_p^* \geq 1$, the particles do not have enough time to readjust to

¹⁷Note that for Figs. 102(a), (b) and (c) the legend is displayed only once since the presentation of the results is not changed.

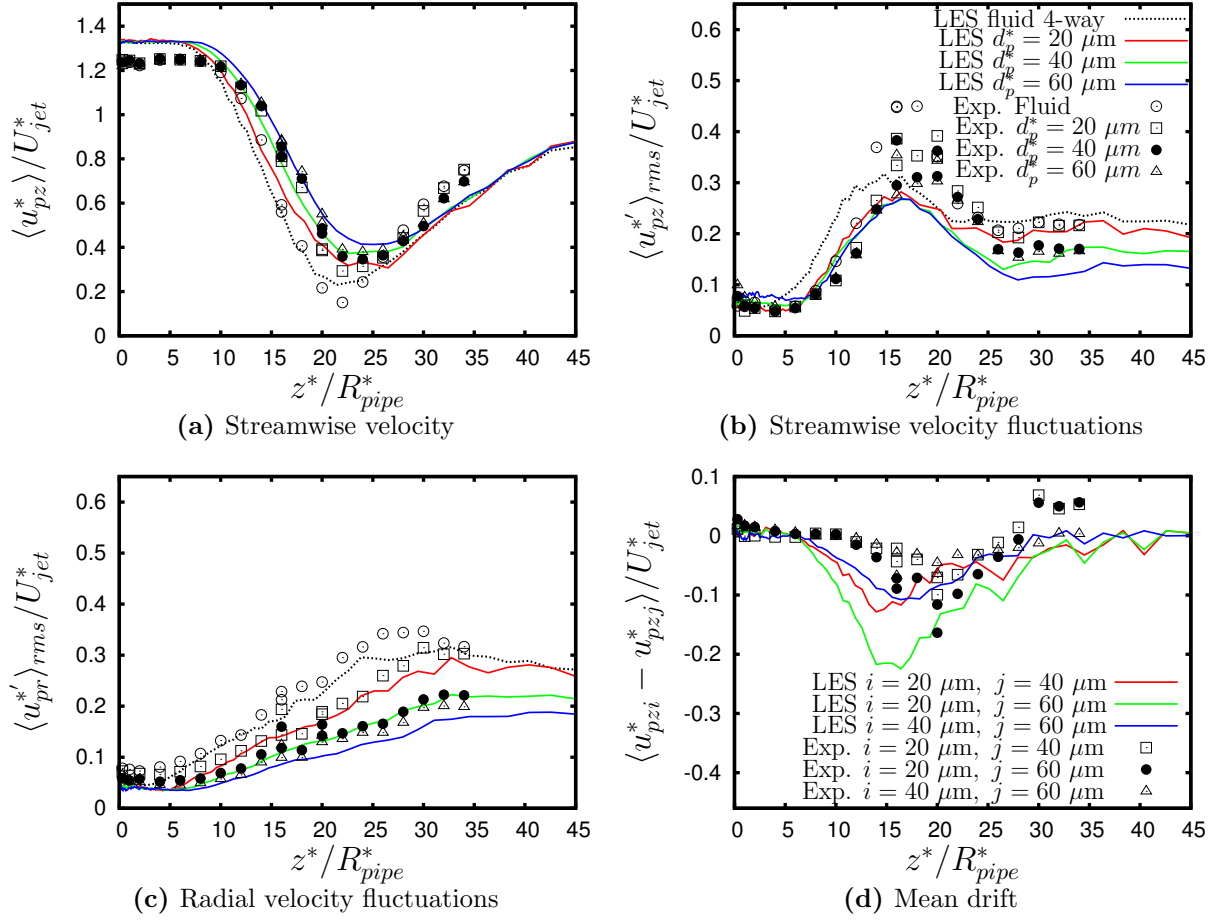


Figure 102: Axial evolution of the streamwise velocity, the streamwise and radial velocity fluctuations of the particulate phase with a diameter of $d_p^* = 20, 40$ and $60 \mu\text{m}$ compared with the continuous phase (same legend for (a), (b) and (c)) and the mean drift between particle classes i and j at $\eta = 110\%$; experimental data by Borée et al. (2001).

the carrier phase between two subsequent collisions and therefore the particle dynamics is significantly influenced by collisions. For the following considerations the relaxation time τ_{p60}^* of the $60 \mu\text{m}$ particles (see Table 5), i.e., the class compared in the former sections with the experiments of Borée et al. (2001) and also the size class with the biggest diameter having a relevant number frequency $f_N(d_{p,i}^*)$ is used to estimate the importance of the collisions on the dynamics of this class. Figure 103 displays the contour plot of the product of the collision frequency f_c^* times the relaxation time τ_{p60}^* of the $60 \mu\text{m}$ particles for the M4 and H4 cases. Note, that the product $f_c^* \cdot \tau_{p60}^*$ is an upper bound estimation of the influence of the collisions on the motion of the $60 \mu\text{m}$ particles. Since the number distribution $q_{0,i}(d_{p,i}^*)$ of the $60 \mu\text{m}$ particles (see Table 5) is less than unity, only a small amount of the totally counted collisions N_{tot} in a control volume involves the $60 \mu\text{m}$ particles and hence the real collision frequency of the f_{c60}^* $60 \mu\text{m}$ particles is certainly lower than the total collision frequency f_c^* .

For the moderate mass loading (Fig. 103(a)) the region where most of the inter-particle collisions occur coincides with the region of the maximum volume fraction (see Fig. 81(g)). The product $f_c^* \cdot \tau_{p60}^*$ is about one order of magnitude smaller than unity confirming the

negligible importance of inter-particle collisions on the particle statistics presented in § 8.7.1.2. This result is contradictory to the considerations of Borée et al. (2001) who estimated that collisions should be important already at this moderate mass loading.

For the high mass loading (see Fig. 103(b)) the maximum collision frequency is found between the end of R2 and the end of R1 on the axis (see Fig. 81(b)). Interestingly, it does not coincide with the maximum of the particle volume fraction Φ located for this case at the chamber entrance on the axis (see Fig. 81(g)). However, the position of the maximum collision frequency is in accordance with the location of the maximum drift between the size classes (Fig. 102(d)) and the maximum of the particle streamwise fluctuations (Fig. 102(b)) on the axis. According to Borée et al. (2001) and Borée and Caraman (2005) the collision frequency f_c^* is a function of the averaged particle velocity fluctuations $\langle \sigma_p^{*2} \rangle = 1/3(\langle u_{pz}^{*2} \rangle + \langle u_{pr}^{*2} \rangle + \langle u_{p\phi}^{*2} \rangle)$, the mean drift between particle classes and the particle volume fraction. The volume fraction is maximal at the chamber entrance, whereas the maximum of the averaged particle velocity fluctuations and the mean drift are found further downstream between $15 \leq z^*/R_{pipe}^* \leq 20$. Obviously, the influence of the particle fluctuations $\langle \sigma_p^{*2} \rangle$ (Fig. 102(b)) and the influence of the mean drift (Fig. 102(d)) on the collision frequency f_c^* compensate the contribution of the decreasing volume fraction leading to a downstream shift of the maximum number of collisions away from the entrance. Also in the H4 case the product $f_c^* \cdot \tau_{p60}^*$ is less than unity in the whole chamber explaining the results shown in § 8.7.1.3, where the differences between the H2 and the H4 cases are found to be negligible. Hence inter-particle collisions are still of minor importance also for $\eta = 110\%$.

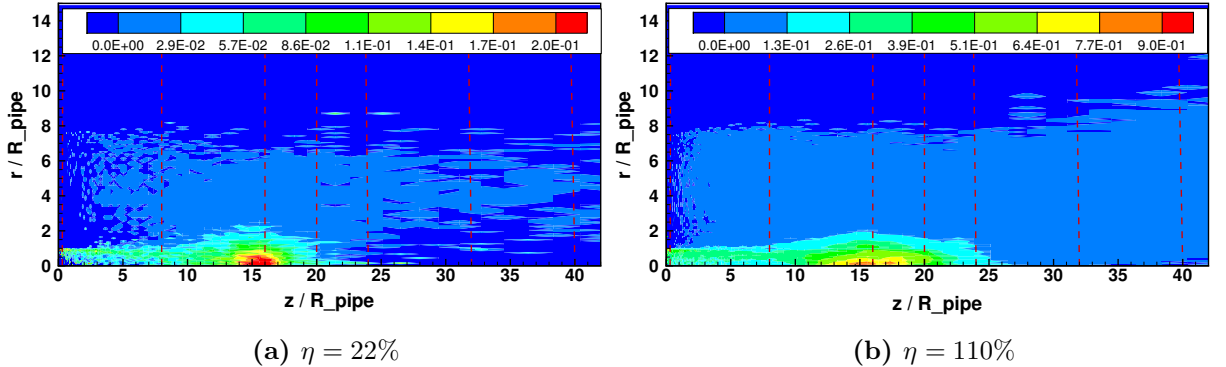


Figure 103: Contour plot of the product $f_c^* \cdot \tau_{p60}^*$.

8.7.2 Influence of the Resolution and the Inflow Boundary Conditions

In the following the influence of the resolution and the inflow boundary conditions (especially the one for the annular flow) is evaluated. In order to study the aforementioned influences the moderate mass loading case $\eta = 22\%$ is analyzed in detail. For $\eta = 110\%$ only the statistics on the axis are shown to emphasize the influence of the inflow conditions applied for the inner pipe flow. Very similar discrepancies between the statistics computed for the COARSE AF-PER case (the M4 and H4 cases discussed in the former chapter) and for the FINE 1 AF-PER and FINE 2 AF-EXP cases in the cross-sections can be found for the moderate mass loading $\eta = 22\%$ and the high mass loading $\eta = 110\%$. Therefore, no substantial information is lost by omitting the plots comparing the simulations with the experiment at the measurement planes $z^*/R_{pipe}^* = 0.3, 8, 16, 20$ and 24 .

8.7.2.1 Overview of the Flow Structure

To get a first overview of the influence of the resolution and the boundary conditions applied for the annular flow, the streamlines of the averaged fluid flow and the contour plot of the radial velocity fluctuations $\langle u_{fr}^* \rangle_{rms} / U_{jet}^*$ of the fluid are analyzed. Note that the forces displacing the particles and the parameters modeling the velocity changes after a particle–particle collision are different for the simulations used to generate the inflow at the pipe inlet for the COARSE grid and the grids denoted FINE 1 and FINE 2 (see § 7.7.2 for details and the motivations for the choices made). Despite the differences in the numerical setup the statistics computed for the four different setups compared in the following are very similar in the region closed to the axis near the entrances. Therefore, the influence of the pipe flow on the qualitative differences found between the different cases shown in Fig. 104 can be disregarded a–priori.

Figure 104 shows the influence of the resolution and the inflow conditions for the annular flow on the streamlines of the averaged flow and the radial velocity fluctuations $\langle u_{fr}^* \rangle_{rms} / U_{jet}^*$ for $\eta = 22\%$. COARSE, FINE 1 and FINE 2 denote the coarse, the fine and the second fine grid where the grid spacing in axial direction is refined in the region between the two stagnation points, respectively (see § 7.7.2). AF–PER and AF–EXP represent the inflow conditions for the annular flow generated by a simulation using periodic boundary conditions and a simulation for which the mean profile is taken from the experiment and the fluctuations are superimposed (see § 7.7.2).

Comparing Figs. 104(a) and (b) with Figs. 104(c) and (d) it is evident that the resolution has a drastic effect on the overall flow structure in the combustion chamber. Surprisingly, the radial velocity fluctuations $\langle u_{fr}^* \rangle_{rms} / U_{jet}^*$ are drastically reduced for the FINE 1 grid compared with the COARSE grid. This observation is unexpected since for a finer resolution the resolved part of the turbulent spectrum should be larger. Therefore, the velocity fluctuations should increase. Here the opposite is the case. Note, however, that the contours of $\langle u_{fr}^* \rangle_{rms} / U_{jet}^*$ for all cases depicted in Fig. 104 are very similar in the region closed to the entrance until approximately $z^* / R_{pipe}^* \approx 8$ and in the annular flow A until the shear layer developing between the recirculation region R1 and A.

The resolution has also a big influence on the streamlines (see Figs. 104(a) and (c)). For the COARSE grid the region between the two stagnation points S1 and S2 is shorter than for the FINE 1 grid. For both grids the first stagnation point S1 is located approximately at the same axial position. However, for the FINE 1 grid the recirculation region R1 extends further downstream than for the COARSE grid. This leads to a downstream shift of S2 which is located at $z^* / R_{pipe}^* \approx 20$ for the COARSE case and $z^* / R_{pipe}^* \approx 27$ for the FINE 1 case. The elongation of R1 for the FINE 1 grid is probably caused by the drastic reduction of the radial velocity fluctuations near the axis. Especially in the region near S2, large radial velocity fluctuations in the COARSE case cause a strong momentum exchange between R1 and the annular flow A leading to a reduction of R1. This big difference of the overall flow structure between the COARSE and the FINE 1 grid can probably (at least partially) explained by the radial near–axis resolution (see Fig. 42(c)). Since the resolution near the axis of the COARSE grid is finer than the resolution of FINE 1 grid, the momentum exchange in radial direction in the region near the axis is larger for COARSE compared with FINE 1. This results in a better mixing of the recirculation region R1 and the annular flow A in the near–axis region around S2. Finally, this causes a shortening of R1 in case of the COARSE grid compared with the FINE 1 grid and a reduction of the distance between S1 and S2.

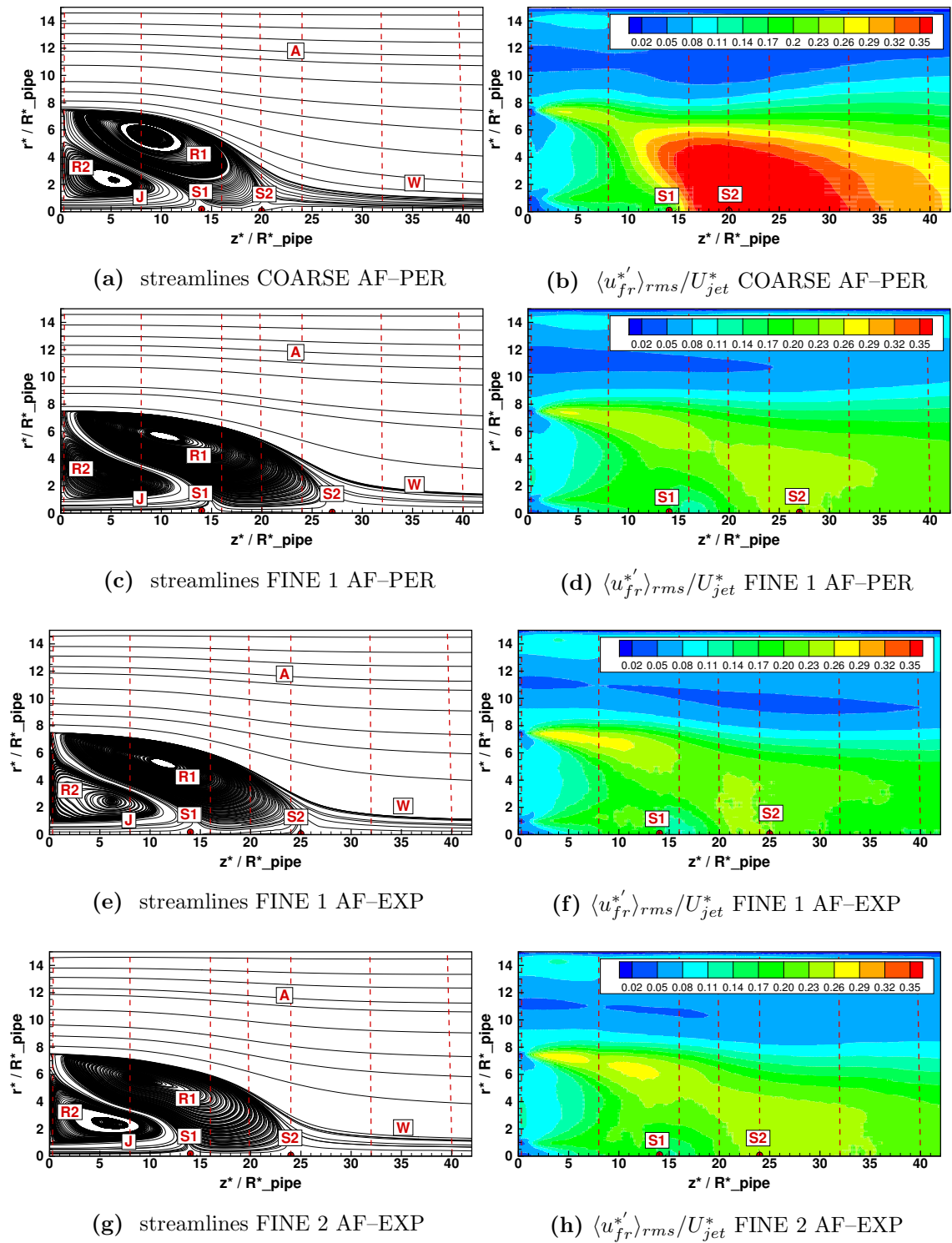


Figure 104: $\eta = 22\%$: Influence of the resolution and the inflow conditions of the annular flow on the streamlines and the radial velocity fluctuations $\langle u_{fr}^{*'} \rangle_{rms} / U_{jet}^*$. (a, b) COARSE grid (c, d) FINE 1, inflow generated by a simulation with periodic boundary conditions; (e, f) FINE 1, inflow generated by imposed mean velocity and fluctuations taken from the experiments of Borée et al. (2001); (g, h) FINE 2, inflow generated by imposed mean velocity and fluctuations taken from the experiments of Borée et al. (2001).

The influence of the inflow boundary conditions can be observed when comparing

Figs. 104(c) and (d) with Figs. 104(e) and (f). It is evident that the radial velocity fluctuations $\langle u_{fr}^{*'} \rangle_{rms} / U_{jet}^*$ in the shear layer between R1 and the annular flow until $z^*/R_{pipe}^* \leq 11$ are larger in the case FINE 1 AF-EXP compared with the FINE 1 AF-PER case. This increased velocity fluctuations cause an enhanced momentum transfer between R1 and A. Therefore, the second stagnation point S2 moves from $z^*/R_{pipe}^* \approx 27$ in the FINE 1 AF-PER case to $z^*/R_{pipe}^* \approx 25$ in the FINE 1 AF-EXP case.

The refinement of the grid spacing in the region between the two stagnation points S1 and S2 has only a small effect on the overall flow structure. This becomes evident when comparing Figs. 104(e) and (f) with Figs. 104(g) and (h). For the FINE 2 AF-EXP case the second stagnation point is slightly shifted upstream compared with the FINE 1 AF-EXP case. Furthermore, the radial velocity fluctuations $\langle u_{fr}^{*'} \rangle_{rms} / U_{jet}^*$ are slightly increased in the near-axis region after S2 for the FINE 2 AF-EXP case compared with the FINE 1 AF-EXP case.

8.7.2.2 Influence of the Resolution and the Inflow Boundary Conditions on the Fluid and Particle Statistics for $\eta = 22\%$

Continuous Phase

Figure 105 shows the influence of the resolution and the inflow conditions on the axial evolution of the streamwise velocity and the streamwise and radial velocity fluctuations of the continuous phase at $\eta = 22\%$. Note that the legend is displayed in Fig. 105(b). The representation of the test cases and of the experimental data does not change within the entire section. Therefore the legend is visualized only ones.

As already visible in Fig. 104 it is evident that the resolution has a dramatic effect on the length of the region between the stagnation points S1 and S2. The compatible observation can be made from the axial evolution of the streamwise fluid velocity on the axis (see Fig. 104(a)). For all four cases examined the axial position of S1 is similar, i.e., it lies at $z^*/R_{pipe}^* = 14.1, 15.3, 15.1$ and 14.2 for the COARSE AF-PER, FINE 1 AF-PER, FINE 1 AF-EXP and FINE 2 AF-EXP cases, respectively. However, the position of S2 differs considerably for the four cases, i.e., it lies at $z^*/R_{pipe}^* = 20.3, 26.9, 25.1$ and 24.0 for the COARSE AF-PER, FINE 1 AF-PER, FINE 1 AF-EXP and FINE 2 AF-EXP cases, respectively. That means that, when the two cases where the inflow conditions for the annular flow are generated by means of simulations with periodic boundary conditions are compared with each other, the distance between the stagnation points S1 and S2 increases from $z^*/R_{pipe}^* = 6.21$ for the COARSE AF-PER case to $z^*/R_{pipe}^* = 11.6$ for the FINE 1 AF-PER case. This observation is consistent with the evolution of the radial velocity fluctuations $\langle u_{fr}^{*'} \rangle_{rms} / U_{jet}^*$ on the axis (see Fig. 104(c)). It is evident that for the COARSE AF-PER case $\langle u_{fr}^{*'} \rangle_{rms} / U_{jet}^*$ drastically increase after the first stagnation point S1. This leads to a strong momentum transfer in radial direction which causes a reduction of the length of R1 (Fig. 104). For the FINE 1 AF-PER case, however, the radial velocity fluctuations slightly decrease after S1 (see Fig. 104(c)). The minimum of $\langle u_{fr}^{*'} \rangle_{rms} / U_{jet}^*$ is reached approximately at the same location as the minimum streamwise velocity (see Fig. 104(a)). After that point, the radial velocity fluctuations slightly rise but the maximum remains approximately one half of the maximum of $\langle u_{fr}^{*'} \rangle_{rms} / U_{jet}^*$ for the COARSE AF-PER case. The lower radial velocity fluctuations in the FINE 1 AF-PER case compared with the COARSE AF-PER case lead to a smaller momentum transfer in radial direction and therefore a elongation of R1 (see Fig. 104).

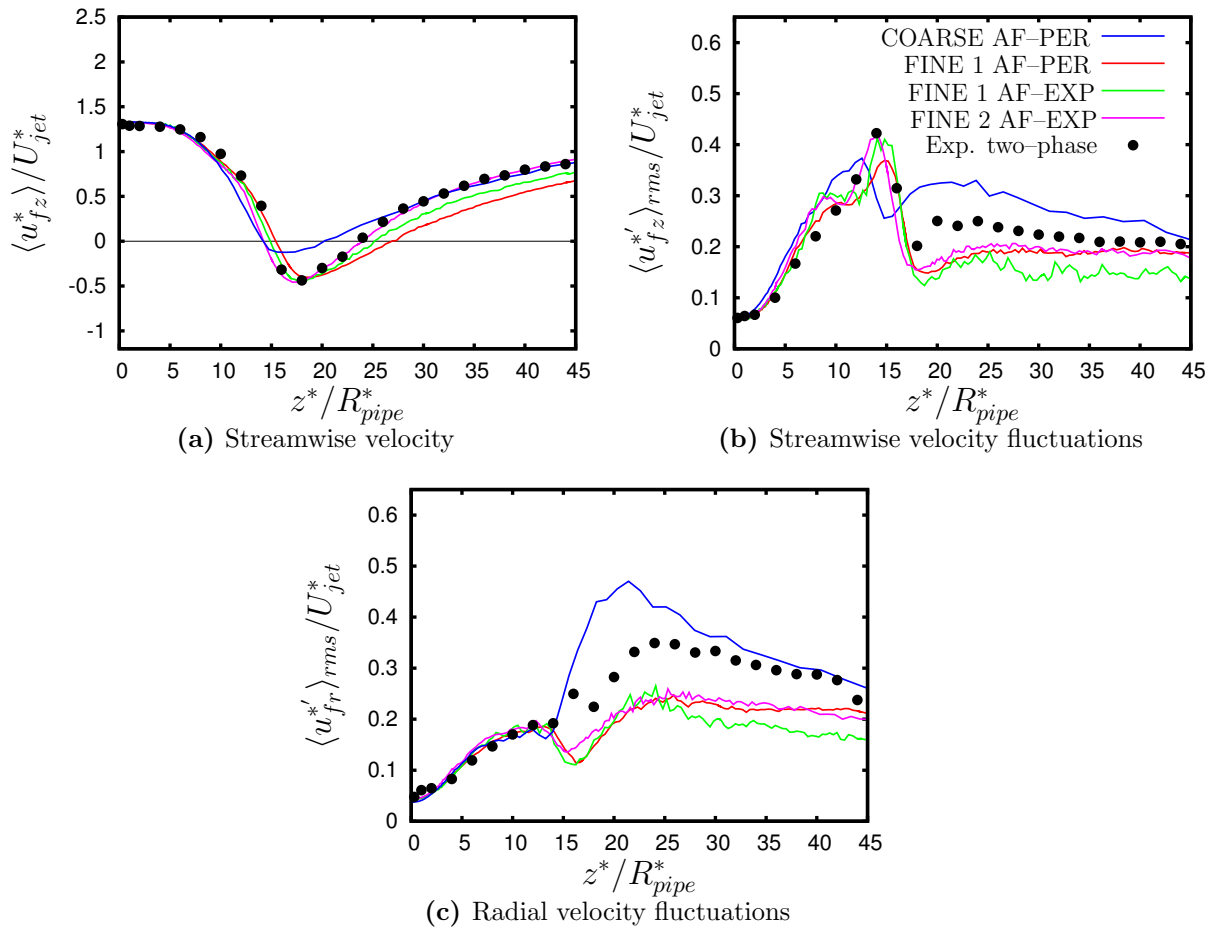


Figure 105: Influence of the resolution and the inflow conditions on the axial evolution of the streamwise velocity and the streamwise and radial velocity fluctuations of the continuous phase at $\eta = 22\%$; experimental data by Borée et al. (2001).

The resolution has also an influence on the streamwise velocity fluctuations $\langle u_{fz}^{*'} \rangle_{rms} / U_{jet}^*$ on the axis (see Fig. 104(b)). However, the effect is not as dramatic as for $\langle u_{fz}^{*'} \rangle_{rms} / U_{jet}^*$. Comparing the streamwise velocity fluctuations of the COARSE AF-PER case with the same quantity for the FINE 1 AF-PER case, it is obvious that the maximum is slightly shifted downstream. Furthermore, the strong decrease of $\langle u_{fz}^{*'} \rangle_{rms} / U_{jet}^*$ observed after its maximum is more pronounced for the FINE 1 AF-PER case than for the COARSE AF-PER case.

Regarding the influence of the inflow conditions for the annular flow, it is evident that they are less influential on the statistics on the axis than the change of the grid. When comparing the red line in Fig. 104(a) with the green line, it can be observed that imposing the mean profile and the velocity fluctuations obtained by the experiment leads to a slightly faster recovery of the time-averaged streamwise velocity than generating the inflow conditions by simulations with periodic boundary conditions. The agreement with the experimentally measured mean streamwise velocity can be further improved by accumulating the grid points in the region between S1 and S2 (FINE AF-EXP case: magenta line in Fig. 104(a)). An analogous observation can be made for the streamwise velocity fluctuations (Fig. 104(b)). Using the improved inflow conditions (compare the red line with the green line in Fig. 104(b)) the maximum of $\langle u_{fz}^{*'} \rangle_{rms} / U_{jet}^*$ slightly increases.

The agreement with the experimental data is further improved by concentrating the grid points in the region between S1 and S2 (magenta line in Fig. 104(b)).

Figure 106 shows the influence of the resolution and the inflow conditions on the mean axial fluid velocity at all measurement planes investigated by Borée et al. (2001) for $\eta = 22\%$, i.e., $z^*/R_{pipe}^* = 0.3, 8, 16, 20, 24, 32$ and 40 . The main conclusion which can be drawn is that the flow in the outer region can be considerably improved by imposing the measured mean profile and the fluctuations at the inflow of the annular region. For the two cases where the inflow is generated by the AF-EXP method described in § 3.3.3.2 (green and magenta line in Fig. 106) the mean streamwise fluid velocity is reduced in the annular flow region compared with the simulations for which the inflow of the annular flow is generated by the AF-PER method described in § 3.3.3.1 (blue and red line in Fig. 106). This finding further confirms the conjecture of Borée et al. (2001) who assumed that the development length of the annular flow was too short to ensure a fully developed flow. Note that the good agreement of the mean streamwise velocity on the axis for the FINE cases (see Fig. 105(a)) can be observed also in the near-axis region of the measurement planes at $z^*/R_{pipe}^* = 16$ and 20 : While the mean streamwise velocity at these planes is overpredicted for the COARSE AF-PER case, the same quantity is well captured for the FINE cases.

Figure 107 illustrates the influence of the resolution and the inflow conditions on the mean radial fluid velocity at the same measurement planes as before. Only small differences between the four cases analyzed here can be found for this quantity. The differences among the four simulations compared are confined in the region near the shear layer developing between the recirculation region R1 and the annular flow (see the region around $r^*/R_{pipe}^* \approx 5$) in the measurement planes located at $z^*/R_{pipe}^* = 20$ and 24 . In these measurement planes the radial velocity has a more pronounced negative component for the cases where the experimental data are used to generate the inflow conditions for the annular flow.

Figure 108 shows the influence of the resolution and the inflow conditions on the axial fluid velocity fluctuations at all measurement planes investigated by Borée et al. (2001) for $\eta = 22\%$. It is evident that the strong dependence of this quantity from the grid resolution already observed for the evolution of $\langle u_{fz}^* \rangle_{rms}/U_{jet}^*$ on the axis (see Fig. 104(a)), is also found at a considerable distance away from the axis. Surprisingly, the decrease of $\langle u_{fz}^* \rangle_{rms}/U_{jet}^*$ for the finer grids (FINE 1 and FINE 2) compared with the COARSE grid can be observed only at the measurement planes located at $z^*/R_{pipe}^* = 16, 20, 24, 32$ and 40 . The discrepancies between the four cases investigated at the planes located closer to the entrance, i.e., $z^*/R_{pipe}^* = 0.3$ and 8 , are minor. Note that for the grids FINE 1 and FINE 2 the radial position of the maximum of $\langle u_{fz}^* \rangle_{rms}/U_{jet}^*$ found in the shear layer developing between R1 and A is better captured than for the grid COARSE: For the COARSE grid the maximum lies at approximately the same radial position for all measurement planes analyzed. For FINE 1 and FINE 2 the maximum of $\langle u_{fz}^* \rangle_{rms}/U_{jet}^*$ moves according to the measurements towards the axis for increasing axial position. The reason is that the resolution of the FINE 1 and FINE 2 grids in the region of the shear layer developing between the recirculation region R1 and the annular flow A are finer than for the COARSE grid (see Fig. 42).

Figure 109 shows the influence of the resolution and the inflow conditions on the radial fluid velocity fluctuations $\langle u_{fr}^* \rangle_{rms}/U_{jet}^*$ for $\eta = 22\%$. Similar to the streamwise velocity fluctuations also for $\langle u_{fr}^* \rangle_{rms}/U_{jet}^*$ no substantial changes between the four cases considered

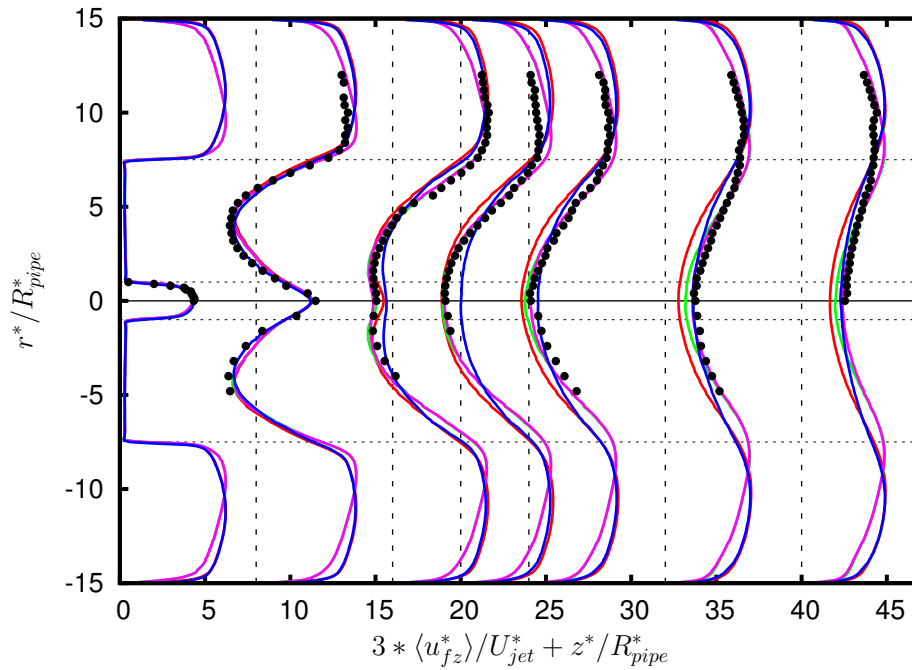


Figure 106: $\eta = 22\%$: Streamwise fluid velocity at the measurement planes $z^*/R_{pipe}^* = 0.3, 8, 16, 20, 24, 32$ and 40 . Blue line: COARSE AF-PER, red line: FINE 1 AF-PER, green line: FINE 1 AF-EXP, magenta line: FINE 2 AF-EXP, filled symbols: Exp. two-phase (Borée et al., 2001).

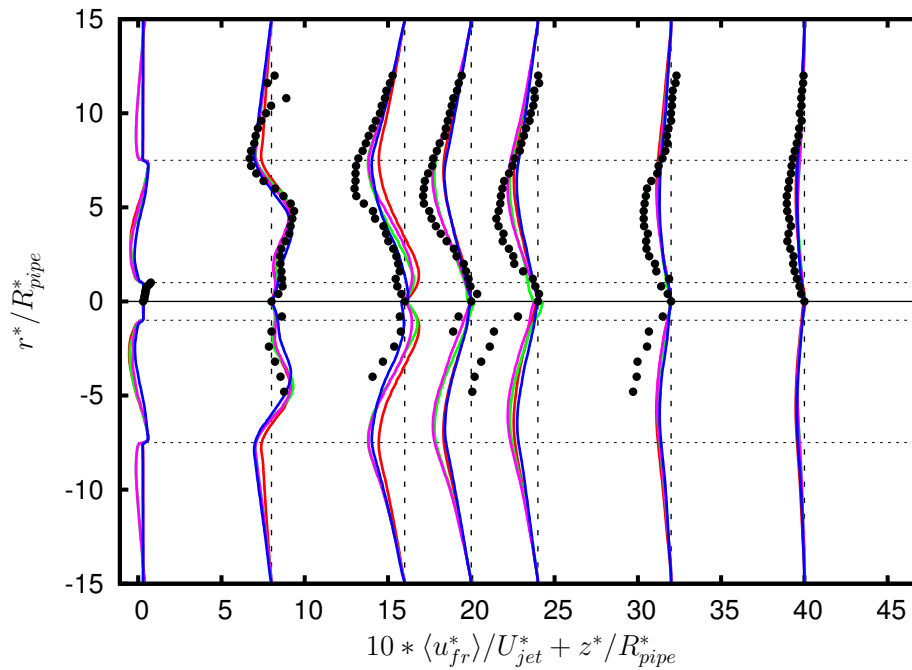


Figure 107: $\eta = 22\%$: Radial fluid velocity at the measurement planes $z^*/R_{pipe}^* = 0.3, 8, 16, 20, 24, 32$ and 40 . Blue line: COARSE AF-PER, red line: FINE 1 AF-PER, green line: FINE 1 AF-EXP, magenta line: FINE 2 AF-EXP, filled symbols: Exp. two-phase (Borée et al., 2001).

here can be observed in the planes located at $z^*/R_{pipe}^* = 0.3$ and 8 . The marked differences

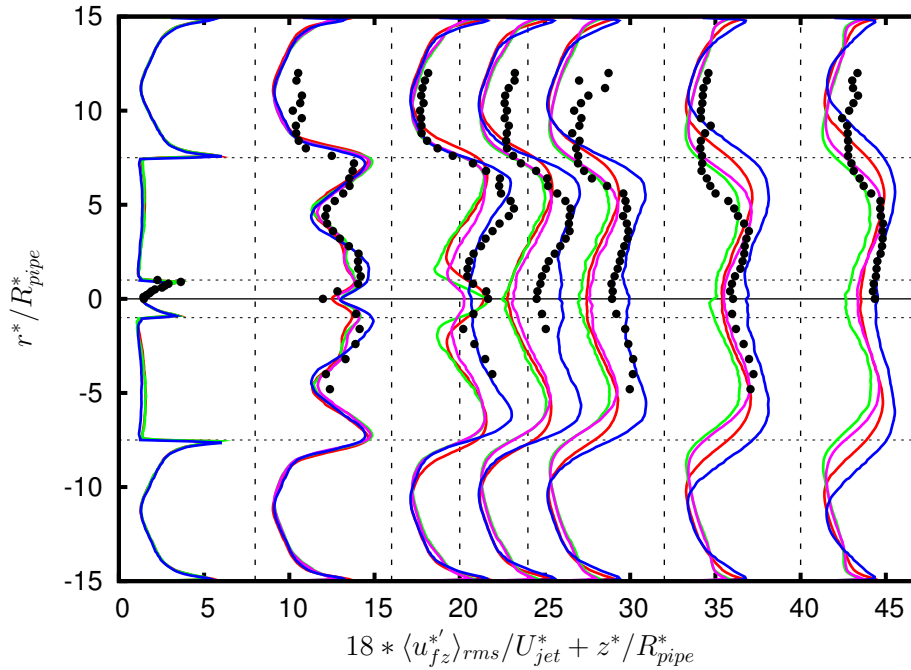


Figure 108: $\eta = 22\%$: Streamwise fluid velocity fluctuations at the measurement planes $z^*/R_{pipe}^* = 0.3, 8, 16, 20, 24, 32$ and 40 . Blue line: COARSE AF-PER, red line: FINE 1 AF-PER, green line: FINE 1 AF-EXP, magenta line: FINE 2 AF-EXP, filled symbols: Exp. two-phase (Borée et al., 2001).

between the grid COARSE and the grids FINE 1 and FINE 2 already observed in the contour plot visualized in Fig. 104 can be also found in Fig. 109: The radial velocity fluctuations predicted in the region between the shear layer and the axis by the grids FINE 1 and FINE 2 are drastically reduced compared with the simulations performed on the grid COARSE. A possible explanation is that the fluid dynamics in the region between the two stagnation points S1 and S2 is very sensitive to the resolution in radial direction. Therefore, changes of the grid spacing in this region which is characterized by strong mixing and strong momentum exchange can have a drastic effect on the overall flow pattern even far away from the axis.

Particulate Phase ($d_p^* = 60 \mu\text{m}$)

Figure 110 shows the influence of the resolution and the inflow conditions on the axial evolution of the mean particle velocity and the streamwise and radial particle fluctuations for the $60 \mu\text{m}$ particles and the mass loading $\eta = 22\%$. As for the continuous phase the legend is shown only in this figure, since the presentation of the different cases does not change throughout the section. Note that for the COARSE grid and the FINE 1 and FINE 2 grids different inflow conditions for the particles and different forces displacing the particles are used. The main differences are that for the computations with the FINE grids the wall roughness is considered for the generation of the inflow conditions while it is disregarded for the COARSE case. (see § 7.7.2 for details). Therefore, not all changes observed between the COARSE case and the three other cases analyzed here can be traced back on the resolution and the inflow conditions for the annular flow.

Figure 110(a) shows the evolution of the particle streamwise velocity along the axis for the $60 \mu\text{m}$ particles. Obviously, very good agreement is found between the FINE 2

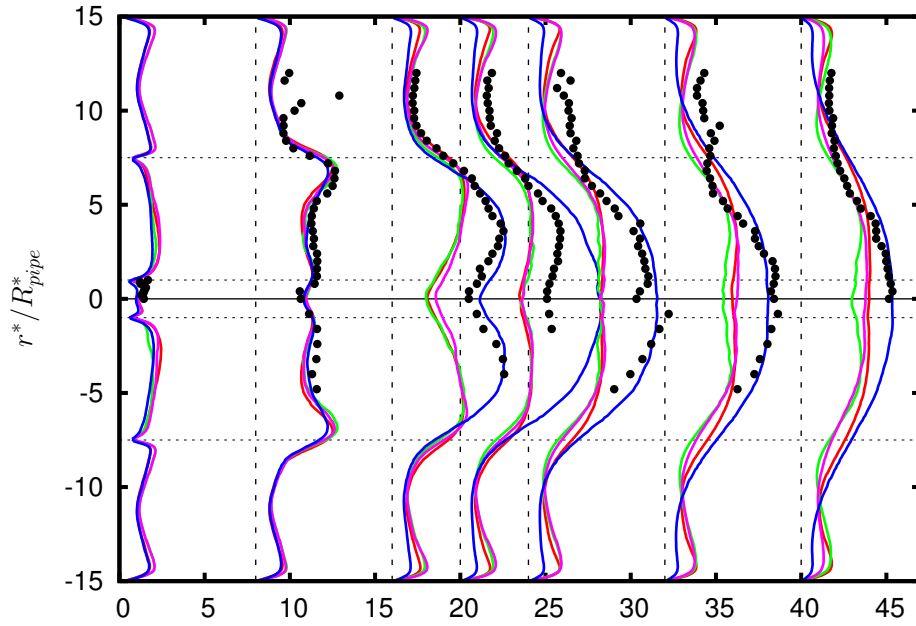


Figure 109: $\eta = 22\%$: Radial fluid velocity fluctuations at the measurement planes $z^*/R_{pipe}^* = 0.3, 8, 16, 20, 24, 32$ and 40 . Blue line: COARSE AF-PER, red line: FINE 1 AF-PER, green line: FINE 1 AF-EXP, magenta line: FINE 2 AF-EXP, filled symbols: Exp. two-phase (Borée et al., 2001).

AF-EXP case and the experiments of Borée et al. (2001). The reduction of the mean streamwise particle velocity of the simulations with the FINE 1 and FINE 2 grids compared with the simulation based on the COARSE grid in the region near the entrance can be clearly traced back to the inflow conditions for the particles. For the FINE 1 and FINE 2 grids a four-way coupled pipe flow with rough walls is used to generate the particle data injected into the chamber. For the COARSE grid a four-way coupled pipe flow with smooth walls seen by the particles is used for the generation of the inflow condition. Furthermore, for the FINE cases the entire forces displacing the particles given by eq. (4.25) are considered. For the COARSE case only the gravity, the buoyancy and the drag forces are taken into account. As already noted in the former sections, the wall roughness leads to a diminishing of the particle streamwise velocity and an increase of the particle velocity fluctuations. As visible from Fig. 110, the usage of more realistic inflow conditions for the particles leads also to a better agreement with the experimental data of Borée et al. (2001) in the region closed to the entrances for all statistical quantities shown. It is also obvious that the minimum streamwise velocity is reduced for the FINE 2 AF-EXP case compared with the COARSE case. Furthermore, it can be observed that for all FINE computations the particles have in close agreement with the experiment a slight negative streamwise velocity. For the COARSE case this is not the case. This observation can be attributed to the increased intensity of the backflow of the continuous phase for the FINE cases compared with the COARSE case (see Fig. 105(a)).

As an introducing remark for the assessment of the particle velocity fluctuations shown in Figs. 110(b) and (c), it should be mentioned that the averaging volume on the axis is quite small compared with regions farther away from it. Therefore, the second order statistics on the axis are not completely smooth.

Figure 110(b) shows the evolution of the particle streamwise velocity fluctuations along

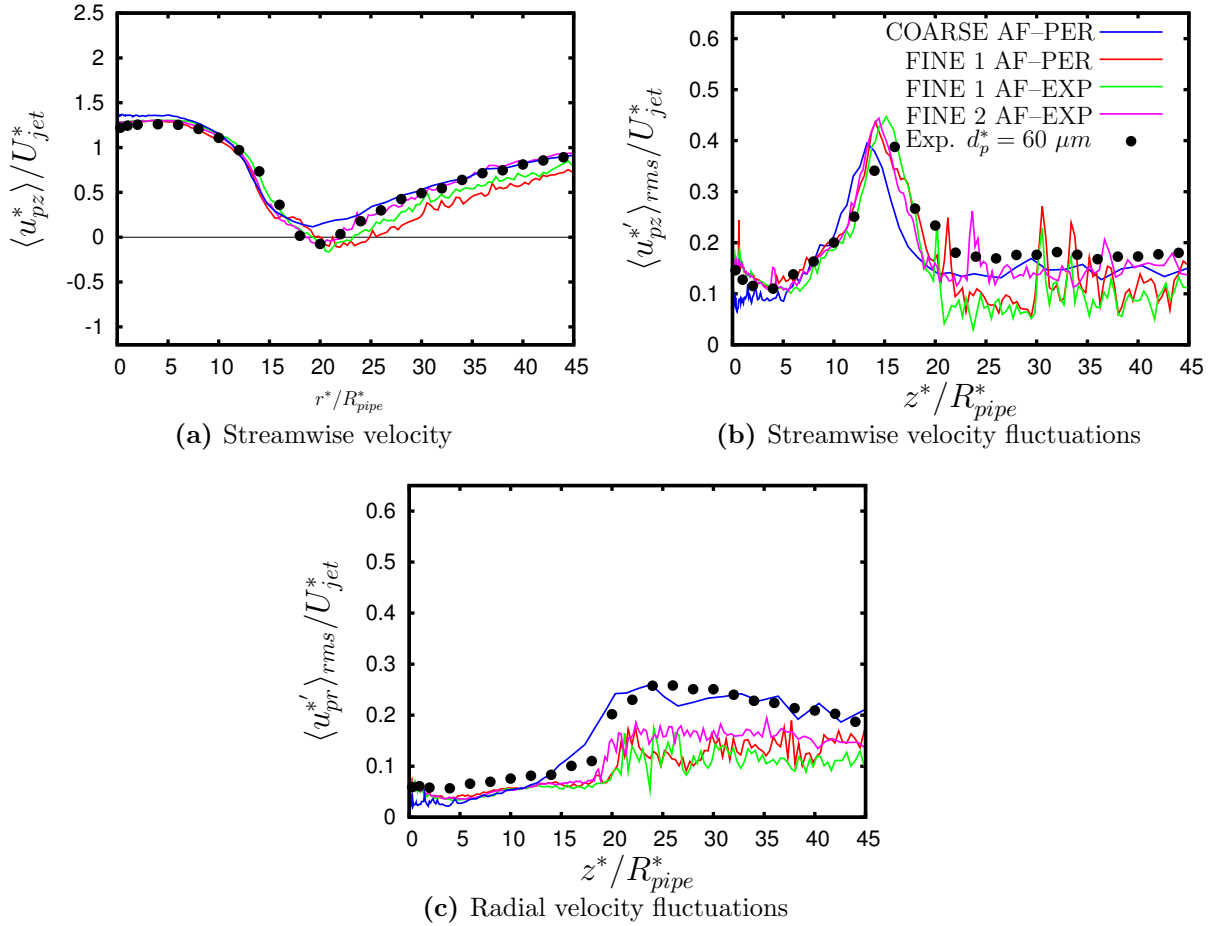


Figure 110: Influence of the resolution and the inflow conditions on the axial evolution of the streamwise velocity and the streamwise and radial velocity fluctuations of the particulate phase with a diameter of $d_p^* = 60 \mu\text{m}$ at $\eta = 22\%$; experimental data by Borée et al. (2001).

the axis for the $60 \mu\text{m}$ particles. Obviously, taking into account the wall roughness seen by the particles when generating the inflow conditions for the particles in the cases of the FINE 1 and FINE 2 grids, leads to increased particle velocity fluctuations at the entrance. Therefore, also a better agreement of this quantity near the entrance for the FINE 1 and FINE 2 grids compared with the simulations using the COARSE grid can be found.

As visible in Fig. 110(c) the wall roughness considered in the pipe flow leads also to increased particle velocity fluctuations in the radial direction close to the entrance. Unfortunately, the improved inflow conditions for the particles do not influence the downstream evolution of $\langle u_{pr}' \rangle_{rms} / U_{jet}^*$. Decisive for the downstream evolution of the radial particle velocity fluctuations is the evolution of the radial fluid velocity fluctuations: Since this quantity is underpredicted for the fluid in the region behind S1 for the FINE 1 and FINE 2 grids compared with the reference experiment, the same holds also for the particles.

Figure 111 shows the mean streamwise particle velocity at all measurement planes z^*/R_{pipe}^* . The same presentation as used for the mean fluid velocity (Fig. 106) is applied. It is evident that no big differences between the four cases analyzed here can be found in the region near the axis. Further away from the axis, however, the particles are moving faster in streamwise direction for the cases where the inflow of the annular flow is generated

by using the experimental data (cases FINE 1 AF-EXP and FINE 2 AF-EXP) than for the cases the FINE 1 AF-PER and COARSE AF-PER. The reason is again that the fluid in the former two cases moves faster in this region (see Fig. 106).

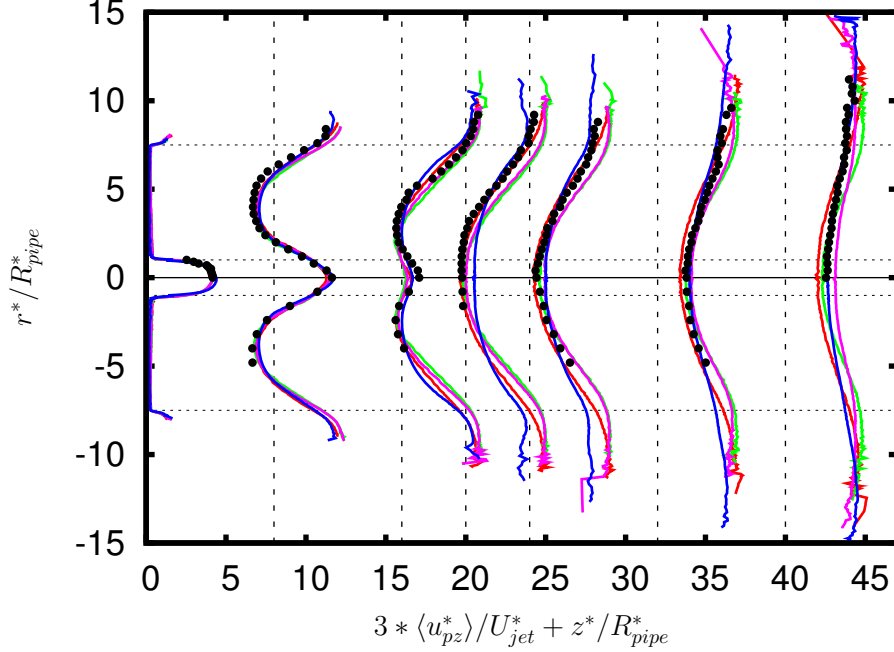


Figure 111: $\eta = 22\%$: Streamwise velocity of particles with a diameter of $d_p^* = 60 \mu\text{m}$ at the measurement planes $z^*/R_{pipe}^* = 0.3, 8, 16, 20, 24, 32$ and 40 . Blue line: COARSE AF-PER, red line: FINE 1 AF-PER, green line: FINE 1 AF-EXP, magenta line: FINE 2 AF-EXP, filled symbols: Exp. two-phase (Borée et al., 2001).

Figure 112 shows the mean radial particle velocity $\langle u_{pr}^* \rangle / U_{jet}^*$ at all measurement planes z^*/R_{pipe}^* . Remarkable is that the agreement with the experiment is improved for the three simulations using the fine grids in the region away from the axis at the measurement planes located at $z^*/R_{pipe}^* = 16, 20, 24$ and 32 . In the region $5 \leq r^*/R_{pipe}^* \leq 7.5$ the simulation using the coarse grid predicts only a very small negative radial particle velocity in the aforementioned measurement planes. Contrarily, the experiments and the simulations using the fine grids show a larger region with negative values of $\langle u_{pr}^* \rangle / U_{jet}^*$.

Figure 113 shows the streamwise particle velocity fluctuations $\langle u_{pz}^{*'} \rangle_{rms} / U_{jet}^*$ at all measurement planes z^*/R_{pipe}^* . Noteworthy is that the agreement of this statistical quantity with the experiment of Borée et al. (2001) is significantly improved at the plane located at $z^*/R_{pipe}^* = 0.3$ for the simulations based on the FINE grids (the red, green and magenta line in Fig. 113) compared with the simulation using the COARSE grid (blue line). The inflow conditions for the particles for the first three calculations mentioned are generated taking into account the rebounding behavior of the solid particles at rough pipe walls. For the COARSE AF-PER case the inflow conditions for the particles are obtained by a four-way coupled pipe flow simulation assuming a smooth wall seen by the particles. Noteworthy is also the effect of inertia which is observable in the streamwise velocity fluctuations: Since the rather heavy $60 \mu\text{m}$ particle cannot completely follow the continuous phase, they feel only the large turbulent scales. Therefore, the discrepancies between the COARSE AF-PER case and the FINE 1 AF-PER, FINE 1 AF-EXP and FINE 2 AF-EXP cases observed in the near-axis region of the streamwise fluid velocity fluctuations

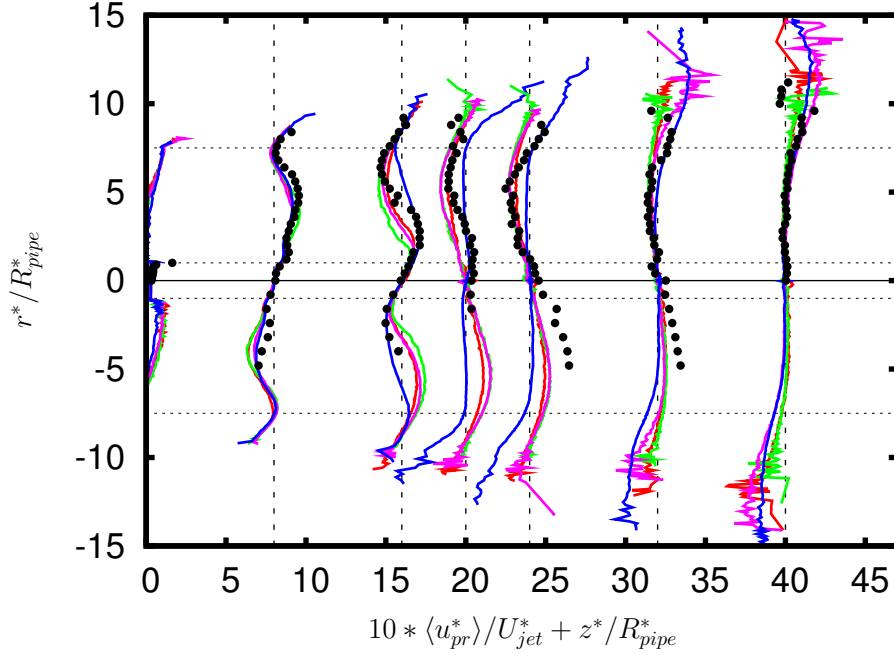


Figure 112: $\eta = 22\%$: Radial velocity of particles with a diameter of $d_p^* = 60 \mu\text{m}$ at the measurement planes $z^*/R_{pipe}^* = 0.3, 8, 16, 20, 24, 32$ and 40 . Blue line: COARSE AF-PER, red line: FINE 1 AF-PER, green line: FINE 1 AF-EXP, magenta line: FINE 2 AF-EXP, filled symbols: Exp. two-phase (Borée et al., 2001).

(see Fig. 108) are less pronounced for the particulate phase.

Figure 114 depicts the radial particle velocity fluctuations $\langle u_{pr}^* \rangle_{rms}/U_{jet}^*$ at all measurement planes z^*/R_{pipe}^* . For this statistical quantity similar considerations can be made as for the streamwise particle velocity fluctuations illustrated in Fig. 113: The agreement of the simulations considering the rough pipe wall with the experiment is better at the plane $z^*/R_{pipe}^* = 0.3$ than for the simulation considering only a smooth wall seen by the particles. Furthermore, the large discrepancies between the COARSE AF-PER case and the FINE cases observed in the near-axis region of the radial fluid velocity fluctuations (see Fig. 109) are less pronounced for the particulate phase.

8.7.2.3 Influence of the Resolution and the Inflow Boundary Conditions on the Fluid and Particle Statistics for $\eta = 110\%$

In the following only the influence of the resolution and the inflow conditions on the axial evolution of the streamwise velocity and the streamwise and radial velocity fluctuations for the continuous and disperse phase is shown. The reason is that the discrepancies observed between the four cases analyzed in the previous section found for the region away from the axis in case of $\eta = 22\%$ can also be observed for $\eta = 110\%$. Therefore, the discussion is not repeated here. Briefly summarized the differences observed between the COARSE AF-PER and the FINE 1 AF-PER, and FINE 2 AF-EXP cases (for the high mass loading the simulation FINE 1 AF-EXP was not performed) found in the measurement planes $z^*/R_{pipe}^* = 0.3, 8, 16, 20$ and 24 are the following: Only small differences between these three simulations can be observed for the mean streamwise and the mean radial fluid velocity. The fluid velocity fluctuations in streamwise and radial directions for the FINE 1 AF-PER and FINE 2 AF-EXP are lower in the region between

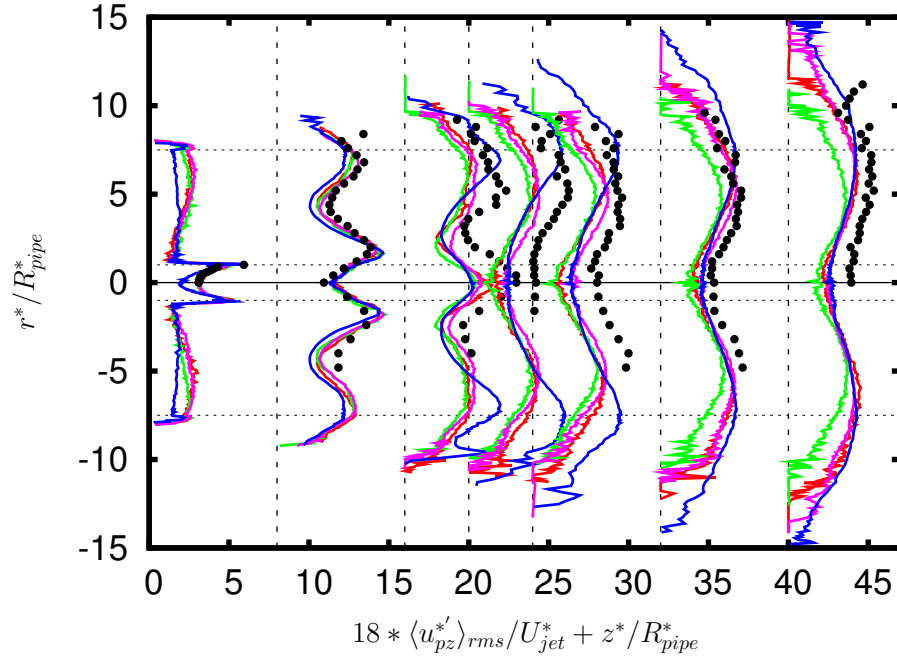


Figure 113: $\eta = 22\%$: Streamwise velocity fluctuations of particles with a diameter of $d_p^* = 60 \mu\text{m}$ at the measurement planes $z^*/R_{pipe}^* = 0.3, 8, 16, 20, 24, 32$ and 40 . Blue line: COARSE AF-PER, red line: FINE 1 AF-PER, green line: FINE 1 AF-EXP, magenta line: FINE 2 AF-EXP, filled symbols: Exp. two-phase (Borée et al., 2001).

the axis and the shear layer developing between the annular flow and the recirculation region R1 compared with the same quantities obtained for the COARSE AF-PER case. The discrepancies found between the COARSE AF-PER case and the FINE 1 AF-PER and FINE 2 AF-EXP cases regarding the particles are as follows: Only small differences between these three simulations can be observed for the mean streamwise particle velocity. Regarding the mean particle radial velocity the agreement with the experiment is better for the FINE 1 AF-PER and FINE 2 AF-EXP cases than for the COARSE AF-PER case. The velocity fluctuations in streamwise and radial directions for the FINE 1 AF-PER and FINE 2 AF-EXP cases are lower in the region between the axis and the shear layer developing between the annular flow and the recirculation region R1 compared with the same quantities obtained for the COARSE AF-PER case.

Continuous Phase

In this section the influence of the inflow conditions and the resolution on the fluid flow in the combustion chamber for the mass loading $\eta = 110\%$ is shown. As already mentioned, similar differences as for the lower mass loading are found between the COARSE AF-PER and the FINE 1 AF-PER and FINE 2 AF-EXP cases. Therefore, the axial evolution of the same quantities as before are taken as an example to illustrate the discrepancies between the different simulations.

Figure 115 shows the influence of the resolution and the inflow conditions on the axial evolution of the streamwise velocity and the streamwise and radial velocity fluctuations of the continuous phase at $\eta = 110\%$. The following observations can be made: The agreement between the mean fluid velocity in streamwise direction (Fig. 115(a)) and the

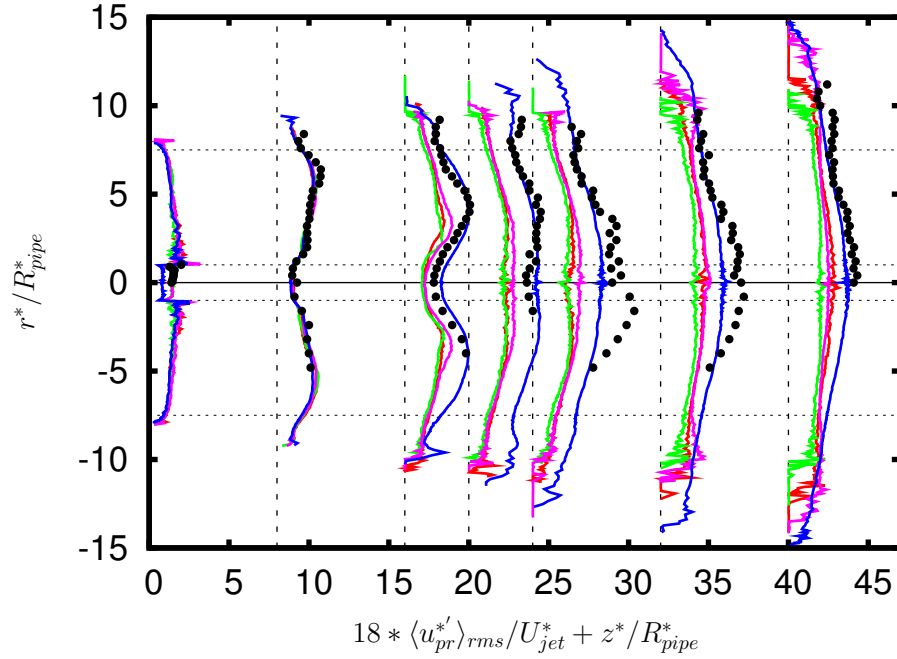


Figure 114: $\eta = 22\%$: Radial velocity fluctuations of particles with a diameter of $d_p^* = 60 \mu\text{m}$ at the measurement planes $z^*/R_{pipe}^* = 0.3, 8, 16, 20, 24, 32$ and 40 . Blue line: COARSE AF-PER, red line: FINE 1 AF-PER, green line: FINE 1 AF-EXP, magenta line: FINE 2 AF-EXP, filled symbols: Exp. two-phase (Borée et al., 2001).

experiment is improved near the pipe entrance for the FINE 1 AF-PER and FINE 2 AF-EXP cases because of the specific choice of the inflow conditions for the pipe flow (see § 7.7.2). Similar to the lower mass loading cases the minimum of the mean streamwise velocity is lower for the FINE 1 AF-PER and FINE 2 AF-EXP cases than for the COARSE AF-PER case. Analogies to the lower mass loading of $\eta = 22\%$ can also be found for the streamwise (Fig. 115(b)) and the radial velocity fluctuations (Fig. 115(c)) on the axis: The simulations denoted FINE 1 AF-PER and FINE 2 AF-EXP predict a larger maximum of the fluid streamwise velocity fluctuations than the simulation denoted COARSE AF-PER. Furthermore, the reduction of this statistical quantity behind the maximum is more pronounced for the FINE 1 AF-PER and FINE 2 AF-EXP cases than for the COARSE AF-PER case. The radial velocity fluctuations for the FINE 1 AF-PER and FINE 2 AF-EXP cases show a local maximum around $z^*/R_{pipe}^* \approx 15$ and the values of $\langle u_z^{*'} \rangle_{rms}/U_{jet}^*$ behind this point are clearly below the experimental values. Contrarily, for the COARSE AF-PER case $\langle u_z^{*'} \rangle_{rms}/U_{jet}^*$ continuously increases until $z^*/R_{pipe}^* \approx 28$.

Particulate Phase ($d_p^* = 60 \mu\text{m}$) Phase

Figure 116 shows the influence of the resolution and the inflow conditions on the axial evolution of the streamwise velocity and the streamwise and radial velocity fluctuations of the particulate phase ($d_p^* = 60 \mu\text{m}$) at $\eta = 110\%$. It is evident that the predictions of streamwise particle velocity and the particle fluctuations near the entrances are improved for the FINE 1 AF-PER and FINE 2 AF-EXP cases compared with the COARSE AF-PER case. Similar to the fluid phase the following analogies can be detected between the particle statistics obtained for the $\eta = 22\%$ and for the $\eta = 110\%$ mass loading: The minimum

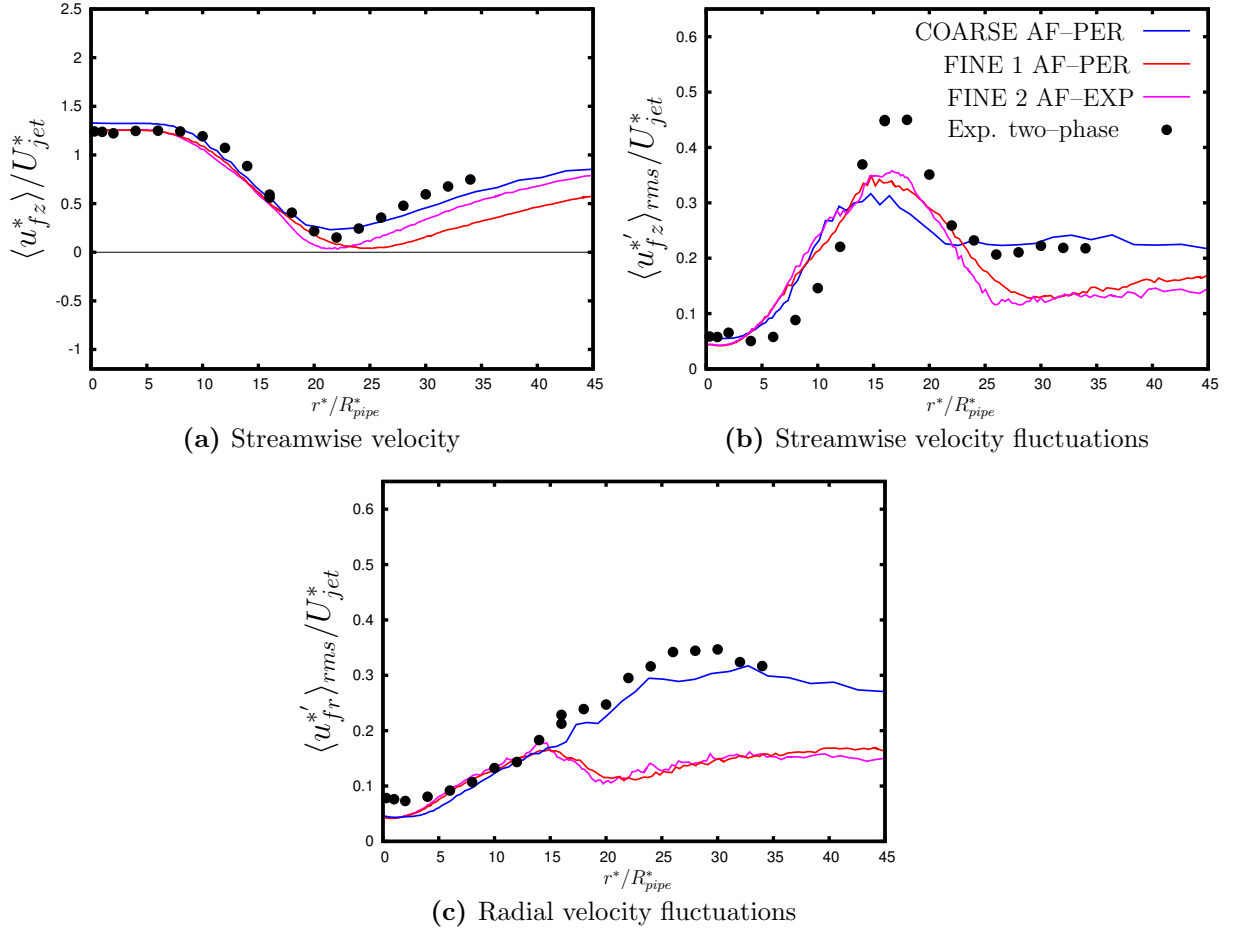


Figure 115: Influence of the resolution and the inflow conditions on the axial evolution of the streamwise velocity and the streamwise and radial velocity fluctuations of the continuous phase at $\eta = 110\%$; experimental data by Borée et al. (2001).

of the mean streamwise velocity is lower for the FINE 1 AF-PER and FINE 2 AF-EXP cases than for the COARSE AF-PER case. The simulation abbreviated by FINE 1 AF-PER and FINE 2 AF-EXP predict a larger maximum of the streamwise particle velocity fluctuations than the simulation abbreviated by COARSE AF-PER. Furthermore, the reduction of this statistical quantities behind the maximum is more pronounced for the FINE 1 AF-PER and FINE 2 AF-EXP cases than for the COARSE AF-PER case. The values of the radial particle velocity fluctuations for the FINE 1 AF-PER and FINE 2 AF-EXP cases are clearly below the experimental values behind $z^*/R_{pipe}^* \approx 15$. Contrarily, for the COARSE AF-PER case $\langle u_z^* \rangle_{rms} / U_{jet}^*$ continuously increases until $z^*/R_{pipe}^* \approx 30$.

8.7.3 Summary and Conclusions

The present study reports one of the first numerical predictions of the high mass loading case of the confined bluff-body particle-laden flow investigated experimentally by Borée et al. (2001) (see also Alletto and Breuer, 2012; Breuer and Alletto, 2012a,b). By tracking a huge number of individual poly-disperse particles through an eddy-resolved flow field predicted by LES, the collisions between particles of different sizes was simulated deterministically. Thus a four-way coupled methodology results. In order to evaluate the

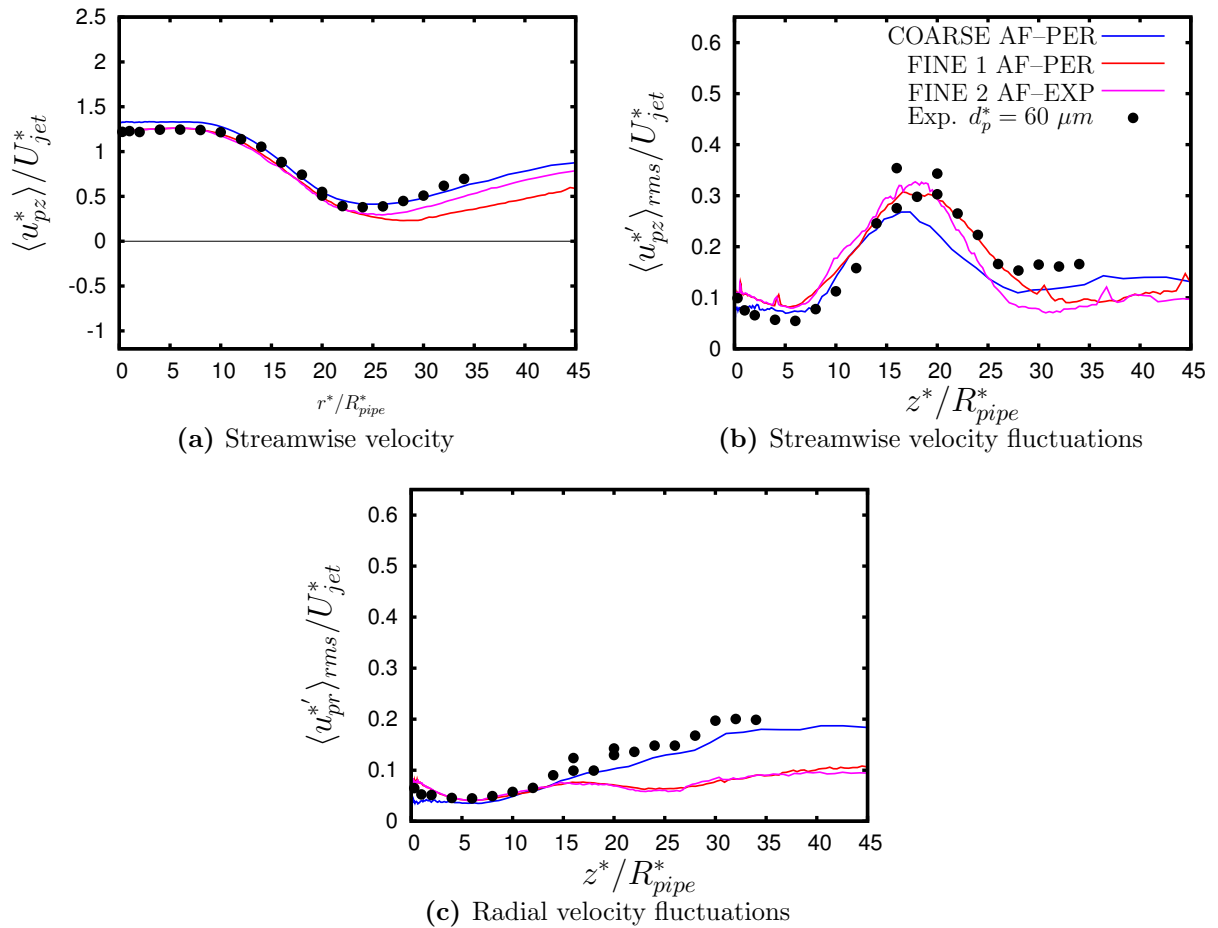


Figure 116: Influence of the resolution and the inflow conditions on the axial evolution of the streamwise velocity and the streamwise and radial velocity fluctuations of the particulate phase with a diameter of $d_p^* = 60 \mu\text{m}$ at $\eta = 110\%$; experimental data by Borée et al. (2001).

importance of the different coupling mechanisms, additional simulations restricting the coupling to two-way and one-way were carried out as well as predictions of the moderate mass loading case studied numerically before by several authors. Hence according to a suggestion already made by Borée et al. (2001) two-phase flow computations in which separate contributions can be artificially isolated are performed, which was impossible in their experimental investigations. Furthermore, the influence of the resolution and of the inflow boundary conditions are studied in detail. This improves the experience regarding LES of a cold combustion chamber flows. The following conclusions can be drawn:

- A significant difference exists between the moderate and the high mass loading case. Whereas without or with moderate mass loading two stagnation points are found on the axis of the chamber, these features completely disappear when the additional momentum induced by the particles is sufficiently high. Due to their high inertia, especially the large particles contribute to this modification of the continuous flow. The disappearance of the two stagnation points strongly influences the radial velocity fluctuations in the region close to the axis and thus the radial dispersion of the particles. For the moderate mass loading a local maximum of the radial velocity fluctuations is observed near the second stagnation point and thus

the particles are significantly dispersed in this region. Contrarily, this effect is not visible for the high mass loading since the stagnation points vanished by the induced particle momentum. Furthermore, the particles are found to accumulate between the two stagnation points for the moderate mass loading, whereas this phenomenon is not observed for the high mass loading.

- For $\eta = 22\%$ the interaction between the fluid and the particles is found to play a major role, whereas the effect of the inter-particle collisions is negligible as expected for this low mass loading. However, even the fluid-particle interaction is restricted in this case to the region around the axis of the chamber. In agreement with the statement of Borée et al. (2001) an accurate prediction of this case can therefore only be achieved by considering two-way coupling.
- For $\eta = 110\%$ the significance of the interaction between fluid and particles is even more pronounced. The deviations observed between the results of the one-way and two-way coupling strongly increase and the region where the fluid flow is influenced by the particulate phase is more extended.
- Contrarily, the effect of the inter-particle collisions is still minor for the high mass loading at the inlet. This observation can be explained by the fact that the local volume fraction of the jet entering the chamber is already below the often mentioned threshold of $\Phi = 10^{-3}$ at which as a widely accepted rule of thumb inter-particle collisions are assumed to be of importance. As shown above, due to missing stagnation points on the axis and strong dispersion of the particles the volume fraction decreases monotonically with increasing distance from the inlet. As estimated by Borée et al. (2001) collisions between particles are detected in the inner jet region of the chamber. The different classes of particles considered in the simulation leads to a mean drift between the size classes. This favors the occurrence of collisions. However, in contradiction to the educated guess by Borée et al. (2001) the collisions between particles are of minor importance also for the high mass loading case since the product of the collision frequency and the particle relaxation time $f_c^* \cdot \tau_p^*$ is found to be less than unity. In contrast to the experiment in the simulations it was possible to artificially isolate the different physical effects and thus to shed some light on the physical phenomena.
- The effect of the rough pipe walls on the particle motion has to be considered to correctly reproduce the inflow boundary conditions for the central jet. Considering the effect of the wall roughness on the particle motion in the pipe flow leads to a reduction of the mean particle velocity and to an increase of the particle velocity fluctuations. This measure yields a better agreement of the particle statistics with the reference experiment close to the entrance.
- A clear trend of the particle statistics on the axis depending on the particle diameter can be observed. Due to the effect of inertia larger particles are able to retain for a longer distance the initial velocity from the entrance. This leads to a downstream shift of the minimum velocity on the axis compared with smaller particles and hence to a maximum of the mean drift between small and big particles located at the end of R2. Furthermore, for particles with a larger Stokes number the minimum velocity on the axis is higher and the velocity fluctuations in the wake region are smaller compared to particles with a smaller Stokes number.

- Unfortunately, a strong grid dependence of the second-order fluid statistics and therewith associated also of the second-order particle statistics can be observed. In contrast to the expectatives the grid with a higher number of computational cells leads to a reduction of the fluid streamwise and radial velocity fluctuations near the axis. The influence of the resolution on the mean streamwise and radial fluid velocity is predominantly reflected in the expansion of the recirculation region R1 (see Fig. 104) generated by the sudden cross-section expansion behind the inflow of the annular flow. For the finer grid R1 extends further downstream compared with the coarse grid.
- The influence of the inflow boundary conditions used for the annular flow is prevalently noticeable in the downstream expansion of R1. Imposing the mean profile measured by the experiment of Borée et al. (2001) superimposed by the velocity fluctuations adjusted to the experiment, leads to a reduction of R1 compared to the simulation for which the inflow of the annular flow is generated with the help of predictions using periodic boundary conditions.

8.8 Cyclone Separator Flow

In the following the unladen and the particle-laden flow in the cyclone separator flow configuration experimentally investigated by Obermair (2002) (see also Obermair et al., 2003, 2005) is studied by means of LES. This section is organized as follows: First in § 8.8.1.1 the influence of the resolution and the subgrid-scale modeling for the continuous fluid is evaluated based on the reference data of the unladen flow. After that, the overall flow structure of the unladen flow for the simulations which show the best agreement with the experimental data is discussed in § 8.8.1.2. Finally, the influence of the one-way and the two-way coupling and also of the wall boundary condition for the particles is briefly evaluated in § 8.8.2.2. Note that parts of the results are already published in Alletto and Breuer (2014).

8.8.1 Unladen Flow

8.8.1.1 Influence of the Resolution and the Subgrid-scale Model for the Fluid

In order to provide a first overview of the influence of the grid resolution and the subgrid-scale model for the fluid, Figs. 117–119 depict the time-averaged streamwise and circumferential velocity of the fluid and the corresponding time-averaged velocity fluctuations at three different axial positions in the x - y plane normal to the cyclone axis. According to the representation of the axial position chosen in Figs. 120–125 these planes are located at $z^* = -197, 205$ and 602 mm. (see also Fig. 43(a)). Since the averaged flow is truly three-dimensional, an averaging in circumferential direction was not possible and only time-averaging could be applied. Note that the flow quantities displayed in Figs. 117–119 are made dimensionless with the mean velocity at the inflow U_{in}^* .

A clear trend of the time-averaged circumferential fluid velocity $\langle u_{f,\theta}^* \rangle / U_{in}^*$ along the axis depending on the resolution and the subgrid-scale model for the fluid can be observed (see Fig. 117(a), 118(a) and 119(a)). Comparing the three simulations carried out on the FINE grid, it is evident that increasing the eddy viscosity μ_T leads to a decrease of the time-averaged tangential velocity. For the two simulations using the model of Smagorinsky (1963) it is obvious that the computation with a higher value of C_s leads to a higher eddy viscosity since μ_T is proportional to C_s^2 (see § 3.2.1). For the model of Germano et al. (1991) where the constant C_s is dynamically adjusted, a direct estimation of μ_T is not possible. For that reason, the time-averaged values of the eddy viscosity $\langle \mu_T \rangle$ of the three simulations using the FINE grid are compared with each other. This comparison turns out that the highest values of $\langle \mu_T \rangle$ among the three simulations using the FINE grid is computed by the model of Germano et al. (1991). Consequently, that is consistent with the observation that increasing values of μ_T yield a decreasing level of the tangential velocity.

Regarding the time-averaged velocity in axial direction (Figs. 117(b), 118(b) and 119(b)), unfortunately, no such clear dependency on the subgrid-scale model for the fluid can be observed. However, it can be deduced that the W-shaped velocity profile is more pronounced for the computations applying the model of Smagorinsky (1963) than the model of Germano et al. (1991). Furthermore, the minimum axial velocity in the core region decreases with increasing values of $\langle \mu_T \rangle$. The comparison of this quantity with the reference experiments is provided later on.

The influence of μ_T on the prediction of the flow in a cyclone separator can also be observed in the second moments of the fluid velocity (Figs. 117(d)–(c), 118(d)–(c) and

119(d)–(c)). Regarding the three computations performed on the FINE grid the highest circumferential and axial velocity fluctuations in the core region are predicted by the simulation applying the model of Smagorinsky (1963) with a constant of $C_s = 0.1$ and the lowest are predicted using the model of Germano et al. (1991). This trend can be observed for both second-order statistics at all three axial positions analyzed except the axial velocity fluctuations at the plane located in the cone (see Fig. 117(d)).

Comparing the simulations performed on two different grids but with the same Smagorinsky constant C_s (red and magenta lines in Figs. 117–119), it is evident that the computation performed on the FINE grid predicts a higher time-averaged circumferential fluid velocity $\langle u_{f,\theta}^* \rangle / U_{in}^*$ and higher velocity fluctuations compared with the computation performed on the COARSE grid. Since for the model of Smagorinsky (1963) the eddy viscosity μ_T is proportional to the filter width squared Δ^2 , the predicted values of μ_T for the COARSE grid are higher than for the FINE grid. Therefore, the reduction of the circumferential velocity and of the velocity fluctuations in the core region for decreasing resolution is in line with the dependence of the predicted fluid flow on the subgrid-scale model, i.e., an increase of μ_T leads to a reduction of $\langle u_{f,\theta}^* \rangle / U_{in}^*$, $\langle u_{f,\theta}^* \rangle_{rms} / U_{in}^*$ and $\langle u_{f,z}^* \rangle_{rms} / U_{in}^*$. For the time-averaged axial velocity $\langle u_{f,z}^* \rangle / U_{in}^*$ unfortunately no clear dependency on the grid can be derived.

Regarding the comparison of the best present simulation (i.e., FINE grid, $C_s = 0.15$) with the experiments of Obermair et al. (2003) in the opinion of the author, a fairly well agreement is found in the major part of the cross-section except in the vortex core region (see Figs. 117–119). Comparing the simulated time-averaged circumferential velocity $\langle u_{f,\theta}^* \rangle / U_{in}^*$ with the reference experiment (see Fig. 117(a), 118(a) and 119(a)), it is evident that $\langle u_{f,\theta}^* \rangle / U_{in}^*$ is slightly underpredicted by all simulations in the region close to the wall. This indicates that the wall model of Werner and Wengle (1993) cannot adequately predict the wall shear stress. This is not surprising since the velocity profile assumed by Werner and Wengle (1993) used to compute the wall shear stress relies on the mean velocity profile of turbulent boundary layers with no or only weak positive streamwise pressure gradients. The assumption that the wall model of Werner and Wengle (1993) overpredicts the wall shear stress leading to a reduction of the circumferential velocity is further supported by an additional simulation on the COARSE grid, where the no-slip condition is applied (results are not shown for the sake of brevity). The time-averaged circumferential velocity for this simulation reached maximal values of $\langle u_{f,\theta}^* \rangle / U_{in}^* \approx 6$ in the core and values of $\langle u_{f,\theta}^* \rangle / U_{in}^* \approx 2$ near the wall at the same axial position as the results shown in Fig. 117. Hence, the application of the no-slip condition leads to an underprediction of the wall-shear stress compared to the model of Werner and Wengle (1993) and therefore to a doubling of $\langle u_{f,\theta}^* \rangle / U_{in}^*$. This indicates the great impact of the wall model on this quantity. Note that as already mentioned in § 7.8.2 on the COARSE grid also computations applying the wall model of Schumann (1975) were performed. Since similar results concerning the circumferential velocity as for the model of Werner and Wengle (1993) are achieved, this results adopting the wall model of Schumann (1975) are not shown for the sake of brevity.

Among the four statistical quantities shown in Figs. 117–119 the axial velocity $\langle u_{f,z}^* \rangle / U_{in}^*$ predicted by the simulations in the cyclone core region shows the greatest discrepancies with the experimental data of Obermair (2002). Especially in the conical part of the cyclone (see Fig. 117(b)), the experiment exhibits a positive axial velocity on the axis (i.e., the flow is directed towards the dust bin), while the simulations predict a negative

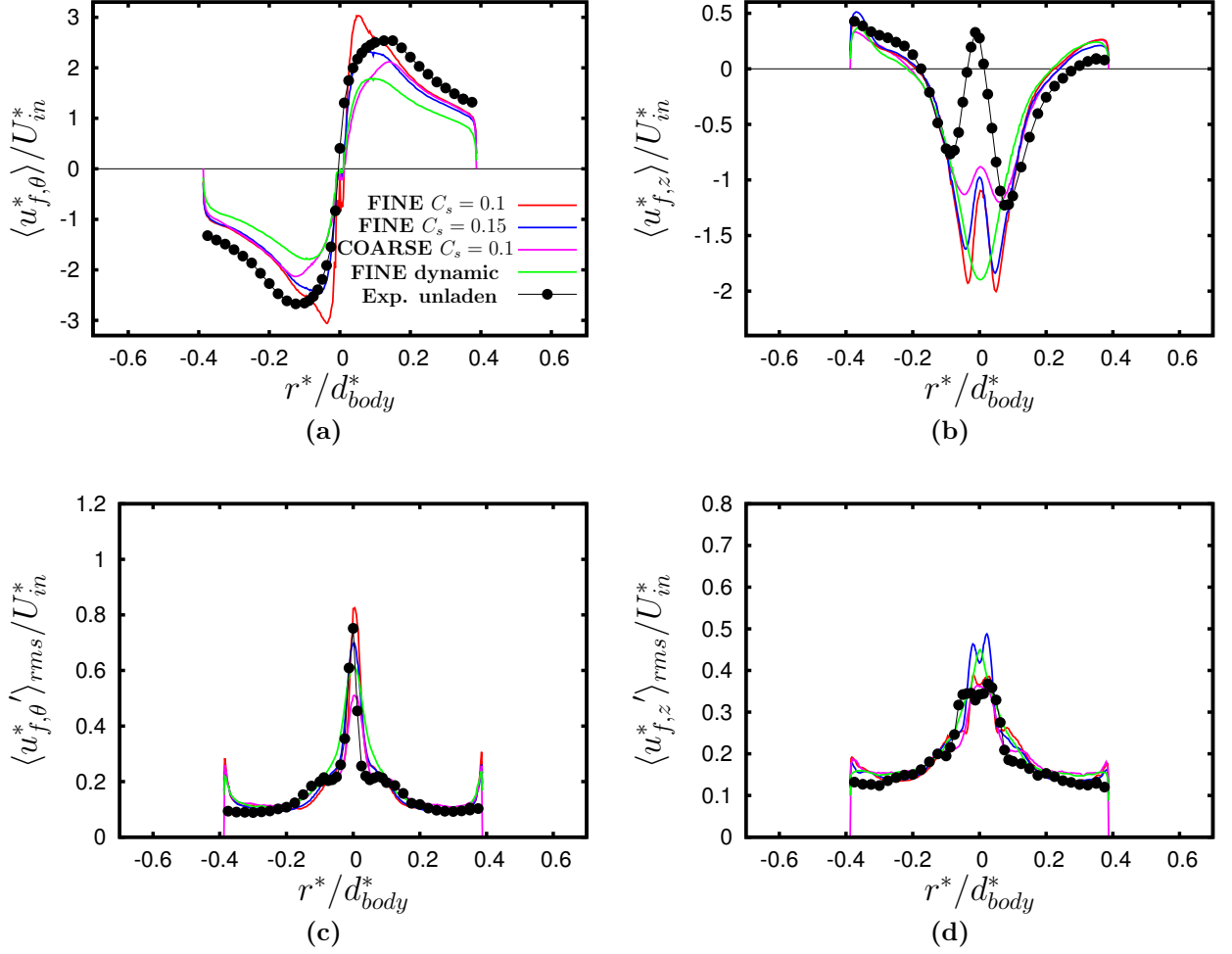


Figure 117: Influence of the resolution and the subgrid-scale modeling on the unladen flow statistics in the conical part of the cyclone at $z^* = -197$ mm: (a) time-averaged circumferential velocity, (b) time-averaged axial velocity, (c) time-averaged circumferential velocity fluctuations, (d) time-averaged axial velocity fluctuations. Experiments by Obermair (2002).

axial velocity (i.e, the flow is directed towards the outlet). Note, however, that the simulations COARSE $C_s = 0.1$, FINE $C_s = 0.1$ and FINE $C_s = 0.15$ predict in accordance to the experiment a W-shaped velocity profile. Unfortunately, no explanation for the discrepancies between simulation and experiment could be found. However, in the view of the still strong influence of the grid and of the subgrid-scale model for the fluid, probably the resolution was not sufficient to accurately reproduce the fluid axial velocity in the core region. The reason for the occurrence of the positive axial velocity in the core region observed in the experiment is still not clear. However, a positive axial velocity in the core region could be observed in different investigations, which experimentally studied the flow in a cyclone (Slack et al., 2000; Solero and Coghe, 2002) and by means of LES (Slack et al., 2000; Gronald and Derksen, 2011; Elsayed and Lacor, 2012). Note that none of the aforementioned investigations provided an explanation for the occurrence of the positive axial velocity in the core region.

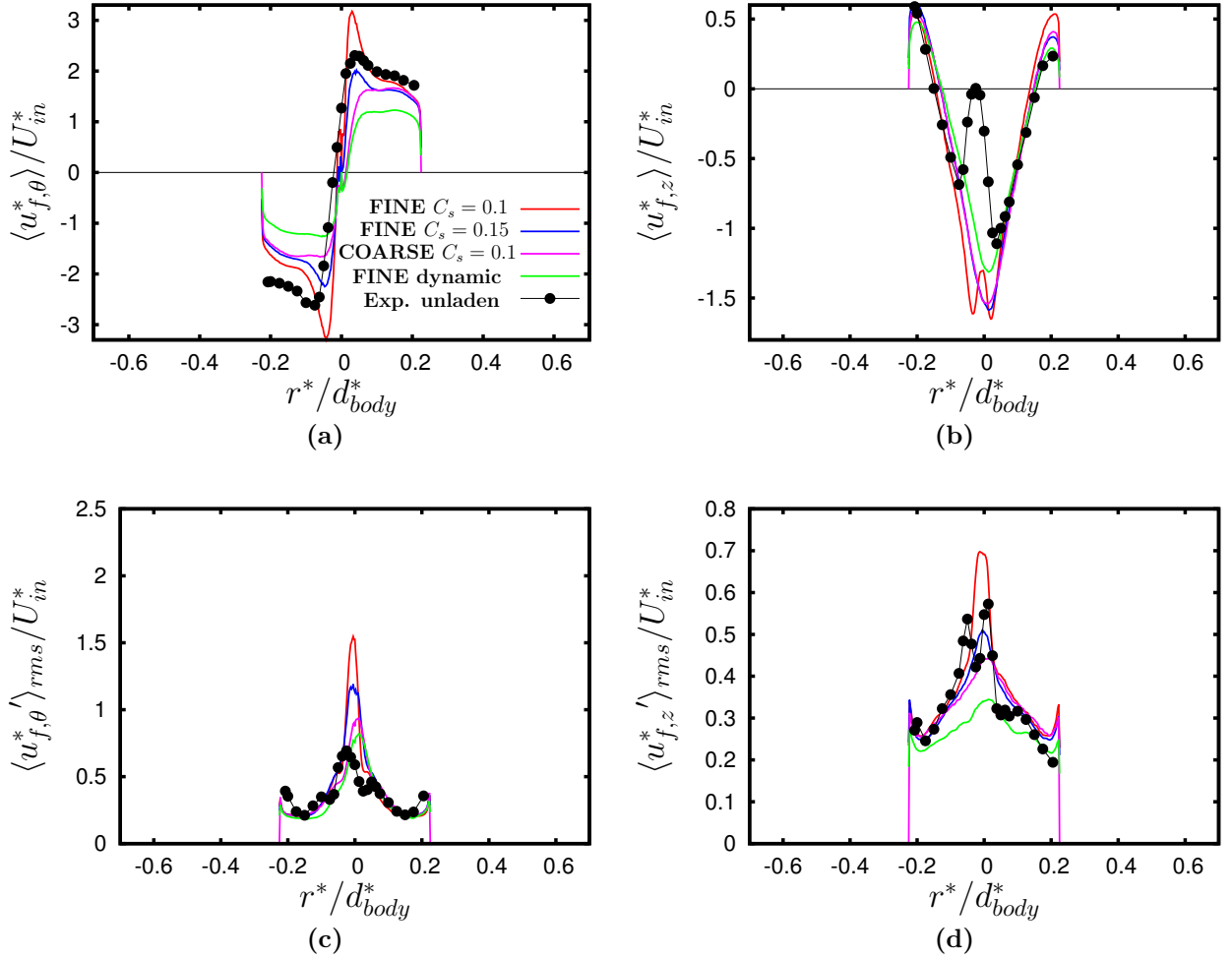


Figure 118: Influence of the resolution and the subgrid-scale modeling on the unladen flow statistics in the downcomer tube at $z^* = 205$ mm: **(a)** time-averaged circumferential velocity, **(b)** time-averaged axial velocity, **(c)** time-averaged circumferential velocity fluctuations, **(d)** time-averaged axial velocity fluctuations. Experiments by Obermair (2002).

8.8.1.2 Overall Flow Structure

After having studied the influence of the subgrid-scale modeling for the continuous fluid and the influence of the resolution on the flow in a cyclone separator, in this section the flow structure obtained by the simulations using the FINE grid and the model of Smagorinsky (1963) with a constant of $C_s = 0.15$ is compared qualitatively (but for the entire region of the cyclone investigated by Obermair, 2002) with the unladen flow experiment of Obermair (2002) and Obermair et al. (2003). In their measurements Obermair (2002) and Obermair et al. (2003) identified two main vortical structures: one is moving towards the dust bin along the cyclone wall and the other vortex is moving towards the outlet near the cyclone axis. Furthermore, a precessing vortex core is identified which rotates with a frequency of 66 Hz around the axis of the downcomer tube. The deviation from an axisymmetric configuration induced by the non-axisymmetric inlet leads to a spiral form of the vortex core underlining the variety of complicated flow structures found in cyclone separators. The aforementioned combination of resolution and subgrid-scale

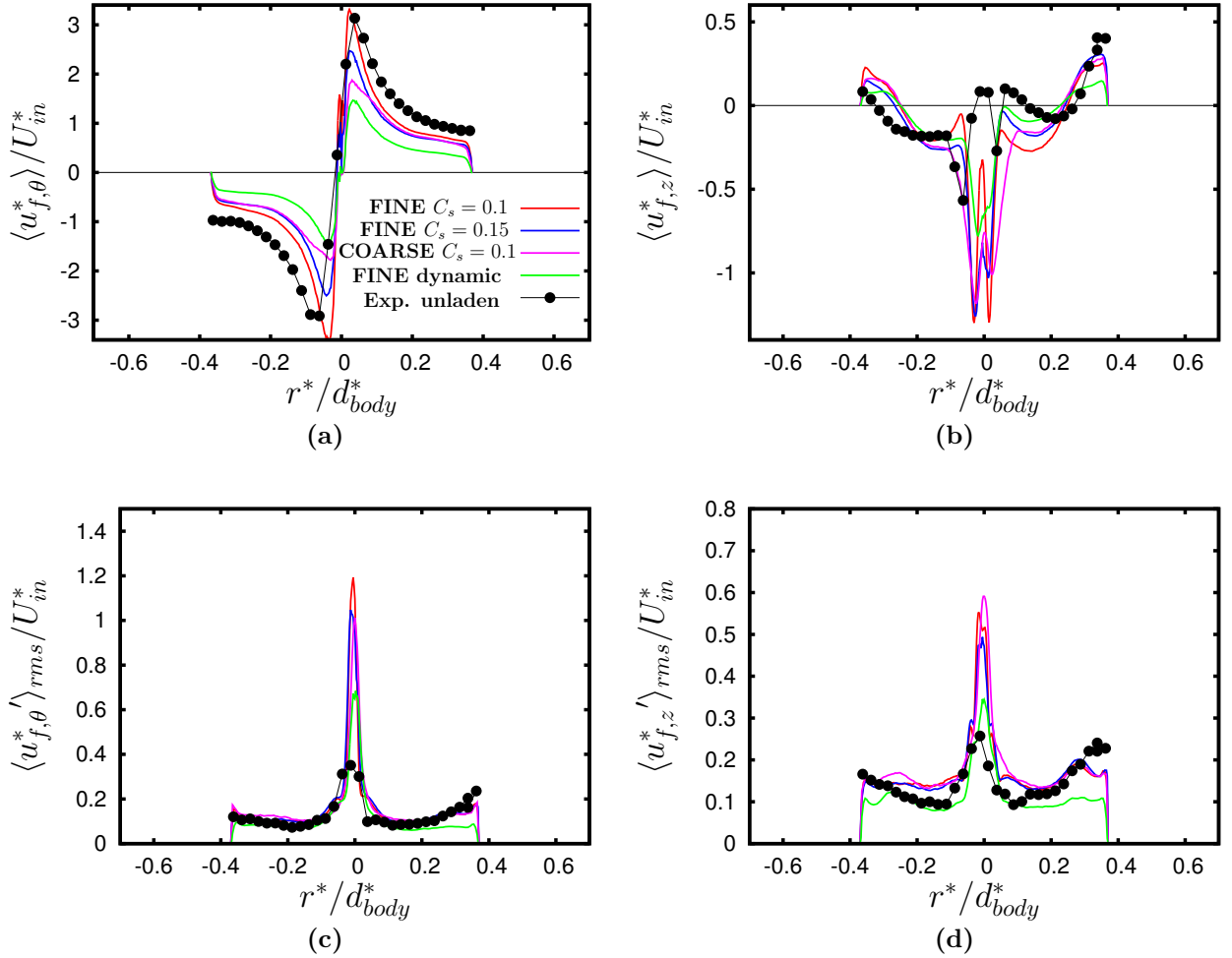


Figure 119: Influence of the resolution and the subgrid-scale modeling on the unladen flow statistics in the dust bin at $z^* = 602$ mm: (a) time-averaged circumferential velocity, (b) time-averaged axial velocity, (c) time-averaged circumferential velocity fluctuations, (d) time-averaged axial velocity fluctuations. Experiments by Obermair (2002).

model is chosen for the present analysis since it gives the best agreement with the reference experiment. Note that similar contour plots as shown in the following can also be found in Alletto and Breuer (2014). However, in this work the COARSE grid was used and the model of Schumann (1975) was applied.

Figure 120 depicts the contour plot of the time-averaged circumferential fluid velocity of the LES prediction (Fig. 120(a)) compared with the reference experiment (Fig. 120(b)). It is evident that the time-averaged circumferential fluid velocity of the LES prediction is qualitatively in good agreement with the unladen measurements of Obermair et al. (2003). Both investigations predict an off-axis alignment of the vortex core (the low velocity region near the cyclone axis). That means that the core of the vortex has a helical structure twisting down from the conical part towards the dust bin in form of a corkscrew. The magnitude of the circumferential velocity is slightly underpredicted and the deviation of the vortex core from the cyclone axis is not as pronounced as in the reference experiment. Note that such spirally formed mean vortex cores were also

found in other LES simulations (see Derksen (2003) and Gronald and Derksen (2011)) and also in other experiments (see the comment in Derksen (2003)). This indicates that the statistically averaged flow in a cyclone separator is truly three-dimensional due to the deviation of the present geometry from an axisymmetric geometry introduced by a finite number of inlets (Derksen, 2003). As already mentioned in the former section, the reason for the discrepancies between the flow statistics of the LES and the experiment is probably due to the overprediction of the wall shear stresses by the applied wall model.

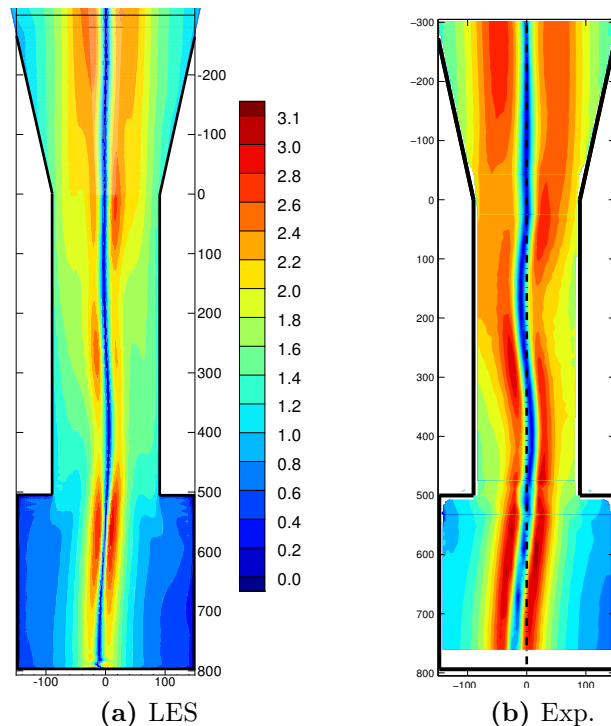


Figure 120: Time-averaged circumferential velocity $\langle u_{f,\theta}^* \rangle / U_{in}^*$ in the central x - z plane **(a)** LES prediction (FINE $C_s = 0.15$); **(b)** unladen flow experiment by Obermair et al. (2003) (same contour levels); Axial and radial coordinates given in [mm].

In order to visualize the core of the vortex in Fig. 121 a snapshot of the pressure isosurface is shown. It is evident that the isosurface has the form of a corkscrew where the turns have a small radius. This is consistent with the observation that the off-axis alignment of the zero mean circumferential velocity representing the mean vortex core is small.

By recording and subsequently visualizing the pressure isosurfaces in planes normal to the z -axis, it could be observed that the instantaneous center of the vortex precesses around its mean center. The sense of rotation of the vortex is given by the location of the inlet. Since in the present configuration the inlet is aligned with the x -axis, the fluid introduced in the cyclone barrel generates a vortex which rotates in mathematically negative sense around the z -axis (see Fig. 43). For this reason also the vortex core precesses in the same sense around the z -axis. In order to determine the frequency of the precessing vortex core, the pressure signal is recorded in the downcomer tube (see Fig. 122(a)). The pressure is recorded in this part of the cyclone in order to allow a comparison with the unladen flow data of Obermair (2002). He reported a frequency of the precessing vortex core of 66 Hz. Unfortunately, he did not visualize any data signal

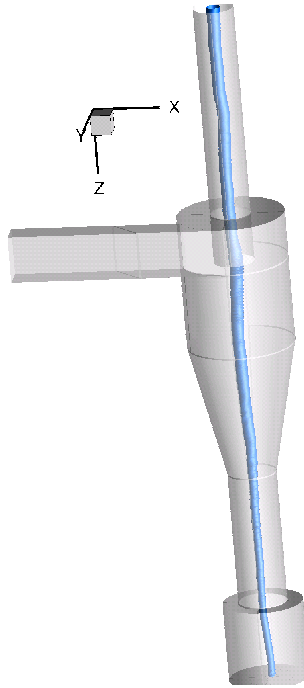


Figure 121: Snapshot of the pressure isosurface in the cyclone.

for the unladen case. From the record of the pressure signal shown in Fig. 122(a) it can be distinguished two main frequencies: A low frequency oscillation superimposed with a high frequency oscillation. In order to determine the frequency of this two modes, in Fig. 122(b) the discrete Fourier transformation (DFT) of the pressure signal is shown. Two main peaks can be distinguished: One is located at 16 Hz and the highest peak is located at 55 Hz. From this analysis it can be concluded that the vortex core in the simulation precesses slower around its mean center than the vortex core in the experiment. In the view of the differences found between simulation and experiment this is not surprising.

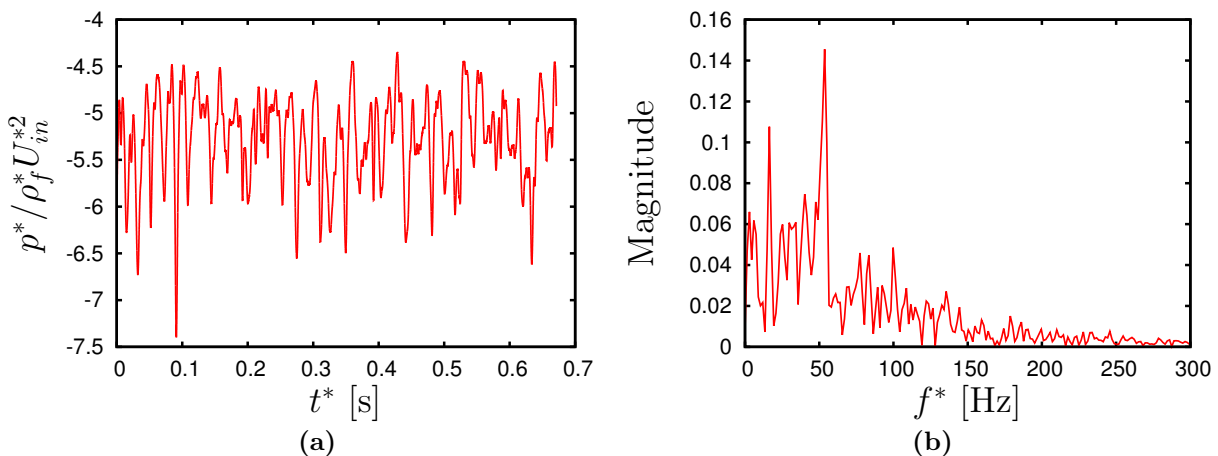


Figure 122: Analysis of the precessing vortex core in the unladen LES: (a) pressure signal recorded in the downcomer (b) DFT of the pressure signal

Figure 123 shows the contour plot of the time-averaged axial velocity of the continuous flow (Fig. 123(a)) compared with the unladen reference experiment of Obermair et al.

(2003) (Fig. 123(b)) in the central x - z plane. Positive velocities indicate that the flow is directed towards the dust bin and negative velocities denote that the fluid is transported towards the cyclone outlet. For this statistical quantity the LES prediction is qualitatively and quantitatively in good agreement with the reference experiment in the region close to the wall. Near the axis, however, the alternating zones of positive and negative axial velocity found in the experiment are not well captured by the simulation. Regardless this difference between the simulation and the experiment, it is evident that for both cases the flow is transported towards the dust bin near the wall and towards the outlet in the zone near the axis.

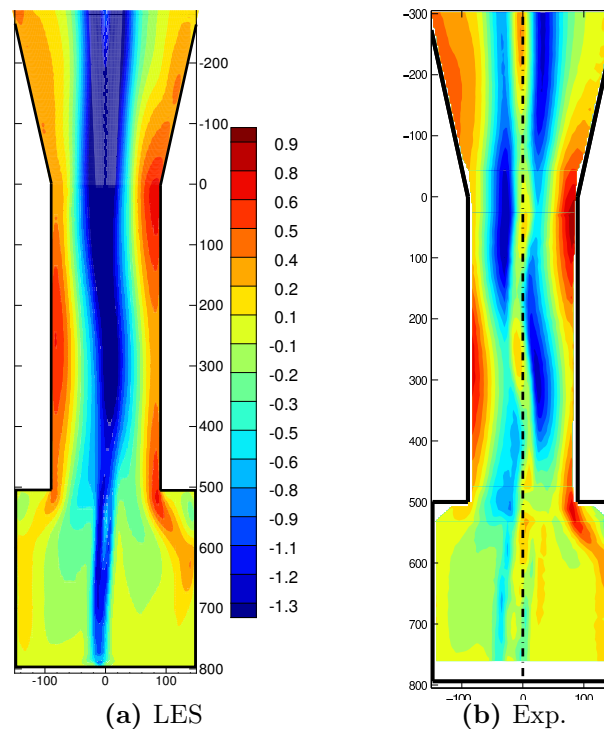


Figure 123: Time-averaged axial fluid velocity $\langle u_{f,z}^* \rangle / U_{in}^*$ in the central x - z plane (a) LES prediction (FINE $C_s = 0.15$); (b) unladen flow experiment by Obermair et al. (2003) (same contour levels); Axial and radial coordinates given in [mm].

The contour plot of the time-averaged RMS-values of the circumferential velocity fluctuations are depicted in Fig. 124 for the same plane as before. It is evident that the LES prediction of the fluid flow (Fig. 124(a)) is in qualitative agreement with the values measured by Obermair et al. (2003). For both cases the maximum fluctuations coincide with the location of the vortex core. However, the amplitudes of the simulated circumferential velocity fluctuations are overpredicted in the region near the axis. In the rest of the plane the agreement with the experiment is reasonable.

Figure 125 shows the contour plot of the RMS-values of the axial velocity fluctuations of the continuous flow. Also for this statistical moment the maximum of the fluctuations is observed near the vortex core in accordance with the measurements. The amplitude, however, is slightly underpredicted near the axis in the upper part of the downcomer tube and slightly overpredicted in the core region in the lower part of the downcomer tube compared with the measurements of Obermair et al. (2003). Regarding the other parts of the measurement plane good agreement is found with the experiment.

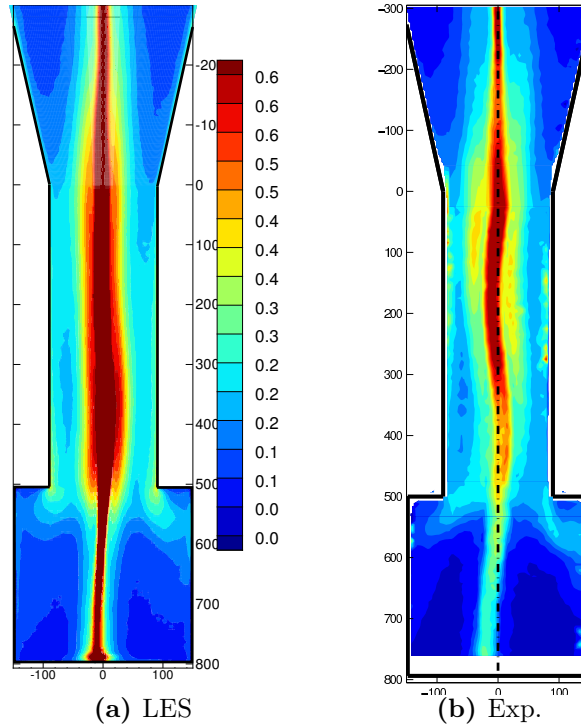


Figure 124: Time-averaged RMS-values of the circumferential fluid velocity fluctuations $\langle u_{f,\theta}^* \rangle_{rms} / U_{in}^*$ in the central x - z plane (a) LES prediction (FINE $C_s = 0.15$); (b) unladen flow experiment by Obermair et al. (2003) (same contour levels); Axial and radial coordinates given in [mm].

8.8.2 Particle-Laden Flow

8.8.2.1 Overall Flow Structure and Particle Diameter Distribution

Contrarily to the previous section, here the qualitative analysis of the two-phase flow is shown before the quantitative analysis. The goal is to first emphasize the drastic change in the results of the two-phase flow experiment of Obermair et al. (2005) compared with the unladen flow experiment of Obermair et al. (2003) (compare Figs. 126–129 with Figs. 120–125). Unfortunately, these drastic changes cannot be observed in the LES simulations. Note that the two-phase flow (particle-laden) data of Obermair (2002) shown in Figs. 120–125 are obtained by a LDA (Laser-Doppler Anemometry) system in contrast to the data shown in Obermair et al. (2005) which are obtained by a PDA (Phase-Doppler Anemometry) system. In the present comparison the LDA data of the continuous fluid are preferred to the PDA data. The reason is that for the LDA measurements also the second moments of the circumferential and axial velocities are available.

Figure 126 compares the particle-laden time-averaged circumferential fluid velocity $\langle u_{f,\theta}^* \rangle / U_{in}^*$ in the downcomer tube measured by Obermair (2002) (Fig. 126(c)) with the corresponding LES data for the fluid (Fig. 126(a)) and the particles (Fig. 126(b)). Note that Obermair (2002) performed the particle-laden LDA measurements (and also the PDA measurements) only in the downcomer tube, i.e., the part of the geometry shown in Figs. 126–130. As already mentioned above, for the unladen flow experimental data are also available for other parts of the cyclone. Since Obermair (2002) obtained particle-laden measurements only in the downcomer tube, only the numerical results obtained in this section of the cyclone are visualized in Figs. 126–130. It is evident that in the

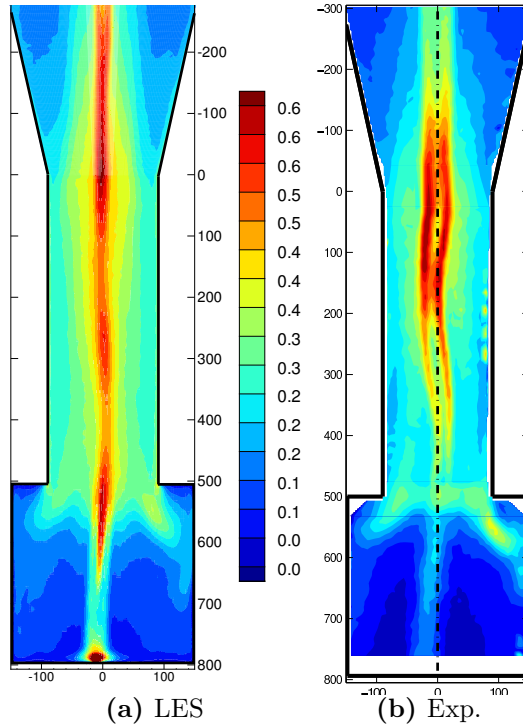


Figure 125: Time-averaged RMS-values of the axial fluid velocity fluctuations $\langle u_{f,z}^* \rangle_{rms}/U_{in}^*$ in the central x - z plane **(a)** LES prediction (FINE $C_s = 0.15$); **(b)** unladen flow experiment by Obermair et al. (2003) (same contour levels); Axial and radial coordinates given in [mm].

reference experiment a structure of the vortex experience a drastic change from the upper part, where it has the structure similar to a potential vortex to the bottom part of the downcomer tube, where it has a structure of a solid body rotation. Obermair (2002) supposed that the dynamics of the flow in the lower part of the downcomer tube is predominantly influenced by the decelerating effect of the particles located in the dust bin. He supposed that the particles slow down the fluid in the dust bin leading to the flow pattern shown in Fig. 126. However, in the view of the low mass loading used by Obermair (2002) and the distance between the change of the vortex structure and the dust bin his interpretation of the phenomenon is not completely satisfactory. A more plausible explanation for the drastic changes observed is that the vortex in the cyclone core of the unladen flow is near the stability limit between a continuous vortex reaching the bottom of the dust bin and a vortex where the end is bend towards the walls of the downcomer tube. Due to the injection of the particles small changes in the boundary conditions (e.g., a higher wall shear stress due to the particles deposited at the walls) or of the momentum required to keep moving the material in the dust bin lead to a sudden transition between the two vortex shapes described above. This conjecture is supported by two observations:

- (i) In the work of Bennek (2012), who used the same COARSE mesh as applied in this thesis, the vortex does not reach the bottom of the dust bin. Close to the end of the downcomer tube the vortex described in Bennek (2012) had a L-shape and the end rotated along the walls of the downcomer tube in a stable axial position. The first and second-order statistics of the fluid are in close agreement with the particle-

laden measurements shown in Figs. 126–129. In order to obtain a vortex which reaches the bottom of the dust bin on the COARSE grid, the solution obtained by Bennek (2012) had to be artificially pushed by a trick. This is achieved by coping the solution obtained in the upper half of the downcomer tube to the lower half of the downcomer tube. Then, the simulation is restarted from this flow field and the simulation is continued for a small period of time. After that, the coping procedure is repeated and the computation is restarted again. The reason for the repetition is that after only one coping procedure the flow in the dust bin was not able to acquire enough speed in order to produce the vortex topology reaching the bottom of the dust bin. Thus the method described above is carried out a few times until a stable vortex reaching the bottom of the dust bin develops. For the FINE grid, however, this measure has not to be undertaken since the vortex reaches the bottom of the dust bin already when starting from the initial conditions described in § 3.3.5. This observation supports the conjecture that the unladen flow of Obermair (2002) is near a stability limit.

- (ii) The second observation which supports the conjecture made above relies on the experimental work of Peng et al. (2005) and the LES of Pisarev et al. (2011). Both studied the ‘end of the vortex’ phenomenon in a swirl separators. In this device the flow structure is similar to the one observed in the downcomer tube: A vortex rotates in a straight tube. Furthermore, the flow in the center is directed towards the outlet and near the wall towards a dust bin. Both investigations reported a sudden change between a L-shaped vortex end which rotates along the circular walls and a straight vortex tube based on small changes in the boundary conditions. Peng et al. (2005) observed the aforementioned sudden change by increasing the inflow mass flow rate by only 5%. For the lower mass flow rate the L-shaped vortex and for the higher mass flow rate the straight vortex were observed. Pisarev et al. (2011) reported the transition from the two possible shapes of the vortex when decreasing the length of the dust bin. For a longer dust bin the L-shaped vortex end was predicted and for a shorter dust-bin length the straight vortex end was the stable vortex shape. These observations support the conjecture that only small changes of the boundary conditions or the operating conditions in a cyclone can cause the transition between two possible shapes of the vortex core.

Unfortunately, the present LES prediction cannot reproduce the drastic changes in the flow structure induced by the particles found by Obermair (2002). For the LES no substantial changes of the time-averaged circumferential fluid velocity between the one-way coupled (Fig. 120(a)) and the two-way coupled simulation with the rough wall boundary conditions for the particles can be observed (Fig. 126(a)). The reason is probably that the overall ratio of the total particle mass present in computational domain achieved by the parcel method to the total fluid mass present in the domain in the LES simulation is about 0.085%, i.e., similar to the mass loading of $\eta = 0.065\%$ present at the entrance. The mean total particle mass present in the domain of the LES simulation in the statistically steady state is the result of different processes. Visualizations have shown that a part of the particles injected in the computational domain are directly bypassed into the flow moving towards the outlet never being transported towards the dust bin. Another part of the particles are centrifuged towards the walls of the cyclone reaching the flow region which is directed towards the dust bin. Light particle are able to leave this flow region

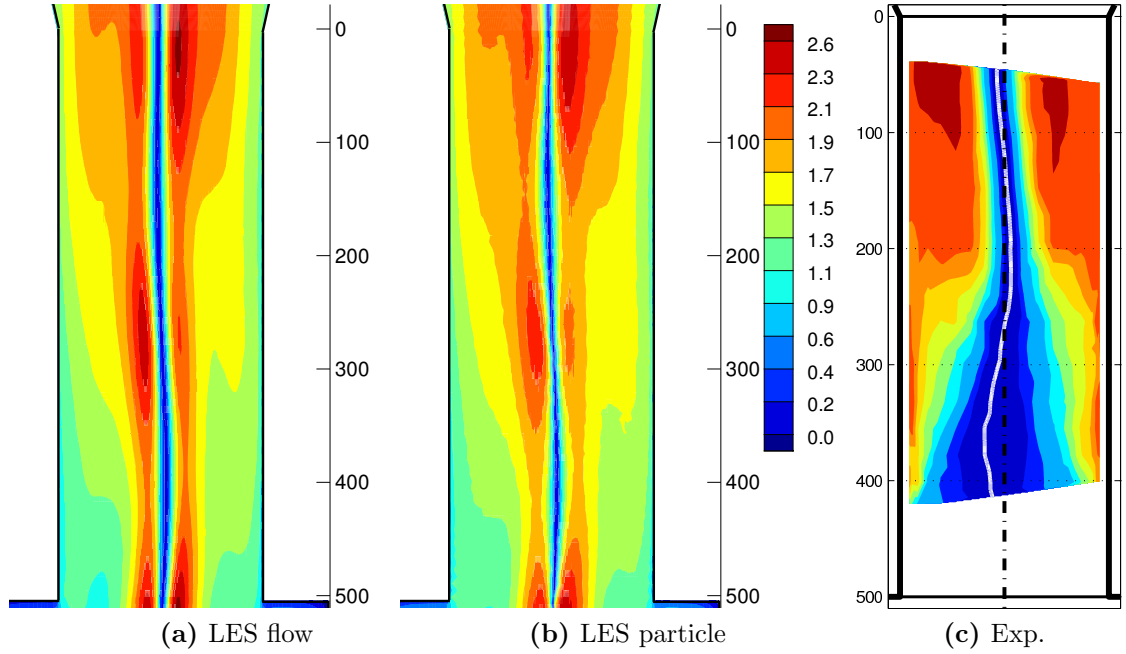


Figure 126: Time-averaged circumferential velocity $\langle u_{f,\theta}^* \rangle / U_{in}^*$ in the central x - z plane (a–b) LES prediction (FINE $C_s = 0.15$); (c) two-phase flow experiment by Obermair (2002) (same contour levels); Axial and radial coordinates given in [mm].

by the influence of the turbulent dispersion reaching also the flow directed towards the outlet. Heavy particles remain in the region close to the wall and are transported towards the dust bin where they are removed from the domain when they touch the walls of the dust bin. Therefore, in the simulation a statistically steady particle mass is reached when the particle mass injected is equal to the particle mass which leaves the domain from the outlet summed with the particle mass removed from the domain at the walls of the dust bin. The total mass of the particles present in the domain is a result of how the three aforementioned processes are related to each other. Say, e.g., that all particles are directly bypassed from the entrance into the gas stream moving towards the outlet. That means that no particle can be deposited and also that the total mass of particles present into the cyclone is very low since the residence time of the particle in the cyclone is also very low. The opposite scenario would be that all particles are centrifuged towards the walls moving towards the dust bin and no particle leaves the domain from the outlet. If the particle stream moving towards the dust bin is very slow and only a very small portion of the particles touch the walls of the dust bin being removed from the domain, this results in a long residence time of the particles inside the domain and therefore a large total particle mass present in the cyclone. Therefore, the total mass of the particles is strongly influenced by the interaction of the particles with turbulence and cannot be estimated a-priori.

In the experimental configuration similar considerations about the development of particle mass present inside the cyclone can be made but with the striking difference that it constantly increases. The reason is that in the experiment the particles are not removed artificially from the domain but remain trapped inside the dust bin. That means that for increasing operation duration of the cyclone the particle mass inside the cyclone constantly increases in the experiment. Unfortunately, Obermair (2002) do not provide any

hint of the mass of particles present inside the device.

For this low mass loading no noticeable difference between a one-way coupled and a two-way coupled simulation is expected. Note that for the aforementioned two figures the same scaling are used as in Obermair (2002) in order to emphasize the differences between the simulation and the experiment. One of the possible reasons why the present LES simulation cannot reproduce the observations made in the experiment can be that in the LES the particles are removed from the computational domain when they touch a wall of the dust bin. This measure is taken to achieve a statistically stationary state for the particles. (For a detailed explanation of the connection between the statistics and the removal of the particles, see § 7.8.2.) Furthermore, the removal of the particles from the dust bin avoids an accumulation of a huge number of particles in the computational domain which would lead to prohibitively large computational times. However, in the view of the big influence of the grid and also of the wall functions for the fluid, other reasons for the discrepancies between the simulation and the experiments in the particle-laden case are thinkable.

Regarding the difference between the particle and the fluid data (compare Fig. 126(a) with (Fig. 126(b)) it is evident that both computed statistics are very similar. Since the particles injected into the domain are very small, they are able to closely follow the carrier phase producing similar statistics as the fluid. This is in line with the findings of the former section, where only big particles are substantially influenced by the wall roughness, whereas small particles feel the wall roughness less since they quickly adjust to the carrier phase after a wall rebound.

Figures 127–129 compare the time-averaged axial fluid velocity $\langle u_{f,z}^* \rangle / U_{in}^*$, the time-averaged RMS-values of the circumferential fluid velocity fluctuations $\langle u_{f,\theta}^{*\prime} \rangle_{rms} / U_{in}^*$ and the time-averaged RMS-values of the axial fluid velocity fluctuations $\langle u_{f,z}^{*\prime} \rangle_{rms} / U_{in}^*$ of the LES predictions with the experiment of Obermair (2002). The following observations can be made: (i) The LES simulation can reproduce the experimental data in the upper part of the downcomer tube, while they fail to reproduce the experiment in the lower part of the downcomer tube. This is not surprising since the drastic changes observed in the measured circumferential velocity (see Fig. 126(c)) are reflected also on all other statistical quantities. (ii) The LES fluid and particle statistics are in close agreement because of the rather small particles present in the computational domain (see Table 6).

Figure 130 depicts the time-averaged particle diameter distribution normalized by the mean diameter $d_{p,in}^*$ at the inlet section. Also for this quantity big differences between the LES prediction (Fig. 130(a)) and the experiment (Fig. 130(b)) can be observed in the lower part of the downcomer tube. In the upper part the discrepancies are minor. Here both, experiment and simulation, show an increase of the time-averaged diameter from the cyclone axis towards the walls. This effect can be traced back to the influence of inertia on the particle motion. Larger particles, which are more subjected to the centrifugal forces, move towards the cyclone walls leading to an increase of the mean diameter in this region. Small particles, which are predominantly influenced by the turbulent motion, are more homogeneously distributed over the cross-section of the downcomer tube parallel to the axis. Therefore, only small particles are present in the core region leading to a reduction of the mean diameter compared to the wall region. In the LES predictions (Fig. 130(a)) the qualitative picture of the time-averaged diameter described before can be observed over the whole cross-section parallel to the axis. The reason is that the magnitude of the circumferential velocity does not change throughout the downcomer

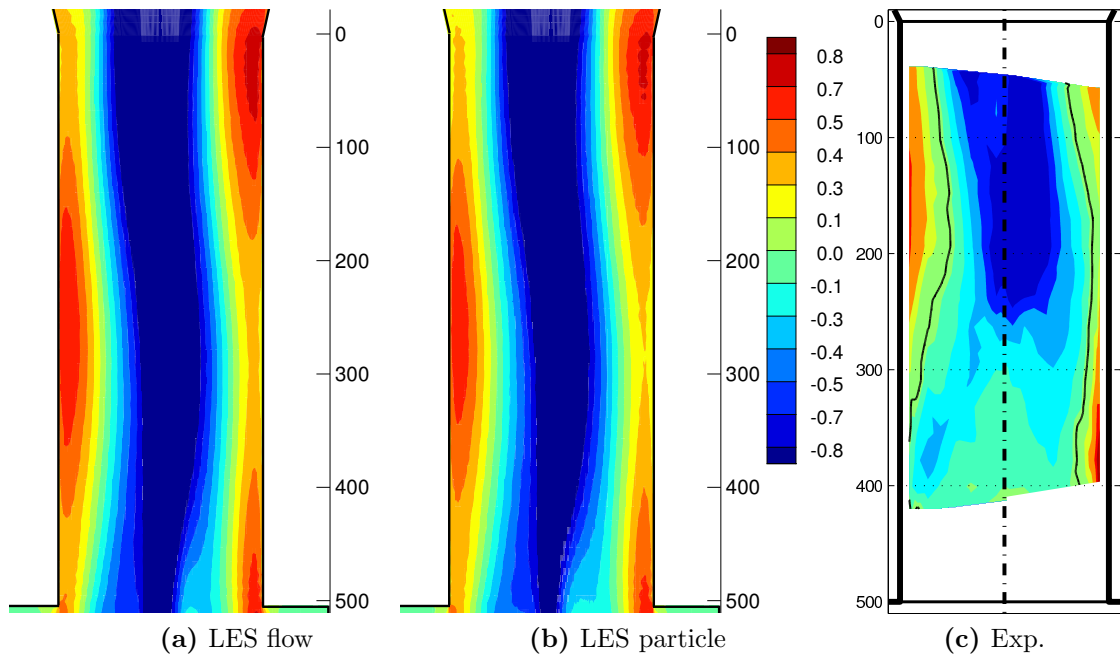


Figure 127: Time-averaged axial fluid velocity $\langle u_{f,z}^* \rangle / U_{in}^*$ in the central x - z plane (a–b) LES prediction (FINE $C_s = 0.15$); (c) two-phase flow experiment by Obermair (2002) (same contour levels); Axial and radial coordinates given in [mm].

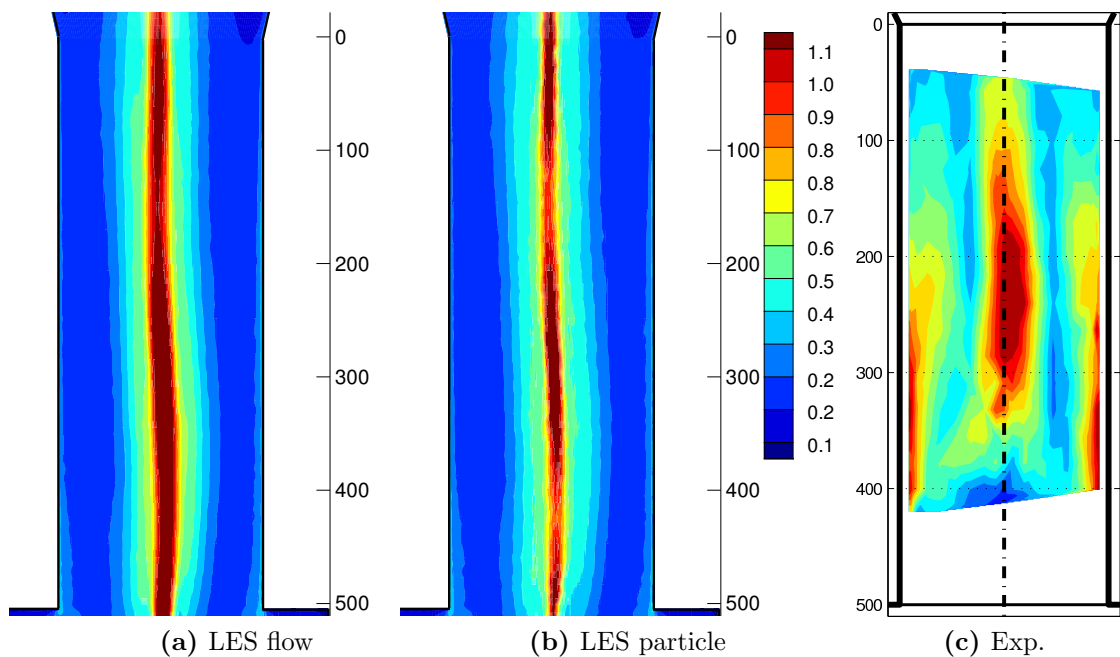


Figure 128: Time-averaged RMS-values of the circumferential fluid velocity fluctuations $\langle u_{f,\theta}^{*'} \rangle_{rms} / U_{in}^*$ in the central x - z plane (a–b) LES prediction (FINE $C_s = 0.15$); (c) two-phase flow experiment by Obermair (2002) (same contour levels); Axial and radial coordinates given in [mm].

tube (see Fig. 126(a)). The magnitude of $\langle d_p^* \rangle / d_{p,in}^*$, however, increases towards the dust bin, indicating that the bigger particles remain trapped in the dust bin. Regarding the

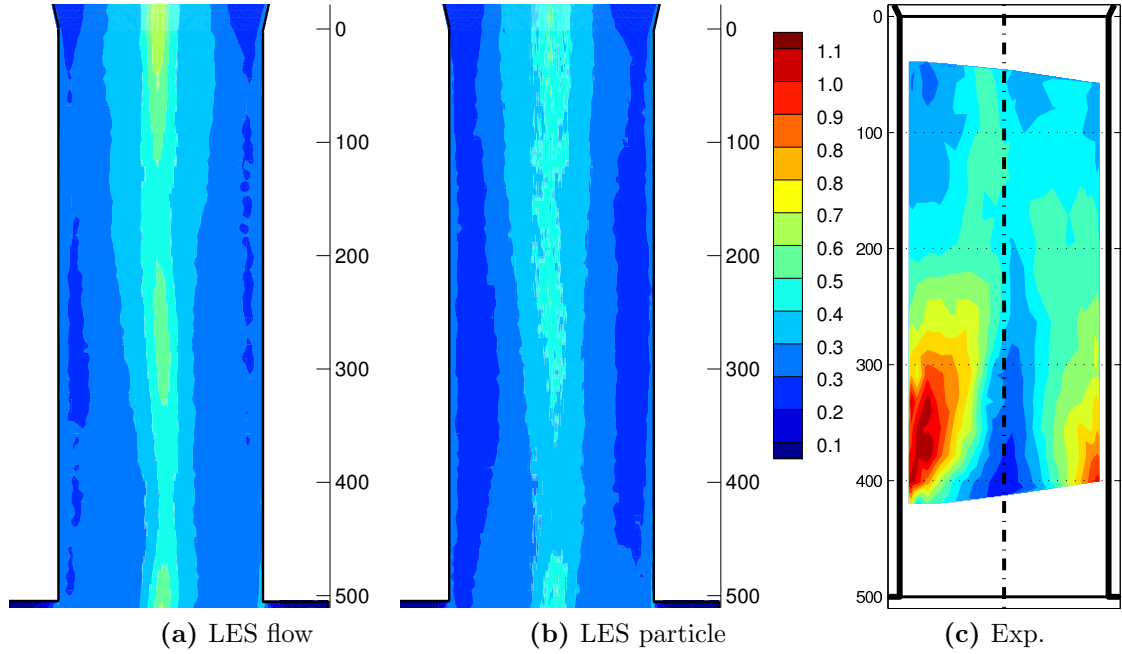


Figure 129: Time-averaged RMS-values of the axial fluid velocity fluctuations $\langle u_{f,z}^{*'} \rangle_{rms} / U_{in}^*$ in the central x - z plane (a–b) LES prediction (FINE $C_s = 0.15$); (c) two-phase flow experiment by Obermair (2002) (same contour levels); Axial and radial coordinates given in [mm].

experimental data (Fig. 130(b)), in the lower part of the downcomer tube the averaged diameter $\langle d_p^* \rangle / d_{p,in}^*$ does not change substantially in radial direction. This observation can be traced back to the small magnitude of the circumferential velocity observed in the lower part of the downcomer tube (see Fig. 126(c)). Furthermore, in the experimental data a strong increase of the mean particle diameter in the lower part of the cross-section visualized in Fig. 130(b) can be observed. Obermair (2002) claimed that this observation is a clear evidence of the occurrence of particle agglomeration. Note, however, that the different vortex structures found in the two-phase experiment compared to the single-phase experiment also strongly influences the diameter distribution of the particles.

8.8.2.2 Influence of the One-way and the Two-way Coupling and the Boundary Conditions for the Particles

In this section the particle statistics for the three different setups employed, i.e., a one-way and two-way coupled simulation with smooth walls seen by the particles and a two-way coupled simulation with rough walls for the particles are compared to each other. For comparison in Figs. 131–133 also the unladen and the two-phase flow data of Obermair (2002) are shown. The axial positions, where the statistical moments of the simulations are compared with each other, are depicted in Fig. 43(a) by the blue lines. According to the representation of the axial position chosen in Figs. 126–130 these planes are located at $z^* = 57, 217$ and 401 mm. (see also Fig. 43(a)). Note that a detailed discussion of Figs. 131–133 is omitted for the sake of brevity since the main scope of this section is to emphasize the small differences found between three different two-phase simulations shown here.

From Figs. 131–133 the following observations can be made: (i) The differences be-

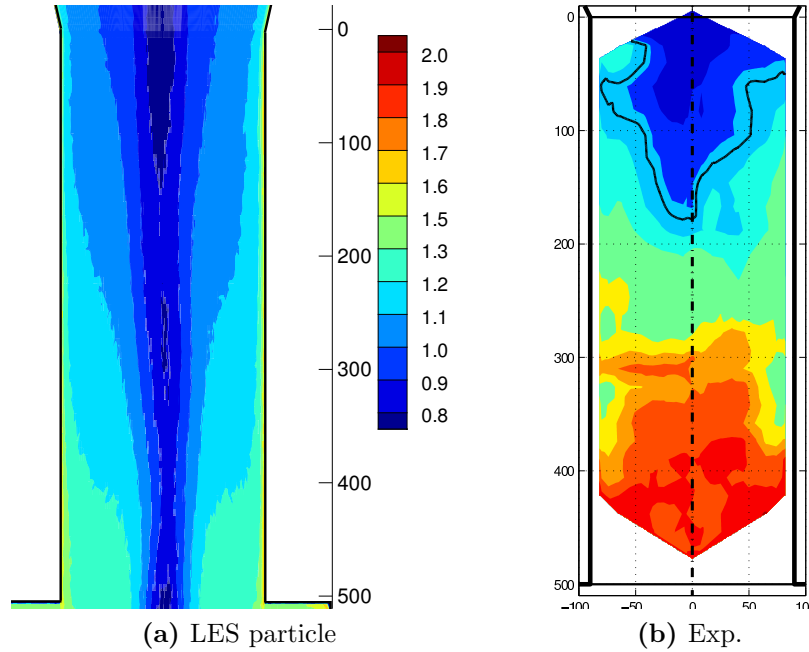


Figure 130: Time-averaged particle diameter distribution $\langle d_p^* \rangle / d_{p,in}^*$ in the central x - z plane (a–b) LES prediction (FINE $C_s = 0.15$); (c) two-phase flow experiment Obermair (2002) (same contour levels); Axial and radial coordinates given in [mm].

tween the experiments and the simulations observed in the former section are recovered in Figs.131–133. (ii) Very small differences between the particle statistics computed by means of one-way and two-way coupled simulations with smooth walls and a two-way coupled simulation with rough walls for the particles can be found. (iii) The not completely smooth particle statistics (especially the peaks in the mean circumferential velocity) in the core region of the cyclone can be explained by the low number of particles available in the core region used for the computation of the statistics. Analyzing the instantaneous particles data turned out that most particles are centrifuged out of the cyclone core leading to an almost particle-free region near the axis. Therefore only a small number of particles are available in the core region to calculate the particle statistics leading to not completely converged statistics in these region.

The vanishing differences between one-way and the two-way coupled simulation can be explained with the overall small ratio of particle mass to fluid mass of about 0.085% found in the computational domain. For this mass loading the forces exerted by the particles on the fluid are not large enough to substantially influence the flow.

Unfortunately, Obermair (2002) provided only the mass loading at the inlet and did not specify the overall total mass of particles present in the cyclone. Since in the experiment the particles are not removed from the device (as done artificially in the simulation), the overall total particle mass in the experimentally analyzed cyclone is for sure higher than the overall mass loading obtained in the simulation. (Keep in mind that, e.g., a vacuum cleaner whose working principle relies on a cyclone has also to be emptied from time to time.) Therefore, the influence of the particles in the reference experiment is higher than in the simulation. This could at least partially explain why the experiment exhibits in the two-phase flow configuration such a drastic change of the flow structure which cannot be observed in the simulation. A further difference between the simulation and the experiment is underlined by the photographs added in the appendix of Obermair

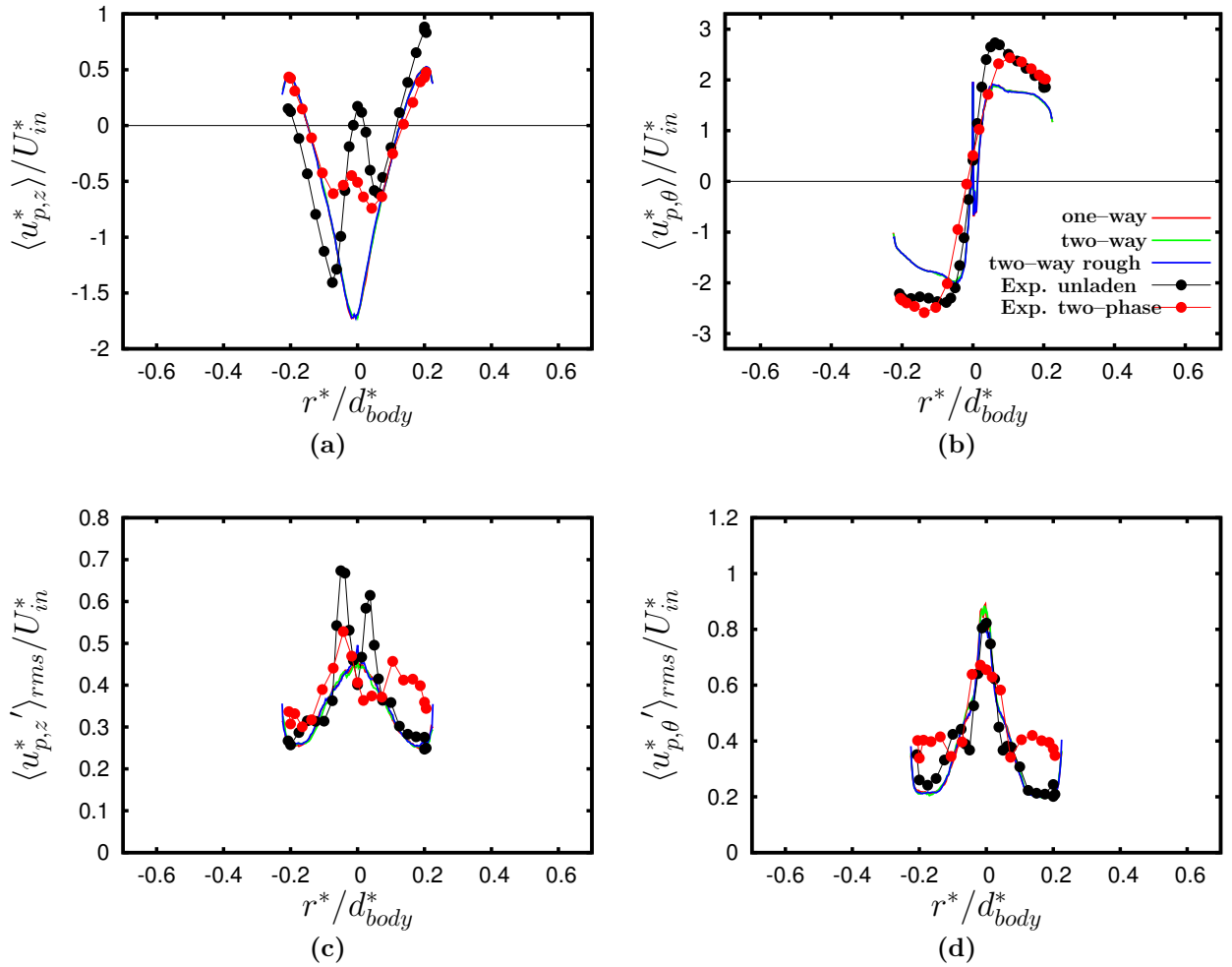


Figure 131: Upper part of the downcomer tube at $z^* = 57$ mm: Influence of the coupling and the wall roughness model for the particles on the particle statistics: (a) time-averaged axial velocity, (b) time-averaged circumferential velocity, (c) time-averaged axial velocity fluctuations, (d) time-averaged circumferential velocity fluctuations. Experiments by Obermair (2002).

(2002). These photographs show a large number of particles deposited at the cyclone walls. These deposited particles lead to a higher wall roughness in the two-phase case and therefore also to a higher wall-shear stress. This higher wall-shear stress can possibly influence the flow behavior in the two-phase experiment. Of course, the influence of the the enlargement of the wall roughness by the deposited particles on the fluid cannot be captured by the present implementation of the wall model for the fluid. However, as already mentioned above, in the view of the big influence of the grid and also of the wall functions for the fluid, other reasons for the discrepancies between the simulation and the experiments in the particle-laden case are thinkable.

The observation of a marginal difference between the particle statistics computed with a smooth wall boundary condition and a rough wall boundary condition for the particles is in line with the findings of the former section: Although small particles are stronger influenced by the wall roughness when they rebound at the wall, the small inertia leads to a quick re-adjustment to the carrier phase. Therefore, the dynamics are substantially influ-

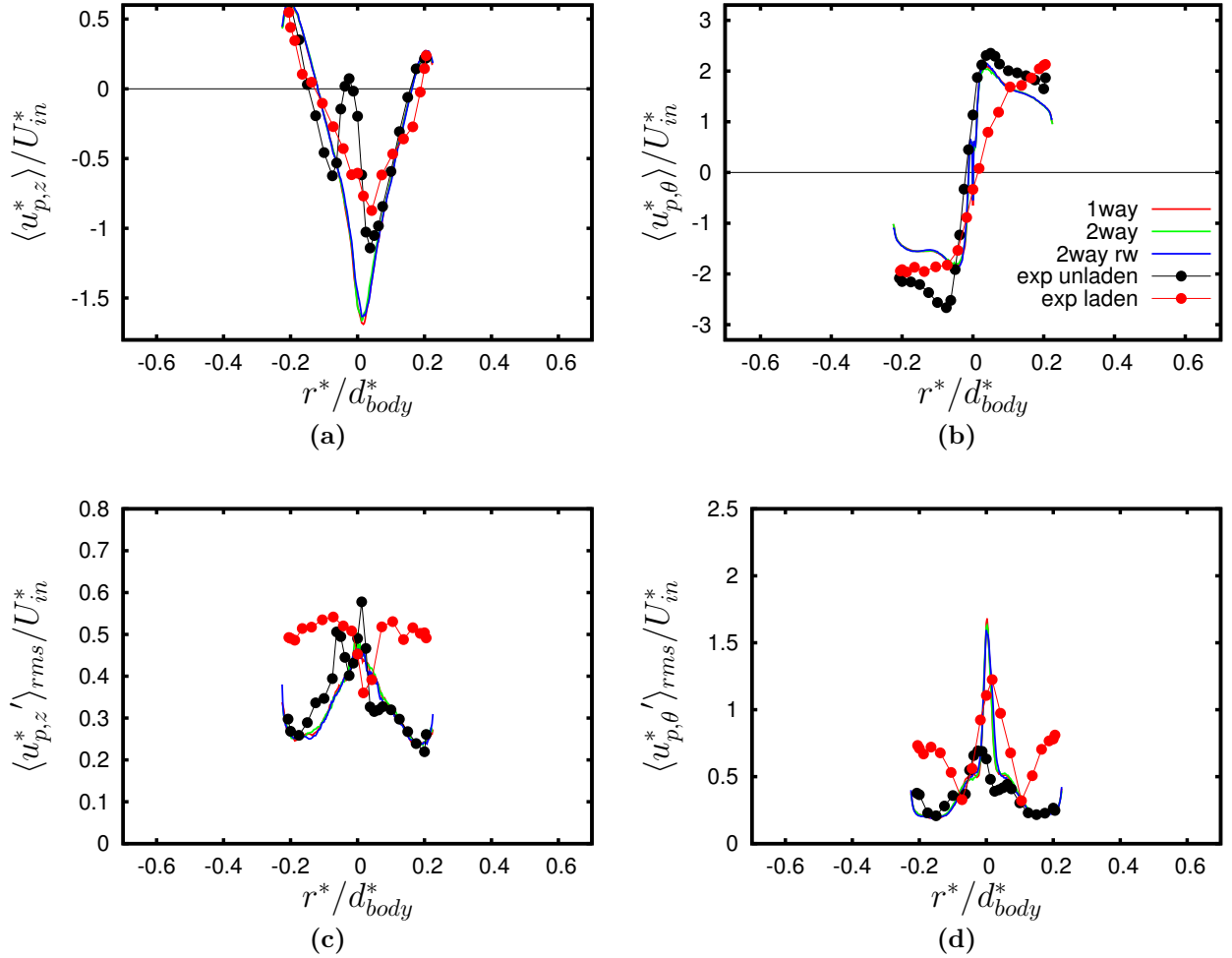


Figure 132: Mid part of the downcomer tube at $z^* = 217$ mm: Influence of the coupling and the wall roughness model for the particles on the particle statistics: (a) time-averaged axial velocity, (b) time-averaged circumferential velocity, (c) time-averaged axial velocity fluctuations, (d) time-averaged circumferential velocity fluctuations. For the legend see Fig. 131. Experiments by Obermair (2002).

enced by the turbulent motion but only a marginal effect of the wall boundary condition for the particles can be observed on the particle statistics.

8.8.3 Summary and Conclusions

In this section the unladen and the particle-laden flow in a cyclone separator was analyzed. In the first part the influence of the resolution and of the subgrid-scale model for the flow on the unladen fluid statistics was studied. The computed statistics were compared with the unladen flow LDA measurements of Obermair (2002). After that, the particle-laden flow was tackled. For this case three different simulations were compared with the LDA and the PDA measurements of Obermair (2002). A one-way and a two-way coupled simulation were performed in order to analyze the influence of the particles on the fluid. For these two simulations the particles were assumed to rebound at specular walls. In order to keep the computational cost of the two-way coupled flow at a reasonable level, the parcel method was applied. Furthermore, in order to investigate the influence of the

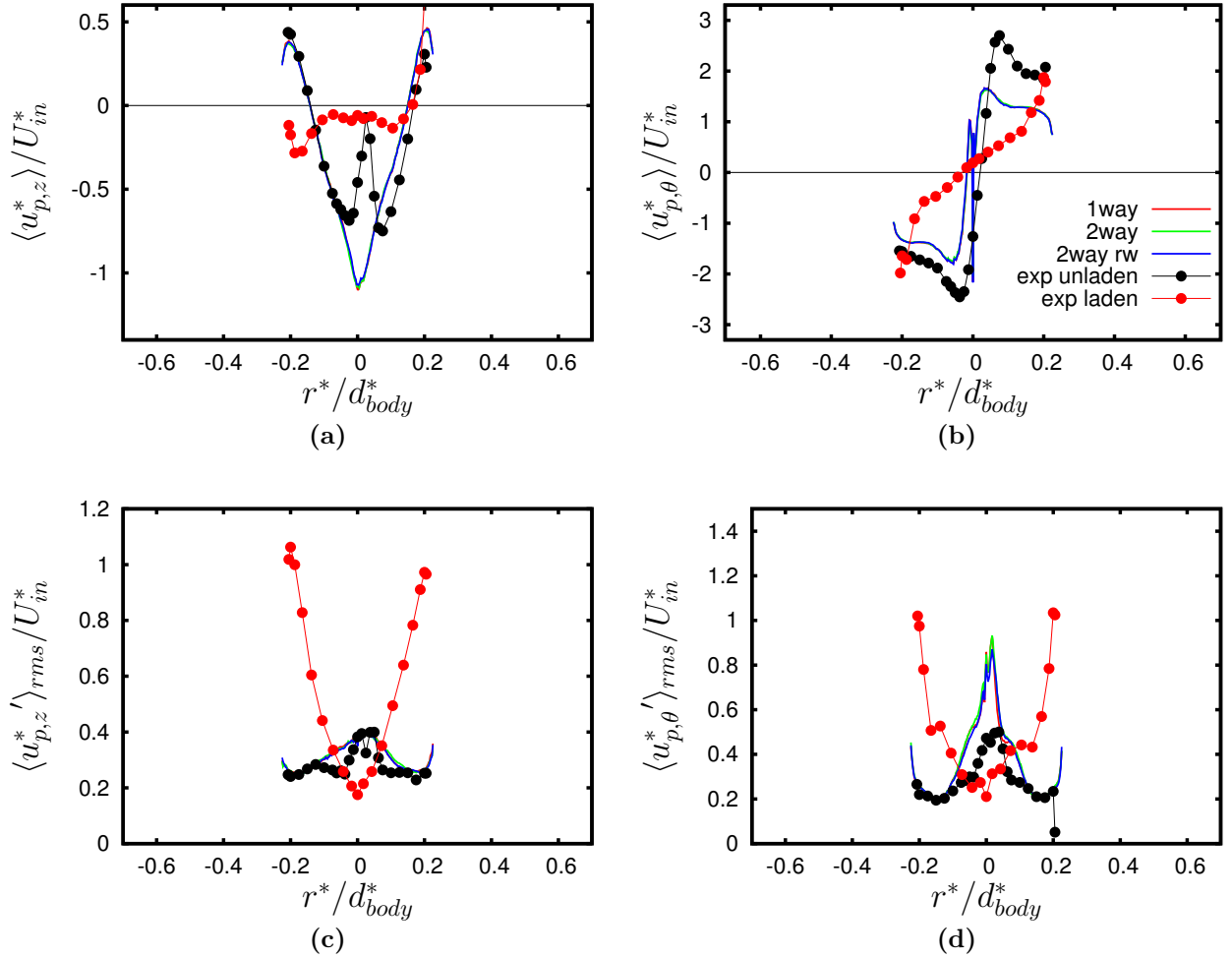


Figure 133: Lower part of the downcomer tube at $z^* = 401$ mm: Influence of the coupling and the wall roughness model for the particles on the particle statistics: (a) time-averaged axial velocity, (b) time-averaged circumferential velocity, (c) time-averaged axial velocity fluctuations, (d) time-averaged circumferential velocity fluctuations. For the legend see Fig. 131. Experiments by Obermair (2002).

rough walls seen by the particles on the particle and fluid statistics, a two-way coupled simulation with the rough wall boundary condition for the particles was performed. The following conclusions can be drawn:

- A big influence of the subgrid-scale model for the continuous flow can be asserted for the flow in a cyclone separator at a Reynolds number of 300,000 discretized by 5.6×10^6 control volumes. For increasing eddy viscosities μ_T the time-averaged circumferential velocity and the velocity fluctuations of the fluid decrease.
- Furthermore, a strong influence of the resolution can be observed. When increasing the number of control volumes employed from 4.4×10^6 to 5.6×10^6 an increase of the circumferential velocity and of the velocity fluctuations can be observed. For the finer grid the resolution at the walls and in the dust bin was slightly increased.
- Good agreement with the unladen flow experiments of Obermair (2002) can be achieved in the wall region of the cyclone. Unfortunately, some discrepancies in

the core region remain. These differences are: The mean axial flow in the cyclone core is directed towards the dust bin in the experiment. This feature cannot be reproduced by the simulation. The radial distance between the two maxima of the circumferential velocity in the core region is smaller in the simulations than in the experiment. The velocity fluctuations in the cyclone center are overpredicted by the simulations compared with the experiment.

- Regarding the particle-laden flow, Obermair (2002) observed in the downcomer tube a transition from a potential vortex found in the part closer to the inlet to a solid body vortex found in the region closer to the dust bin. He attributed this phenomenon to the decelerating effect of the particles located in the dust bin on the fluid. This effect cannot be reproduced by the simulations since the particles hitting the wall of the dust bin are removed from the computational domain in order to achieve a statistically stationary state and to reduce the computational costs to a feasible amount.
- The LES statistics computed for the continuous phase and the one computed for the disperse phase are very similar since only small particles are located in the cyclone.
- Only marginal differences between the particle statistics obtained with a one-way and a two-way coupled simulation assuming a smooth wall seen by the particles and a two-way coupled simulation assuming a rough wall can be observed. By removing the particles hitting the walls of the dust bin an overall small statistically stationary total mass of particles present in the cyclone of about only 0.085% of the fluid mass is predicted. This explains the vanishing difference between the one- and the two-way coupled simulation. Since the particles located in the computational domain are small, they are predominantly influenced by the turbulent motion of the fluid and not by the wall boundary conditions.
- Regarding the difference between the simulation and the experiment in the particle-laden configuration different explanation can be provided. Since in the experiment the dust bin is closed, the particle mass located inside the dust bin constantly increases in time leading after a while to a transition of the flow structure. That means that the force exerted by the particles on the fluid is high enough to lead to a transition of the flow configuration where the vortex reaches the bottom of the dust bin to a L-shaped vortex rotating around the bottom of the downcomer tube. In the simulation the particles are removed from the cyclone when they touch the walls of the dust bin and therefore the particle mass in the dust bin remains constant. An other explanation could be that in the experiment the particles are able to agglomerate at the walls of the cyclone. This leads to a higher wall roughness and therefore also a higher wall shear stress decelerating the vortex in the cyclone. In the simulation the influence of the increased wall roughness on the fluid flow can not be captured by the wall model for the fluid adopted. The combination of this two aforementioned effects can possibly explain the differences between the particle-laden experimental and simulation data. However, in the view of the big influence of the grid and also of the wall functions for the fluid, other reasons for the discrepancies between the simulation and the experiments in the particle-laden case are thinkable. Therefore, the definitive explanation of the big differences between the experiment and the simulation in the particle-laden case, is still open for discussion.

9 Conclusions and Outlook

9.1 Conclusions

Wall-bounded particle-laden flows in complex geometries play an important role in many industrial applications and natural phenomena. These flows are in almost all cases turbulent. For that reason it is indispensable to develop tools which correctly describe the interaction of the particles with the fluid including the turbulent motion, the particles among each other and the particles with bounding walls to accurately predict the flows mentioned above.

From an engineering point of view such methods should reliably predict the statistics of the carrier and the disperse phase, such as the mean velocities, the velocity fluctuations or the particle concentration. For highly unsteady or intermittent flows (e.g., combustion processes) it is furthermore important that the time-dependent local quantities are accurately reproduced.

From a physical point of view it is important to understand the phenomena appearing in turbulent particle-laden flows. This can be achieved by analyzing the complex interplay between the particles and the multiple of vortical scales present in a turbulent flow.

In order to tackle these challenges, the large-eddy simulation code *LESOC* (Breuer, 1998, 2002; Breuer et al., 2006) was further enhanced in this thesis. *LESOC* is an Euler-Lagrange solver describing the particles as point-particles. The original version of the tool relying on an eddy-resolving simulation concept was capable to describe two-way coupled flows. In the present study a highly efficient particle-particle collision handling and a new wall model describing the rebound of solid particles at rough walls was developed. The new wall model has the advantage over models present in the literature that a single roughness parameter such as the mean roughness height R_z^* or the root-mean square roughness R_q^* is required as a fundamental model parameter. Therefore, the model is applicable in designing industrial devices, where usually only R_z^* or R_q^* are used to characterize the surface roughness (Breuer, Alletto, and Langfeldt, 2012). The rough wall is modeled by a densely packed layer of mono-disperse spheres modeling sandgrain. The radius of the spheres is related to the given roughness parameter (R_q^* or R_z^*) requiring only one additional parameter ($C_{\text{surface}} \approx 3$ to 5) depending on the surface finishing also borrowed from the continuous phase (Schlichting, 1936; Hama, 1954; Zagarola and Smits, 1998; Shockling et al., 2006). Purely based on geometric and kinematic considerations an easy to use model is derived which mimics the most important influences of the rough walls on the rebound behavior of the solid particles, i.e., the redistribution of the streamwise momentum of the particles towards the wall-normal component (shadow effect) and the momentum loss of the particles, when hitting rough asperities.

The second key aspect of this thesis is the development of an efficient deterministic collision handling which is more accurate than stochastic models available in the literature (see, e.g., Sommerfeld, 2001). Due to the fast collision handling turbulent flows with high mass loadings can be computed. The efficiency of the method is underlined by the circumstance that the computational costs scale linearly with the number of particles present in the computational domain, whereas a standard brute-force implementation would result in computational costs which scale with the number of particles squared (Alletto and Breuer, 2014). The collision handling basically relies on a virtual cell concept: The computational domain is divided into virtual cells and only particles located in these virtual cells are checked against collision (Breuer and Alletto, 2012b). Furthermore, a

simple model which considers the influence of the subgrid-scales on the particle motion and an agglomeration model for frictional particle-particle collisions were presented.

The resulting method, especially the collision handling and the wall-roughness model for the particles, was tested and validated with the help of several test cases taken from the literature. These test cases consisted of flows in simple geometries such as the turbulent channel and pipe flows but also in complicated practically relevant flows such as the cold flow in a combustion chamber model and the particle-laden flow in a cyclone separator. The main conclusions which can be drawn from the application of the methodology presented in this thesis to the channel and pipe flows (see also Breuer, Alletto, and Langfeldt, 2012; Breuer and Alletto, 2012b, 2013, 2012c; Alletto and Breuer, 2013) are:

- Good agreement with a variety of experimental reference cases could be achieved.
- Inter-particle collisions taken into account in a turbulent channel or pipe flow lead to a flattening of the mean particle streamwise velocity profile, an enhancement of the particle velocity fluctuations and a homogenization of the particle concentration profile. All these observations can be explained by the enhancement of the momentum transfer between the particles induced by the collisions.
- In accordance with measurements, the application of the wall roughness model applied to turbulent channel and pipe flows leads to a momentum loss of the particles in streamwise direction. The momentum loss is strongly augmented with increasing wall roughness. That leads to particles which considerably lag behind the continuous flow. Two main reasons are identified for this behavior. Due to the shadow effect a redistribution of the streamwise momentum carried by the particles towards the wall-normal direction takes place. Additionally, the impact of the particles at the wall is stronger due to the higher wall-normal velocity fluctuations compared with a smooth wall configuration. This also leads to increased momentum loss.
- In close agreement with the measurements, the consideration of the influence of the wall roughness on the particle motion leads to an enhancement of the particle velocity fluctuations and a homogenization of the particle concentration throughout the cross-section.
- Due to the influence of the particles on the fluid (two-way coupling) a reduction of the fluid velocity fluctuations can be observed. Furthermore, a deceleration of the mean fluid flow in the regions of the highest particle concentration can be found.

Especially the successful simulation of the combustion chamber flow proves the applicability of the method for industrially relevant devices. The present study shows together with investigations already published by the author (Breuer and Alletto, 2011; Alletto and Breuer, 2012; Breuer and Alletto, 2012a,b) the first four-way coupled LES computation using an Euler-Lagrange method in complex geometries. These computations were possible because of the efficient collision handling presented here. The key findings of this application are the following:

- Good agreement with the experimental reference case could be achieved.
- A significant difference exists between the moderate and the high mass loading configuration. For the unladen and the moderate mass loading flow two stagnation

points are found on the axis of the chamber. For the high mass loading flow, however, these features completely disappear when the additional momentum induced by the particles is sufficiently high. The disappearance of the two stagnation points strongly influences the radial velocity fluctuations in the region close to the axis and thus also the radial dispersion of the particles. For the moderate mass loading a local maximum of the radial velocity fluctuations is observed near the second stagnation point indicating a strong mixing in this region. Therefore, the particles are significantly dispersed in this region. Contrarily, this effect is not visible for the high mass loading since the stagnation points vanished by the induced particle momentum. Furthermore, the particles are found to accumulate between the two stagnation points for the moderate mass loading, whereas this phenomenon is not observed for the high mass loading.

- For $\eta = 22\%$ the interaction between the fluid and the particles is found to play a major role, whereas the effect of the inter-particle collisions is negligible.
- For $\eta = 110\%$ the interaction between fluid and particles plays a major role. The deviations observed between the results of the one-way and two-way coupling strongly increase and the region where the fluid flow is influenced by the particulate phase is more extended. Contrarily, the effect of the inter-particle collisions is still minor for the high mass loading at the inlet.

Regarding the cyclone separator flow, unfortunately, some differences between the simulation and the experiment in the core region of the cyclone remain. The reason of this deviation can be probably explained by the big influence of the grid and the subgrid-scale model for the fluid. Based on this observation, it can be concluded that the resolution of the cyclone separator flow especially in the core region is still too low.

Also the second challenge postulated above, i.e., the improvement of the understanding of phenomena characterizing particle-laden turbulent flows, was successfully mastered. In this thesis the particle-laden flow in a horizontal pipe was simulated the first time by means of an eddy-resolving technique (see also Alletto and Breuer, 2013). The development of the interesting secondary-flow was found to be indirectly caused by the particles: Due to the gravitational settling the particles accumulate at the bottom of the pipe leading to a gradient of the circumferential Reynolds stress at the wall. Thus the anisotropy of the Reynolds stresses is identified as the driving force for the secondary flow. Therefore, the secondary flow is found to be of second kind and not of first kind. These findings are in agreement with the experimental work of Belt et al. (2012). The particles are not primarily responsible for the appearance of the secondary flow since they exert a net force against the mean flow direction in the pipe cross-section.

Summing up, in this work the parameter space and thus also the class of flows capable to be simulated by means of the code *LESOC* was considerably enhanced. Furthermore, some fundamental comprehension of turbulent particle-laden flows could be achieved.

9.2 Outlook

General Considerations

As mentioned in the introduction, the Lagrangian point-particle method applied in this thesis is flanked by the Euler-Euler and the fully-resolved approach. The border between

the point–particle and the fully–resolved approach is defined by the validity of the point–particle approach on the one hand and on the other hand by the computational costs of the fully–resolved approach. Concerning the border between the Euler–Euler and the point–particle approach similar considerations can be made. That means that when the computational costs for the point–particle approach are too high, the Euler–Euler approach has to be applied. Of course, when adopting a method based on the continuum assumption, it has to be ensured that a sufficiently high number of particles are present in each computational cell. If the number of particles per computational cell is too low (i.e., the continuum assumption is violated), the particles have to be treated in a Lagrangian frame of reference. Providing that the problem is feasible concerning the computational demands.

Possible future developments of the method presented here concern the shift of the borders between the simulation methods, i.e., the range of the parameter space, where the point–particles approach can be applied. The overpass of the border towards the fully resolved approach seems to be far from trivial. This would require to model the influence of the vortices generated behind the particles on the resolved scales, which is quite difficult. The enlargement of the parameter space feasible for the point–particle approach towards the parameter space belonging to the Euler–Euler approach seems to be more practicable. First, due to the increase of the computational power more particles than a few years ago can be tracked through the computational space. Thus the motion of smaller particles keeping the mass loading constant can be described. If the grid spacing is not adjusted accordingly, this requires the development of more accurate models describing the influence of the unresolved scales on the smaller particles having less inertia. Especially the preferential concentration of small particles caused by the unresolved scales is still an open issue in the literature worth to be investigated in the future.

Combination of the Parcel Method with the Deterministic Collision Model

In order to avoid waiting until the computational resources enable to track much more particles as possible nowadays, additional modeling assumptions are a remedy. If only two–way coupled flows are considered, the parcel method can be applied as already done in this thesis. Unfortunately, a direct application of the parcel method to four–way coupled flows using a deterministic collision algorithm is not trivial. In order to model the inter–particle collisions a stochastic model could be an option. The reason is that in contrast to deterministic models it can also be applied if not every real particle is tracked throughout the domain, i.e., using the parcel method. However, the application of a stochastic model such as the one described in Sommerfeld (2001) requires fully converged particle velocity fluctuations in order to compute the correct collision frequency. Applying the RANS approach this implies at least a few iterations starting from a two–way coupled flow. Therefore, for eddy–resolving techniques such as LES, which require very long computational times in order to produce converged statistics, this seem to be not the right method to choose in order to save computational time.

A possible alternative might be to exploit the functional dependency of the collision frequency per particle f_c^*/N_p from the particle diameter d_p^* and the number of particles N_p present in the computational domain (see, e.g., Sommerfeld, 2000; Wang et al., 2000; Borèe and Caraman, 2005, and references therein). f_c^*/N_p rises linearly with respect to N_p but is proportional to the particle diameter squared d_p^{*2} . It is obvious that if the parcel method is applied together with the collision handling presented in this thesis, the

correct collision frequency per particle is not captured. The reason is that the number of parcels tracked N_{parcel} does not correspond to the real number of particles present in the computational domain, i.e., $N_{parcel} = N_p/I_{parcel}$. I_{parcel} describes the number of particles grouped in a parcel. Therefore, the collision frequency per parcel $f_{c,parcel}^*/N_{parcel}$ is reduced compared with the real collision frequency.

In order to artificially rise the collision frequency per parcel $f_{c,parcel}^*/N_{parcel}$ and therefore to obtain the same collision frequency per parcel $f_{c,parcel}^*/N_{parcel}$ as the real collision frequency per real particle f_c^*/N_p , a fictive diameter of the parcels d_{parcel}^* can be introduced. d_{parcel}^* has to be larger than the particle diameter d_p^* by a factor of $\sqrt{I_{parcel}}$ in order to obtain the same collision frequency per parcel $f_{c,parcel}^*/N_{parcel}$ as the collision frequency per real particle f_c^*/N_p . Note that d_{parcel}^* should be only used in the collision detection procedure in order not to change the aerodynamic properties of the particles. This simple modification of the collision handling described in this thesis (after a careful validation) could be a valid alternative to the stochastic models to capture the influence of the inter-particle collisions even if not all real particles are tracked through the domain. In the opinion of the author the methodology described above could deliver reasonable results as long as the colliding parcels are not too far away from each other. That means that the two colliding parcels should be located in flow regions where the flow quantities are still correlated. Of course, when the fictive diameter of the parcels d_{parcel}^* is so large that a parcel located in the bulk flow collides with a parcel located in the boundary layer close to the wall, the methodology would deliver a totally wrong momentum transfer induced by collisions. Therefore, also a wrong velocity after the collision would be predicted.

Enhancement of the Wall Roughness Model

Regarding the wall roughness model for the particles, a possible enhancement could be the incorporation of the influence of grazing collisions. Konan et al. (2009) argued that even if a particle after its first wall collision would still move towards the wall or leave the wall with a very small deflection angle, in reality it would hit anyway a second wall asperity. This mechanism deflects the particle towards the inner part of the domain preventing an accumulation of the particles near the wall. Unfortunately, this mechanism is not captured by the model presented in this thesis. Therefore, the deficiency of the reproduction of this effect in the wall roughness model presented here could explain the high particle concentration seen close to the walls of the horizontal channel (see § 8.3).

A possible enhancement of the present wall roughness model considering also grazing collisions could provide the following methodology:

- (i) After the collision of the particles with the first wall sphere, it has to be verified if the trajectory of the particle crosses a second wall sphere placed after the first one. In order to verify if the aforementioned condition is fulfilled, a location of the second wall sphere has to be assumed. For example, it can be assumed that the center of the second wall sphere lies on the projection of the trajectory of the particle on the wall.
- (ii) If this condition is fulfilled, the wall-normal vector \mathbf{n}_{Rgrace} in case of a grazing collision can be computed and the post-collision state of the particles can be calculated with \mathbf{n}_{Rgrace} instead of \mathbf{n}_R .

With this measure the wall-normal component of the particle velocity after the grazing collision is larger than the one without considering the impact with a second wall sphere.

Therefore, the modeling of the grazing collision could prevent a large accumulation of the particles at the wall.

Future Steps concerning the Flow in the Cyclone Separator

Also regarding the flow in the cyclone separator some future works are possible. First of all, a more realistic condition for the removal of the particles from the computational domain is required. As visible in the pictures shown in the appendix of the dissertation of Obermair (2002), quite a lot of particles were deposited at the walls of the cyclone due to the influence of the van-der-Waals forces. Therefore, a physically motivated condition for the removal of the particles from the computational domain would be to verify if a particle sticks at the wall due to the influence of the van-der-Waals forces. If this condition is fulfilled, the particles can be removed. In order to reproduce this observation also in the simulation, criterion (5.115) can be easily modified in order to determine if a particle sticks at the wall due to the influence of the van-der-Waals forces. With this measure a physically motivated condition for the removal of the particles from the computational domain could be achieved.

A further measure to improve the results obtained in the cyclone is to perform additional computations on a finer grid. As shown in § 8.8, the subgrid-scale model for the fluid still has a large influence on the fluid statistics. Therefore, a higher resolution hopefully reduces this dependency providing a better accordance of the simulation results with the reference experiment.

A Grassmann and Lagrange Identity

The Grassmann identity reads (Merziger and Wirth, 1999):

$$(\mathbf{a} \times \mathbf{b}) \times \mathbf{c} = (\mathbf{a} \cdot \mathbf{c})\mathbf{b} - (\mathbf{b} \cdot \mathbf{c})\mathbf{a}. \quad (\text{A.1})$$

The Lagrange identity reads (Merziger and Wirth, 1999):

$$(\mathbf{a} \times \mathbf{b})^2 = \mathbf{a}^2\mathbf{b}^2 - (\mathbf{a} \cdot \mathbf{b})^2 \quad (\text{A.2})$$

B Total Kinetic Energy of a Rigid Body

In the determination of the total kinetic energy of a rigid body is recalled (see also Balke, 2011). The total kinetic energy E_{tot} is defined as follows:

$$E_{tot} = \frac{1}{2} \int_m \mathbf{v}_A^2 dm. \quad (\text{B.1})$$

\mathbf{v}_A is the velocity of a arbitrary point of the rigid body depicted in Fig. 134 and m is the mass of the rigid body. According to Balke (2011) the velocity of the point A can be decomposed into the velocity of the center of mass \mathbf{v}_S and a component resulting from the rotation of the rigid body:

$$\mathbf{v}_A = \mathbf{v}_S + \boldsymbol{\omega} \times \mathbf{r}_{SA}. \quad (\text{B.2})$$

After inserting eq. (B.2) into the definition of the total kinetic energy eq. (B.1) we obtain:

$$E_{tot} = \frac{1}{2} m \mathbf{v}_S^2 + 2 \mathbf{v}_S \cdot \underbrace{\boldsymbol{\omega} \int_m \mathbf{r}_{SA} dm}_{=0} + \frac{1}{2} \int_m (\boldsymbol{\omega} \times \mathbf{r}_{SA})^2 dm. \quad (\text{B.3})$$

Since the second term on the right-hand side of the above equation is zero per definition, the following relation is obtained:

$$E_{tot} = \frac{1}{2} m \mathbf{v}_S^2 + \frac{1}{2} \int_m (\boldsymbol{\omega} \times \mathbf{r}_{SA})^2 dm. \quad (\text{B.4})$$

The integrand on the right-hand side of the above equation can be written as follows:

$$(\boldsymbol{\omega} \times \mathbf{r}_{SA})^2 = (\omega_y r_{SA,z} - \omega_z r_{SA,y})^2 + (\omega_z r_{SA,x} - \omega_x r_{SA,z})^2 + (\omega_x r_{SA,y} - \omega_y r_{SA,x})^2 \quad (\text{B.5})$$

After inserting eq. (B.5) into the integral in eq. (B.4) it is easy to see that

$$\frac{1}{2} \int_m (\boldsymbol{\omega} \times \mathbf{r}_{SA})^2 dm = \frac{1}{2} \left[I_{xx} \omega_x^2 + I_{yy} \omega_y^2 + I_{zz} \omega_z^2 + 2(I_{yz} \omega_y \omega_z + I_{xz} \omega_x \omega_z + I_{xy} \omega_x \omega_y) \right]. \quad (\text{B.6})$$

I_{xx}, I_{yy}, \dots are the components of the inertial stress tensor $\underline{\underline{\mathbf{I}}}$. They are defined as follows:

$$I_{xx} = \int (r_{SA,y}^2 + r_{SA,z}^2) dm, \quad I_{yy} = \int (r_{SA,x}^2 + r_{SA,z}^2) dm, \quad I_{xy} = \int (r_{SA,x} r_{SA,y}) dm, \dots \quad (\text{B.7})$$

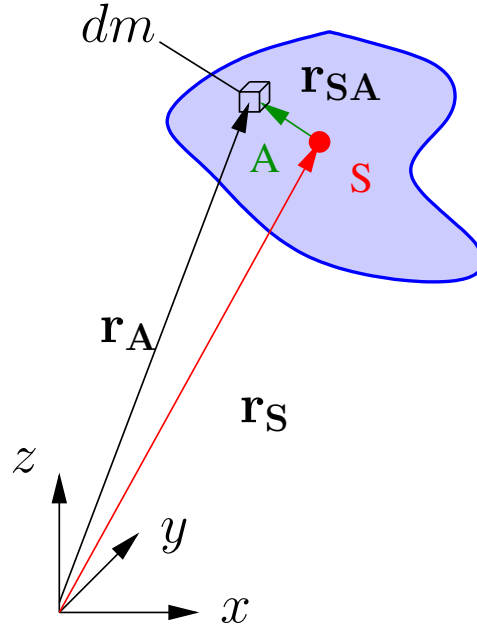


Figure 134: Coordinate system for the determination of the kinetic energy.

For coordinate systems which are aligned with the principal axis of $\underline{\mathbf{I}}$ the deviatoric moments vanish and a simple expression for the total kinetic energy is obtained.

C Treatment of the Agglomerate as a Hollow Sphere

In order to remove this inconsistency in the energy balance, the agglomerate can be treated as a hollow sphere with an inner diameter d_{ih} and an outer diameter d_{oh} . The particle density ρ_p is kept constant. The moment of inertia of a hollow sphere $\underline{\underline{\mathbf{I}_{hs}}}$ is calculated by:

$$\underline{\underline{\mathbf{I}_{hs}}} = \begin{pmatrix} 1/60 \pi \rho_p (d_{oh}^5 - d_{ih}^5) & 0 & 0 \\ 0 & 1/60 \pi \rho_p (d_{oh}^5 - d_{ih}^5) & 0 \\ 0 & 0 & 1/60 \pi \rho_p (d_{oh}^5 - d_{ih}^5) \end{pmatrix}. \quad (\text{C.1})$$

In order not to violate the energy balance, the rotational energy of the agglomerate and the rotational energy of the hollow sphere have to be equal:

$$\frac{1}{2} \underline{\underline{\mathbf{I}_{hs}}} \cdot \boldsymbol{\omega}_{hs,ntz}^2 = \frac{1}{2} \underline{\underline{\underline{\mathbf{I}_{ag,ntz}}}} \cdot \boldsymbol{\omega}_{ag,ntz}^2 \quad . \quad (\text{C.2})$$

Here $\boldsymbol{\omega}_{hs,ntz}$ denotes the angular velocity of the hollow sphere which is determined by means of the angular momentum balance:

$$\underline{\underline{\mathbf{I}_{hs}}} \cdot \boldsymbol{\omega}_{hs,ntz} = \underline{\underline{\underline{\mathbf{I}_{ag,ntz}}}} \cdot \boldsymbol{\omega}_{ag,ntz} \quad . \quad (\text{C.3})$$

Rearranging the above equation with respect to $\omega_{hs,ntz}$ leads together with eq. (5.116) to the following result:

$$\omega_{hs,ntz} = \frac{\underline{\underline{\mathbf{I}_{ag,ntz}}} \cdot \omega_{ag,ntz}}{1/60 \pi \rho_p (d_{oh}^5 - d_{ih}^5)} . \quad (C.4)$$

The required inertial moment of the hollow sphere is determined by inserting the above definition of $\omega_{hs,ntz}$ in the energy balance (5.117). The result of this operation reads:

$$\frac{(\underline{\underline{\mathbf{I}_{ag,ntz}}} \cdot \omega_{ag,ntz})^2}{1/60 \pi \rho_p (d_{oh}^5 - d_{ih}^5)} = \underline{\underline{\mathbf{I}_{ag,ntz}}} \cdot \omega_{ag,ntz}^2 \quad (C.5)$$

Hence, the inertial moment of the hollow sphere can be determined:

$$1/60 \pi \rho_p (d_{oh}^5 - d_{ih}^5) = \frac{(\underline{\underline{\mathbf{I}_{ag,ntz}}} \cdot \omega_{ag,ntz})^2}{\underline{\underline{\mathbf{I}_{ag,ntz}}} \cdot \omega_{ag,ntz}^2} . \quad (C.6)$$

The above relation still has the two unknowns d_{ih} and d_{oh} . The last relation to obtain the outer diameter of the hollow sphere d_{oh} (which is the main quantity of interest since it is required to calculate the fluid forces and also for the collision detection) is the mass conservation. The mass of the hollow sphere has to be equal to the mass of the two agglomerating particles:

$$\rho_p \frac{1}{6} \pi (d_{oh}^3 - d_{ih}^3) = \frac{1}{6} \pi \rho_p (d_{p,1}^3 + d_{p,2}^3) . \quad (C.7)$$

Finally by combining eq. (C.6) and eq. (C.7) a non-linear system of equations for d_{ih} and d_{oh} is obtained:

$$d_{oh}^5 - d_{ih}^5 = \frac{(\underline{\underline{\mathbf{I}_{ag,ntz}}} \cdot \omega_{ag,ntz})^2}{1/60 \pi \rho_p \underline{\underline{\mathbf{I}_{ag,ntz}}} \cdot \omega_{ag,ntz}^2} . \quad (C.8a)$$

$$d_{oh}^3 - d_{ih}^3 = d_{p,1}^3 + d_{p,2}^3 . \quad (C.8b)$$

Unfortunately, the author was not able to obtain an analytical solution of the above equation.

References

- DIN EN ISO 4287:2010-07. Geometrische Produktspezifikation (GPS) – Oberflächenbeschaffenheit: Tastschnittverfahren – Benennungen, Definitionen und Kenngrößen der Oberflächenbeschaffenheit; Geometrical product specifications (GPS) - surface texture: Profile method - terms, definitions and surface texture parameters.
- DIN 4760:1982-06. Gestaltabweichungen, Begriffe, Ordnungssystem; Form deviations, concepts, classification system.
- DIN ISO 9276-1:2004-09. Darstellung der Ergebnisse von Partikelgrößenanalysen–Teil 1: Grafische Darstellung; Representation of results of particle size analysis–Part 1: Graphical representation.
- M. Alletto and M. Breuer. One–way, two–way and four–way coupled LES predictions of a particle–laden turbulent flow at high mass loading downstream of a confined bluff body. *Int. J. Multiphase Flow*, 45:70–90, 2012.
- M. Alletto and M. Breuer. Prediction of turbulent particle–laden flow in horizontal smooth and rough pipes inducing secondary flow. *Int. J. Multiphase Flow*, 55:80–98, 2013.
- M. Alletto and M. Breuer. Large–eddy simulation of the particle–laden turbulent flow in a cyclone separator. In W. E. Nagel, D. B. Kröner, and M. M. Resch, editors, *High Performance Computing in Science and Engineering '13*, pages 377–391. Springer Berlin Heidelberg, 2014.
- N. Alvandifar, M. Abkar, Z. Mansoori, M. Saffar Avval, and G Ahmadi. Turbulence modulation for gas–particle flow in vertical tube and horizontal channel using four–way Eulerian–Lagrangian approach. *Int. J. Heat Fluid Flow*, 32(4):826–833, 2011.
- ANSYS. Ansys icem–cfd 12.0.1 linux 64–bit, 2009.
- H. M. Antia. *Numerical Methods for Scientists and Engineers*. Birkhaeuser, second edition, 2000.
- S. Antonyuk. *Deformations– und Bruchverhalten von kugelförmigen Granulaten bei Druck– und Stoßbeanspruchung*. PhD thesis, Otto–von–Guericke–Universität Magdeburg, Germany, 2006.
- S. V. Apte, M. Gorokhovski, and P. Moin. LES of atomizing spray with stochastic modeling of secondary breakup. *Int. J. Multiphase Flow*, 29(9):1503–1522, 2003a.
- S. V. Apte, K. Mahesh, P. Moin, and J. C. Oefelein. Large–eddy simulation of swirling particle–laden flows in a coaxial–jet combustor. *Int. J. Multiphase Flow*, 29(8):1311–1331, 2003b.
- B. Arcen, A. Tanière, and B. Oesterlé. On the influence of near–wall forces in particle–laden channel flows. *Int. J. Multiphase Flow*, 32(12):1326–1339, 2006.
- V. Armenio and V. Fiorotto. The importance of the forces acting on particles in turbulent flows. *Phys. Fluids*, 13:2437–2440, 2001.

- E. S. Asmolov and S. V. Manuilovich. Stability of a dusty-gas laminar boundary layer on a flat plate. *J. Fluid Mech.*, 365:137–170, 1998.
- J. S. Baggett, J. Jimenez, and A. G. Kravchenko. Resolution requirements in large-eddy simulations of shear flows. In *Annual Research Briefs*, pages 51–66, Center for Turbulence Research, Stanford, CA, 1997.
- S. Balachandar and J. K. Eaton. Turbulent dispersed multiphase flow. *Annu. Rev. Fluid Mech.*, 42:111–133, 2010.
- H. Balke. *Einführung in die technische Mechanik, Kinetik*. Springer DE, third edition, 2011.
- J. Bardina, J. H. Ferziger, and W. C. Reynolds. Improved subgrid-scale models for large-eddy simulations. *AIAA Paper*, 80–1357, 1980.
- R. J. Belt. *On the Liquid Film in Inclined Annular Flow*. PhD thesis, Delft University of Technology, The Netherlands, 2007.
- R. J. Belt, A. C. L. M. Daalman, and L. M. Portela. Experimental study of particle-driven secondary flow in turbulent pipe flows. *J. Fluid Mech.*, 709:1–36, 2012.
- L. Bennek. Numerische Simulation und Analyse der dispersen Mehrphasenströmung in einem Gaszyklon. Master’s thesis, Professur für Strömungsmechanik Helmut-Schmidt-Universität, Hamburg, 2012.
- C. Benocci and A. Pinelli. The role of the forcing term in large-eddy simulation of equilibrium channel flow. In W. Rodi and Ganić, editors, *Engineering Turbulence Modelling and Experiments 1*, pages 287–296. Elsevier Science Pub. Co., New York, 1990.
- M. Benson, T. Tanaka, and J. K. Eaton. Effects of wall roughness on particle velocities in a turbulent channel flow. *Trans. ASME J. Fluids Eng.*, 127:250–256, 2005.
- A. S. Berrouk. Stochastic large-eddy simulation of an axisymmetrical confined-bluff-body particle-laden turbulent flow. *American Journal of Fluid Dynamics*, 2:101–116, 2012.
- B. Bhushan. *Handbook of Micro/Nano Tribology*. Second edition. ISBN 0–8493–8402–8.
- C. S. Bierwisch. *Numerical Simulations of Granular Flow and Filling*. PhD thesis, University of Freiburg im Breisgau, Germany, 2009.
- M. J. Bijlard, R. V. A. Oliemans, L. M. Portela, and G. Ooms. Direct numerical simulation analysis of local flow topology in a particle-laden turbulent channel flow. *J. Fluid Mech.*, 653:35–56, 2010.
- M Bini and W. P Jones. Particle acceleration in turbulent flows: A class of nonlinear stochastic models for intermittency. *Phys. Fluids*, 19:035104–1–035104–9, 2007.
- M. Bini and W. P. Jones. Large-eddy simulation of particle-laden turbulent flows. *J. Fluid Mech.*, 614(1):207–252, 2008.

- B. Binninger. *Untersuchung von Modellströmungen in Zylindern von Kolbenmotoren*. PhD thesis, Aerodynamisches Institut, RWTH Aachen, 1989.
- G. A. Bird. *Molecular Gas Dynamics*. Claredon, first edition, 1976.
- B. J. Boersma. Direct numerical simulation of turbulent pipe flow at high reynolds numbers. In *14th European Turbulence Conference, 1–4 September 2013, Lyon, France*, 2013.
- M. Boivin, O. Simonin, and K.D. Squires. Direct numerical simulation of turbulence modulation by particles in isotropic turbulence. *J. Fluid Mech.*, 375:235–263, 1998.
- M. Boivin, O. Simonin, and K. D. Squires. On the prediction of gas–solid flows with two–way coupling using large–eddy simulation. *Phys. Fluids*, 12:2080–2090, 2000.
- J. Borèe and N. Caraman. Dilute bidispersed tube flow: Role of interclass collisions at increased loadings. *Phys. Fluids*, 17:055108–1–055108–9, 2005.
- J. Borée, T. Ishima, and I. Flour. The effects of mass loading and inter–particle collisions on the development of polydispersed two–phase flow downstream of a confined bluff body. *J. Fluid Mech.*, 443:129–165, 2001.
- Bormann. Digitizelt 1.5.8a, 2006.
- J. Boussinesq. *Essai sur la théorie des eaux courantes*. Imprimerie nationale, 1877.
- C. E. Brennen. *Fundamentals of Multiphase Flows*. Cambridge University Press, 2005.
- H. Brenner. The slow motion of a sphere through a viscous fluid towards a plane surface. *Chemical Engineering Science*, 16(3–4):242–251, 1961.
- M. Breuer. Large–eddy simulation of the sub–critical flow past a circular cylinder: Numerical and modeling aspects. *Int. J. Numer. Meth. Fluids*, 28(9):1281–1302, 1998.
- M. Breuer. *Direkte Numerische Simulation und Large–Eddy Simulation turbulenter Strömungen auf Hochleistungsrechnern*. Habilitationsschrift, Universität Erlangen–Nürnberg, Berichte aus der Strömungstechnik. Shaker Verlag, Aachen, 2002. ISBN 3–8265–9958–6.
- M. Breuer. *Numerische Strömungsmechanik, Vorlesungsskript*. Helmut–Schmidt–Universität Hamburg, 2011.
- M. Breuer. *LESOCC Manual: Large–Eddy Simulation on Curvilinear Coordinates*. Helmut–Schmidt–Universität Hamburg, edition: August, 2013.
- M. Breuer and M. Alletto. Two–phase flow predictions of the turbulent flow in a combustion chamber including particle–particle interactions. In *J. Physics: Conference Series*, volume 318, page 052002. IOP Publishing, 2011. doi: 10.1088/1742-6596/318/5/052002. 13th European Turbulence Conference (ETC13), Warsaw, Poland, Sept., 12–15, 2011.
- M. Breuer and M. Alletto. Numerical simulation of particle–laden turbulent flows using LES. In W. E. Nagel, D. B. Kröner, and M. M. Resch, editors, *High Performance Computing in Science and Engineering '11*, pages 337–352. Springer Berlin Heidelberg, 2012a. ISBN 978-3-642-23868-7.

- M. Breuer and M. Alletto. Efficient simulation of particle-laden turbulent flows with high mass loadings using LES. *Int. J. Heat Fluid Flow*, 35:2–12, 2012b.
- M. Breuer and M. Alletto. Application of a sandgrain roughness model in two-phase LES predictions of channel and pipe flows. In *13th Workshop on Two-Phase Flow Predictions*, Martin-Luther-Universität Halle-Wittenberg, Germany, 2012c.
- M. Breuer and M. Alletto. Effect of wall roughness seen by particles in turbulent channel and pipe flows. In W. E. Nagel, D. B. Kröner, and M. M. Resch, editors, *High Performance Computing in Science and Engineering '12*, pages 277–293. Springer Berlin Heidelberg, 2013. ISBN 978-3-642-33373-6. doi: 10.1007/978-3-642-33374-3_21.
- M. Breuer, H. T. Baytekin, and E. A. Matida. Prediction of aerosol deposition in 90 degrees bends using LES and an efficient Lagrangian tracking method. *J. Aerosol Science*, 37(11):1407–1428, 2006.
- M. Breuer, E. A. Matida, and A. Delgado. Prediction of aerosol drug deposition using an Eulerian-Lagrangian method based on LES. In *Int. Conf. on Multiphase Flow, July 9–13, 2007*, Leipzig, Germany, 2007.
- M. Breuer, M. Alletto, and F. Langfeldt. Sandgrain roughness model for rough walls within Eulerian-Lagrangian predictions of turbulent flows. *Int. J. Multiphase Flow*, 43: 157–175, 2012.
- J. Byerlee. Friction of rocks. *Pure and Applied Geophysics*, 116(4-5):615–626, 1978.
- C. S. Campbell. Rapid granular flow. *Annu. Rev. Fluid Mech.*, 22:57–92, 1990.
- M. Caporaloni, F. Tampieri, F. Trombetti, and O. Vittori. Transfer of particles in non-isotropic air turbulence. *J. Atmospheric Sciences*, 32:565–568, 1975.
- N. Caraman, J. Borèe, and O. Simonin. Effects of collisions on the dispersed phase fluctuations in a dilute tube flow: Experimental and theoretical analysis. *Phys. Fluids*, 15:3602–3612, 2003.
- C. Chan-Braun, M. García-Villalba, and M. Uhlmann. Force and torque acting on particles in a transitionally rough open-channel flow. *J. Fluid Mech.*, 684:441–474, 2011.
- M. Chen, K. Kontomaris, and J. B. McLaughlin. Direct numerical simulation of droplet collisions in a turbulent channel flow, part I: Collision algorithm. *Int. J. Multiphase Flow*, 24:1079–1103, 1998a.
- R. H. Chen, J. F. Driscoll, J. Kelly, M. Namazian, and R. W. Schefer. A comparison of bluff-body and swirl-stabilized flames. *Combustion Science Technology*, 71(4–6): 197–217, 1990.
- Y. C. Chen, C. C. Chang, K. L. Pan, and J. T. Yang. Flame lift-off and stabilization mechanisms of non-premixed jet flames on a bluff-body burner. *Combustion Flame*, 115(1–2):51–65, 1998b.
- M. Chrigui, A. Sadiki, and A. Zghal. Unsteady Euler/Lagrange simulation of a confined bluff-body gas-solid turbulent flow. 2010.

- D. Chung and B. J. McKeon. Large-eddy simulation of large-scale structures in long channel flow. *J. Fluid Mech.*, 661:341–364, 2010.
- P. W. Cleary. Industrial particle flow modelling using discrete element method. *Engineering Computations*, 26:698–743, 2009.
- C. T. Crowe, M. P. Sharma, and D. E. Stock. The Particle–Source–In–Cell (PSI–CELL) model for gas–droplet flows. *Trans. ASME J. Fluids Eng.*, 99:325–332, 1977.
- C. T. Crowe, M. Sommerfeld, and Y. Tsuji. *Multiphase Flows with Droplets and Particles*. CRC Press, 1998.
- Clayton T Crowe. On models for turbulence modulation in fluid–particle flows. *Int. J. Multiphase Flow*, 26(5):719–727, 2000.
- D. S. Dandy and H. A. Dwyer. A sphere in shear flow at finite Reynolds number: Effect of shear on particle lift, drag, and heat transfer. *J. Fluid Mech.*, 216:381–410, 1990.
- F. J. de Souza, R. de Vasconcelos Salvo, and D. A. de Moro Martins. Large-eddy simulation of the gas–particle flow in cyclone separators. *Separation and Purification Technology*, 94:61–70, 2012.
- S. Decker. *Zur Berechnung von gerührten Suspensionen mit dem Euler–Lagrange Verfahren*. PhD thesis, University Martin–Luther Halle–Wittenberg, Germany, 2004.
- S. C. R. Dennis, S. N. Singh, and D. B. Ingham. The steady flow due to a rotating sphere at low and moderate Reynolds numbers. *J. Fluid Mech.*, 101(02):257–279, 1980.
- J. J. Derksen. Separation performance prediction of a Stairmand high–efficiency cyclone. *AIChE Journal*, 49(6):1359–1371, 2003.
- J. J. Derksen. Numerical simulation of solids suspension in a stirred tank. *AIChE Journal*, 49(11):2700–2714, 2003b.
- J. J. Derksen, S. Sundaresan, and H. E. A. van den Akker. Simulation of mass–loading effects in gas–solid cyclone separators. *Powder Technology*, 163:59–68, 2006.
- J. J. Derksen, H. E. A. van den Akker, and S. Sundaresan. Two–way coupled large–eddy simulations of the gas–solid flow in cyclone separators. *AIChE Journal*, 54(4):872–885, 2008.
- C. D. Dritselis and N. S. Vlachos. Numerical study of educed coherent structures in the near–wall region of a particle–laden channel flow. *Phys. Fluids*, 20:055103–1–055103–12, 2008.
- C. D. Dritselis and N. S. Vlachos. Numerical investigation of momentum exchange between particles and coherent structures in low–Re turbulent channel flow. *Phys. Fluids*, 23:025103–1–025103–15, 2011a.
- C. D. Dritselis and N. S. Vlachos. Large–eddy simulation of gas–particle turbulent channel flow with momentum exchange between the phases. *Int. J. Multiphase Flow*, 37(7):706–721, 2011b.

- S. Elghobashi. On predicting particle-laden turbulent flows. *Applied Scientific Research*, 52:309–329, 1994. ISSN 0003-6994.
- S. Elghobashi and GC Truesdell. On the two-way interaction between homogeneous turbulence and dispersed solid particles. I: Turbulence modification. *Phys. Fluids A*, 5: 1790–1801, 1993.
- K. Elsayed and C. Lacor. The effect of cyclone vortex finder dimensions on the flow pattern and performance using les. *Computers & Fluids*, (71):224–239, 2012.
- C. Escauriaza and F. Sotiropoulos. Lagrangian model of bed-load transport in turbulent junction flows. *J. Fluid Mech.*, 666:36–76, 2011.
- J. D. Faires and R. L. Burden. *Numerische Methoden: Näherungsverfahren und ihre praktische Anwendung*. Spektrum, Akad. Verlag, 1994.
- M. Fairweather and J. Yao. Mechanisms of particle dispersion in a turbulent, square duct flow. *AIChE Journal*, 55(7):1667–1679, 2009.
- P. Fede and O. Simonin. Effect of polydispersion in bluff-body particle-laden flows. In *12th Workshop on Two-Phase Flow Predictions*, Halle (Saale), Germany, March 22–25, 2010, 2010.
- P. Fede, O. Simonin, P. Villedieu, and K. D. Squires. Stochastic modeling of turbulent subgrid fluid velocity along inertial particle trajectories. In *Proceedings of the 2006 CTR Summer Program*, pages 247–258, Center for Turbulence Research, Stanford, CA, 2006.
- J. Ferry and S. Balachandar. A fast Eulerian method for disperse two-phase flow. *Int. J. Multiphase Flow*, 27(7):1199–1226, 2001.
- J. Ferry, S. L. Rani, and S. Balachandar. A locally implicit improvement of the equilibrium Eulerian method. *Int. J. Multiphase Flow*, 29(6):869–891, 2003.
- J. H. Ferziger and Perić. *Computational Methods for Fluid Dynamics*. Springer, third edition, 2002.
- P. Fevrier, O. Simonin, and K. Squires. Partitioning of particle velocities in gas-solid turbulent flows into a continuous field and a spatially uncorrelated random distribution: Theoretical formalism and numerical study. *J. Fluid Mech.*, 533:1–46, 2005.
- S. F. Foerster, M. Y. Louge, H. Chang, and K. Allia. Measurements of the collision properties of small spheres. *Phys. Fluids*, 6(3):1108–1115, 1994.
- S. Fokeer, S. Kingman, I. Lowndes, and A. Reynolds. Characterization of the cross-sectional particle concentration distribution in horizontal dilute flow conveying, A review. *Chemical Engineering and Processing*, 43(6):677–691, 2004.
- Y. Forterre and O. Pouliquen. Flows of dense granular media. *Annu. Rev. Fluid Mech.*, 40(1):1–24, 2008.

- Th. Frank, K. P. Schade, and D. Petrak. Numerical simulation and experimental investigation of a gas–solid two–phase flow in a horizontal channel. *Int. J. Multiphase Flow*, 19:187–198, 1993.
- J. Fröhlich. *Large Eddy Simulation turbulenter Strömungen*. Springer, first edition, 2006.
- B. Frohnäpfel, P. Lammers, J. Jovanović, and F. Durst. Interpretation of the mechanism associated with turbulent drag reduction in terms of anisotropy invariants. *J. Fluid Mech.*, 277:457–466, 2007.
- K. Fukagata, S. Zahrai, S. Kondo, and F. H. Bark. Anomalous velocity fluctuations in particulate turbulent channel flow. *Int. J. Multiphase Flow*, 27:701–719, 2001.
- K. Fukagata, S. Zahrai, F. H. Bark, and S. Kondo. Influences of the near–wall drag correction in a Lagrangian simulation of particulate turbulent channel flow. In *Proc. 1st Int. Symp. on Turbulence and Shear Flow Phenomena*, pages 259–264, 1999.
- R. Gatignol. The Faxén formulae for a rigid particle in an unsteady non–uniform Stokes flow. *J. Méc. Theor. Appl.*, 1:143–160, 1983.
- M. Germano, U. Piomelli, P. Moin, and W. H. Cabot. A dynamic subgrid–scale eddy viscosity model. *Phys. Fluids A*, 3:1760–1765, 1991.
- B. J. Geurts and B. Vreman. Dynamic self–organization in particle–laden channel flow. *Int. J. Heat Fluid Flow*, 27(5):945–954, 2006.
- I. Goldhirsch. Rapid granular flow. *Annu. Rev. Fluid Mech.*, 35:267–292, 2003.
- A. J. Goldman, R. G. Cox, and H. Brenner. Slow viscous motion of a sphere parallel to a plane wall, part I: Motion through a quiescent fluid. *Chemical Engineering Science*, 22(4):637–651, 1967.
- P. Gondret, M. Lance, and L. Petit. Bouncing motion of spherical particles in fluids. *Phys. Fluids*, 14(2):643–652, 2002.
- G. Gronald and J. J. Derksen. Simulating turbulent swirl flow in a gas cyclone: A comparison of various modeling approaches. *Powder Technology*, 205:160–171, 2011.
- F. R. Hama. Boundary layer characteristics for smooth and rough surfaces. *Trans. Soc. Naval Archit. Mar. Eng.*, 62:333–358, 1954.
- H. C. Hamaker. The London–van der Waals attraction between spherical particles. *Physica*, 4(10):1058–1072, 1937.
- J. A. Hernández. Instabilities induced by concentration gradients in dusty gases. *J. Fluid Mech.*, 435:247–260, 2001.
- R. Hiller. *Der Einfluss von Partikelstoß und Partikelhaftung auf die Abscheidung in Faserfiltern*. PhD thesis, Universität Fridericiana Karlsruhe, Germany, 1981.
- A. T. Hjelmfelt and L. F. Mockros. Motion of discrete particles in a turbulent fluid. *Applied Scientific Research*, 16(1):149–161, 1966.

- A. C. Ho. *Modellierung der Partikelagglomeration im Rahmen des Euler/Lagrange-Verfahrens und Anwendung zur Berechnung der Staubabscheidung im Zyklon*. PhD thesis, Math.–Nat.–Techn. Tech. Fakultät, Martin–Luther–Universität Halle–Wittenberg, Germany, 2004.
- A. C. Ho and M. Sommerfeld. Modelling of micro–particle agglomeration in turbulent flows. *Chemical Engineering Science*, 57(15):3073–3084, 2002.
- B. P. B. Hoomans, J. A. M. Kuipers, W. J. Briels, and W. P. M. Van Swaaij. Discrete particle simulation of bubble and slug formation in a two–dimensional gas–fluidised bed: A hard–sphere approach. *Chemical Engineering Science*, 51(1):99–118, 1996.
- P. B. Hoomans, B. *Granular Dynamics of Gas–solid Two–phase Flows*. PhD thesis, Universiteit Twente, The Netherlands, 2000.
- M.A. Hopkins and M.Y. Louge. Inelastic microstructure in rapid granular flows of smooth disks. *Phys. Fluids A*, 3:47–57, 1991.
- S. Hoyas and J. Jiménez. Scaling of the velocity fluctuations in turbulent channels up to $Re_\tau = 2003$. *Phys. Fluids*, 18(1):011702, 2006.
- S. Hoyas and J. Jiménez. Reynolds number effect on the Reynolds–stress budgets in turbulent channels. *Phys. Fluids A*, 20:101511–1–101511–8, 2008.
- N. Huber. *Zur Phasenverteilung von Gas–Feststoff–Strömungen in Rohren*. PhD thesis, Universität Erlangen–Nürnberg, Germany, 1997.
- N. Huber and M. Sommerfeld. Modelling and numerical calculation of dilute–phase pneumatic conveying in pipe systems. *Powder Technology*, 99:90–101, 1998.
- M. Hussainov, A. Kartushinsky, A. Mulgi, and Ü. Rudi. Gas–solid flow with the slip velocity of particles in a horizontal channel. *J. Aerosol Science*, 27(1):41–59, 1996.
- I. E. Idelchik. *Handbook of Hydraulic Resistance*. Springer, second edition, 1986. ISBN 3–540–15962–2.
- S. Ilincic, N. Tungkunagorn, A. Vernes, G. Vorlaufer, P. A. Fotiu, and F. Franek. FEM–BEM contact mechanics on rough, artificial hip joints. *Proc. IMechE, Part J: J. Engineering Tribology*, 225(11):1081–1091, 2011.
- I. Iliopoulos and T. J. Hanratty. Turbulent dispersion in a non–homogeneous field. *J. Fluid Mech.*, 392:45–71, 1999.
- I. Iliopoulos, Y. Mito, and T. J. Hanratty. A stochastic model for solid particle dispersion in a non–homogeneous turbulent field. *Int. J. Multiphase Flow*, 29(3):375–394, 2003.
- J. N. Israelachvili. *Intermolecular and Surface Forces*. Academic Press, third edition, 2011.
- G. Jin, G. He, L. Wang, and J. Zhang. Subgrid–scale fluid velocity time–scales seen by inertial particles in large–eddy simulation of particle–laden turbulence. *Int. J. Multiphase Flow*, 36(5):432–437, 2010a.

- G. Jin, G. W. He, and L. P. Wang. Large-eddy simulation of turbulent collision of heavy particles in isotropic turbulence. *Phys. Fluids*, 22:055106–1–055106–13, 2010b.
- K. L. Johnson. *Contact Mechanics*. Cambridge University Press, 1989.
- G. G. Joseph, R. Zenit, M. L. Hunt, and A. M. Rosenwinkel. Particle–wall collisions in a viscous fluid. *J. Fluid Mech.*, 433:329–346, 2001.
- D. Jürgens. Modellierung und Simulation der Partikelagglomeration in turbulenten, dispersen Mehrphasenströmungen. Master’s thesis, Professur für Strömungsmechanik Helmut–Schmidt–Universität, Hamburg, 2012.
- T. Kajishima. Influence of particle rotation on the interaction between particle clusters and particle–induced turbulence. *Int. J. Heat Fluid Flow*, 25(5):721–728, 2004.
- T. Kajishima, S. Takiguchi, H. Hamasaki, and Y. Miyake. Turbulence structure of particle–laden flow in a vertical plane channel due to vortex shedding. *JSME Int. Journal Series B*, 44(4):526–535, 2001.
- A. I. Kartushinsky, E. E. Michaelides, Y. A. Rudi, S. V. Tisler, and I. N. Shcheglov. Numerical simulation of three–dimensional gas–solid particle flow in a horizontal pipe. *AIChE Journal*, 57(11):2977–2988, 2011.
- T. Kempe and J. Fröhlich. Collision modelling for the interface–resolved simulation of spherical particles in viscous fluids. *J. Fluid Mech.*, 709:445–489, 2012b.
- T. Kempe and J. Fröhlich. An improved immersed boundary method with direct forcing for the simulation of particle–laden flows. *J. Comput. Phys.*, 231(9):3663–3684, 2012a.
- J. Kim, P. Moin, and R. Moser. Turbulence statistics in fully developed channel flow at low Reynolds number. *J. Fluid Mech.*, 177:133–166, 1987.
- C. Kleinstreuer and Z. Zhang. Airflow and particle transport in the human respiratory system. *Annu. Rev. Fluid Mech.*, 42:301–334, 2010.
- N. A. Konan, O. Kannengieser, and O. Simonin. Stochastic modeling of the multiple rebound effects for particle–rough wall collisions. *Int. J. Multiphase Flow*, 35:933–945, 2009.
- N. A. Konan, O. Simonin, and K. D. Squires. Detached–eddy simulations and particle Lagrangian tracking of horizontal rough wall turbulent channel flow. *J. Turbulence*, 12(22):1–21, 2011.
- J. G. M. Kuerten. Subgrid modeling in particle–laden channel flow. *Phys. Fluids*, 18(2):025108, 2006.
- J. G. M. Kuerten and A. W. Vreman. Can turbophoresis be predicted by large–eddy simulation? *Phys. Fluids*, 17(1):11701, 2005.
- J. D. Kulick, J. R. Fessler, and J. K. Eaton. Particle response and turbulence modification in fully developed channel flow. *J. Fluid Mech.*, 277:109–134, 1994.

- R. Kurose and S. Komori. Drag and lift forces on a rotating sphere in a linear shear flow. *J. Fluid Mech.*, 384:183–206, 1999.
- J. Kussin. *Experimentelle Studien zur Partikelbewegung und Turbulenzmodifikation in einem horizontalen Kanal bei unterschiedlichen Wandrauigkeiten*. PhD thesis, Martin–Luther–Universität Halle–Wittenberg, Germany, 2004.
- J. Kussin and M. Sommerfeld. Experimental studies on particle behavior and turbulence modification in horizontal channel flow with different wall roughness. *Experiments Fluids*, 33:143–159, 2002.
- S. Lain and M. Sommerfeld. Euler/Lagrange computations of pneumatic conveying in a horizontal channel with different wall roughness. *Powder Technology*, 184:76–88, 2008.
- S. Lain and M. Sommerfeld. Numerical calculation of pneumatic conveying in horizontal channels and pipes: Detailed analysis of conveying behavior. *Int. J. Multiphase Flow*, 39:105–120, 2012.
- S. Lain, M. Sommerfeld, and J. Kussin. Experimental studies and modelling of four–way coupling in particle–laden horizontal channel flow. *Int. J. Heat Fluid Flow*, 23:647–656, 2002.
- A. R. Lambert, P. T. O’Shaughnessy, M. H. Tawhai, E. A. Hoffman, and C. L. Lin. Regional deposition of particle in an image–based airway model: Large–eddy simulation and left–right lung ventilation asymmetry. *Aerosol Sci. Technol.*, 45:11–25, 2011.
- H. Lee and S. Balachandar. Drag and lift forces on a spherical particle moving on a wall in a shear flow at finite Re. *J. Fluid Mech.*, 657:89–125, 2010.
- K. Lei, N. Taniguchi, and T. Kobayashi. Large–eddy simulation of particle–laden turbulent channel flow considering SGS coupling. *JSME Int. Journal Series B*, 45(1):164–173, 2002.
- D. C. Leslie and G. L. Quarini. The application of turbulence theory to the formulation of subgrid modelling procedures. *J. Fluid Mech.*, 91(01):65–91, 1979.
- J. Li and J. A. M. Kuipers. Gas–particle interactions in dense gas–fluidized beds. *Chemical Engineering Science*, 58(3–6):711–718, 2003.
- T. Li, J. Grace, and X. Bi. Study of wall boundary condition in numerical simulations of bubbling fluidized beds. *Powder Technology*, 203(3):447–457, 2010.
- Y. Li, J. B. McLaughlin, K. Kontomaris, and L. Portela. Numerical simulation of particle–laden turbulent channel flow. *Phys. Fluids*, 13(10):2957–2967, 2001.
- D. K. Lilly. A proposed modification of the Germano subgrid–scale closure method. *Phys. Fluids A*, 4:633–635, 1992.
- F. Löffler and W. Muhr. Die Abscheidung von Feststoffteilchen und Tropfen an Kreiszyllindern infolge von Trägheitskräften. *Chemie Ingenieur Technik*, 44(8):510–514, 1972.
- F. Lucci, A. Ferrante, and S. Elghobashi. Modulation of isotropic turbulence by particles of Taylor length–scale size. *J. Fluid Mech.*, 650:5–55, 2010.

- J. L. Lumley. Computational modeling of turbulent flows. *Adv. Appl. Mech.*, 18:123–176, 1978.
- J. L. Lumley and G. Newman. The return to isotropy of homogeneous turbulence. *J. Fluid Mech.*, 82:161–178, 1977.
- C. K. K. Lun and H. S. Liu. Numerical simulation of dilute turbulent gas–solid flows in horizontal channels. *Int. J. Multiphase Flow*, 23(3):575–605, 1997.
- E. Macherauch and H. W. Zoch. Topographie von Werkstoffoberflächen. In *Praktikum in Werkstoffkunde*, pages 145–151. Vieweg+Teubner, 2011. ISBN 978-3-8348-9884-5.
- K. Mahesh, G. Constantinescu, and P. Moin. A numerical method for large–eddy simulation in complex geometries. *J. Comput. Phys.*, 197(1):215–240, 2004.
- G. Mallouppas and B. van Wachem. Large–eddy simulations of turbulent particle–laden channel flow. *Int. J. Multiphase Flow*, 54:65–75, 2013.
- F. E. Marble. Dynamics of dusty gases. *Annu. Rev. Fluid Mech.*, 2:397–446, 1970.
- C. Marchioli and A. Soldati. Mechanism for particle transport and segregation in a turbulent boundary layer. *J. Fluid Mech.*, 468:283–315, 2002.
- C. Marchioli, A. Giusti, M. V. Salvetti, and A. Soldati. Direct numerical simulation of particle wall transfer and deposition in upward turbulent pipe flow. *Int. J. Multiphase Flow*, 29:1017–1038, 2003.
- C. Marchioli, V. Armenio, and A. Soldati. Simple and accurate scheme for fluid velocity interpolation for Eulerian–Lagrangian computation of dispersed flow in 3D curvilinear grids. *Computers & Fluids*, 36:1187–1198, 2007a.
- C. Marchioli, M. Picciotto, and A. Soldati. Influence of gravity and lift on particle velocity statistics and transfer rates in turbulent vertical channel flow. *Int. J. Multiphase Flow*, 33:227–251, 2007b.
- C. Marchioli, M. V. Salvetti, and A. Soldati. Some issues concerning large–eddy simulation of inertial particle dispersion in turbulent bounded flows. *Phys. Fluids*, 20(4):040603, 2008a.
- C. Marchioli, M. V. Salvetti, and A. Soldati. Appraisal of energy recovering subgrid–scale models for large–eddy simulation of turbulent dispersed flows. *Acta Mechanica*, 201(1): 277–296, 2008b.
- C. Marchioli, A. Soldati, J. G. M. Kuerten, B. Arcen, A. Tanière, G. Goldensohn, K. D. Squires, M. F. Cargnelutti, and L.M. Portela. Statistics of particle dispersion in direct numerical simulations of wall–bounded turbulence: Results of an international collaborative benchmark test. *Int. J. Multiphase Flow*, 34:879–893, 2008c.
- M. R. Maxey and J. J. Riley. Equation of motion for a small rigid sphere in a non–uniform flow. *Phys. Fluids*, 26:883–889, 1983.
- J. B. McLaughlin. Inertial migration of a small sphere in linear shear flows. *J. Fluid Mech.*, 224:261–274, 1991.

- G. Merziger and T. Wirth. *Repetitorium der höheren Mathematik*. 1999.
- D. W. Meyer. Modelling of turbulence modulation in particle- or droplet-laden flows. *J. Fluid Mech.*, 706:251–273, 2012.
- E. E. S. Michaelides. *Heat and Mass Transfer in Particulate Suspensions*. Springer, 2013.
- J. P. Minier. Lagrangian stochastic modeling of turbulent flows. In *Advances in Turbulence Modeling*, Von Karmán Institute for Fluid Dynamics, Belgium, 1998.
- J. P. Minier, E. Peirano, and S. Chibbaro. PDF model based on Langevin equation for polydispersed two-phase flows applied to a bluff-body gas-solid flow. *Phys. Fluids*, 16(7):2419–2431, 2004.
- M. Namazian, J. Kelly, R. W. Schefer, S. C. Johnston, and M. B. Long. Nonpremixed bluff-body burner flow and flame imaging study. *Experiments Fluids*, 8:216–228, 1989.
- H. Nasr, G. Ahmadi, and J. B. McLaughlin. A DNS study of effects of particle-particle collisions and two-way coupling on particle deposition and phasic fluctuations. *J. Fluid Mech.*, 640:507–536, 2009.
- J. Nikuradse. Strömungsgesetze in rauhen Röhren. *Forsch.-Arb. Ing.-Wes.*, 361, 1933.
- S. Obermair. *Einfluss der Feststoffaustragungsgeometrie auf die Abscheidungsrate und den Druckverlust eines Gaszyklons*. PhD thesis, Technische Universität Graz, Austria, 2002.
- S. Obermair, J. Woisetschläger, and Staudinger G. Investigation of the flow pattern in different dust outlet geometries of a gas cyclone by laser Doppler anemometry. *Powder Technology*, 138:239–251, 2003.
- S. Obermair, C. Gutsch, J. Woisetschläger, and Staudinger G. Flow pattern and agglomeration in the dust outlet of a gas cyclone investigated by phase Doppler anemometry. *Powder Technology*, 156:34–42, 2005.
- J. C. Oefelein, V. Sankaran, and T. G. Drozda. Large-eddy simulation of swirling particle-laden flow in a model asymmetric combustor. *Proc. Combustion Institute*, 31(2):2291–2299, 2007.
- B. Oesterlé and T. Bui Dinh. Experiments on the lift of a spinning sphere in a range of intermediate Reynolds numbers. *Experiments Fluids*, 19:16–22, 1998.
- A. D. Paris. *Turbulence Attenuation in a Particle-Laden Channel Flow*. PhD thesis, Mech. Eng. Dept., Stanford University, USA, 2001.
- W. Peng, A. C. Hoffmann, H. W. A. Dries, M. A. Regelink, and L. E. Stein. Experimental study of the vortex end in centrifugal separators: The nature of the vortex end. *Chemical Engineering Science*, 60(24):6919–6928, 2005.
- B. N. J. Persson, O. Albohr, U. Tartaglino, A. I. Volokitin, and E. Tosatti. On the nature of surface roughness with application to contact mechanics, sealing, rubber friction and adhesion. *J. Phys.: Condens. Matter*, 17:R1–R62, 2005.

- U. Piomelli and J. R. Chasnov. Large-eddy simulations: Theory and applications. In M. Hallböck, D.S. Henningson, A.V. Johansson, and P.H. Alfredson, editors, *Turbulence and Transition Modeling*, pages 269–331. Kluwer, 1996.
- S. Pirker, D. Kahrimanovic, C. Kloss, B. Popoff, and M. Braun. Simulating coarse particle conveying by a set of Eulerian, Lagrangian and hybrid particle models. *Powder Technology*, 204(2–3):203–213, 2010.
- G. I. Pisarev, A. C. Hoffmann, W. Peng, and H. A. Dijkstra. Large eddy simulation of the vortex end in reverse-flow centrifugal separators. *Applied mathematics and computation*, 217(11):5016–5022, 2011.
- J. Pozorski and S. V. Apte. Filtered particle tracking in isotropic turbulence and stochastic modeling of subgrid-scale dispersion. *Int. J. Multiphase Flow*, 35:118–128, 2009.
- Sarma L. Rani, C.M. Winkler, and S.P. Vanka. Numerical simulations of turbulence modulation by dense particles in a fully developed pipe flow. *Powder Technology*, 141(1–2):80–99, 2004.
- B. Ray and L. R. Collins. Preferential concentration and relative velocity statistics of inertial particles in Navier–Stokes turbulence with and without filtering. *J. Fluid Mech.*, 680:488–510, 2011.
- H. Reichardt. Vollständige Darstellung der turbulenten Geschwindigkeitsverteilung in glatten Leitungen. *Zeitschrift für Angewandte Mathematik und Mechanik*, 31:208–219, 1951.
- C. M. Rhie and W. L. Chow. Numerical study of the turbulent flow past an airfoil with trailing edge separation. *AIAA journal*, 21(11):1525–1532, 1983.
- E. Riber, M. Moreau, O. Simonin, and B. Cuenot. Towards large-eddy simulation of non-homogeneous particle-laden turbulent gas flows using Euler–Euler approach. In *11th Workshop on Two-Phase Flow Predictions, Merseburg, Germany*, volume 51, pages 183–200, 2005.
- E. Riber, V. Moureau, M. Garcia, T. Poinsot, and O. Simonin. Evaluation of numerical strategies for large-eddy simulation of particulate two-phase recirculating flow. *J. Comput. Phys.*, 228:539–564, 2009.
- J. C. Rotta. *Turbulente Strömungen*. B.G. Teubner, Stuttgart, 1972.
- D. W. I. Rouson and J. K. Eaton. On the preferential concentration of solid particles in turbulent channel flow. *J. Fluid Mech.*, 428:149–169, 2001.
- S. I. Rubinow and J. B. Keller. The transverse force on a spinning sphere moving in a viscous fluid. *J. Fluid Mech.*, 11:447–459, 1961.
- P. G. Saffman. On the stability of laminar flow of dusty gas. *J. Fluid Mech.*, 13:120–128, 1962.
- P. G. Saffman. The lift on a small sphere in a slow shear flow. *J. Fluid Mech.*, 22:385–400, 1964.

- P. Sagaut. *Large-Eddy Simulation for Incompressible Flows*. Springer Berlin, third edition, 2006.
- F. Schäfer and M. Breuer. Comparison of c-space and p-space particle tracing schemes on high-performance computers: Accuracy and performance. *Int. J. Numer. Meth. Fluids*, 39(4):277–299, 2002.
- R. W. Schefer, M. Namazian, and J. Kelly. Velocity measurements in a turbulent non-premixed bluff-body stabilized flame. *Combustion Science Technology*, 56(4–6):101–138, 1987.
- R. W. Schefer, M. Namazian, and J. Kelly. Velocity measurements in a turbulent bluff-body stabilized flow. *AIAA Journal*, 9:1844–1851, 1994.
- L. Schiller and A. Naumann. A drag coefficient correlation. *VDI Zeitschrift*, 77:318–320, 1933.
- H. Schlichting. Experimentelle Untersuchungen zum Rauigkeitsproblem. *Archive of Applied Mechanics*, 7:1–34, 1936. ISSN 0939–1533.
- H. Schlichting and K. Gersten. *Boundary-Layer Theory*. Springer Verlag, 2000.
- U. Schumann. Subgrid-scale model for finite-difference simulations of turbulent flows in plane channels and annuli. *J. Comput. Phys.*, 18:376–404, 1975.
- J. C. Segura. *Predictive Capabilities of Particle-laden Large-Eddy Simulation*. PhD thesis, Stanford University, USA, 2004.
- R. A. Serway and C. Vuille. *Essentials of college physics*. Thomson, first edition, 2006.
- H. H. Shalaby. *On the Potential of Large eddy Simulation to Simulate Cyclone Separators*. PhD thesis, Technischen Universität Chemnitz, Germany, 2007.
- X. Shao, T. Wu, and Z. Yu. Fully resolved numerical simulation of particle-laden turbulent flow in a horizontal channel at a low Reynolds number. *J. Fluid Mech.*, 693:319–344, 2012.
- X. Shi, R. Qian, H. Shi, and C. Zheng. Investigation of the optimization of slit width for a slitted bluff-body burner: Pulverized coal ignition and flame stabilization. *Combustion Science Technology*, 124(1–6):1–15, 1997.
- M. A. Shockling, J. J. Allem, and A. J. Smits. Roughness effects in turbulent pipe flow. *J. Fluid Mech.*, 564:267–285, 2006.
- B. Shotorban and F. Mashayek. Modeling subgrid-scale effects on particles by approximate deconvolution. *Phys. Fluids*, 17:081701–1–08170–4, 2005.
- M. D. Slack, R. O. Prasad, A. Bakker, and F. Boysan. Advances in cyclone modelling using unstructured grids. *Chemical Engineering Research and Design*, 78(8):1098–1104, 2000.
- J. Smagorinsky. General circulation experiments with the primitive equations, I, The basic experiment. *Monthly Weather Review*, 91:99–165, 1963.

- G. Solero and A. Coghe. Experimental fluid dynamic characterization of a cyclone chamber. *Experimental Thermal and Fluid Science*, 27(1):87–96, 2002.
- M. Sommerfeld. Modelling of particle–wall collisions in confined gas–particle flows. *Int. J. Multiphase Flow*, 18(6):905–926, 1992.
- M. Sommerfeld. Theoretical and experimental modelling of particulate flows. In *Lecture Series 2000–06, von Kármán Institute for Fluid Dynamics*, 2000.
- M. Sommerfeld. Validation of a stochastic Lagrangian modelling approach for inter–particle collisions in homogeneous isotropic turbulence. *Int. J. Multiphase Flow*, 27:1829–1858, 2001.
- M. Sommerfeld. Analysis of collision effects for turbulent gas–particle flow in a horizontal channel: Part I. Particle transport. *Int. J. Multiphase Flow*, 29:675–699, 2003.
- M. Sommerfeld and S. Decker. State–of–the–art and future trends in CFD simulation of stirred vessel hydrodynamics. *Chemical Engineering & Technology*, 27(3):215–224, 2004.
- M. Sommerfeld and N. Huber. Experimental analysis and modelling of particle–wall collisions. *Int. J. Multiphase Flow*, 25:1457–1489, 1999.
- M. Sommerfeld and J. Kussin. Analysis of collision effects for turbulent gas–particle flow in a horizontal channel: Part II. Integral properties and validation. *Int. J. Multiphase Flow*, 29:701–718, 2003.
- M. Sommerfeld and J. Kussin. Wall roughness effect on pneumatic conveying of spherical particles in a narrow horizontal channel. *Powder Technology*, 142:180–192, 2004.
- M. Sommerfeld and H. H. Qiu. Characterization of particle–laden, confined swirling flows by phase–Doppler anemometry and numerical calculation. *Int. J. Multiphase Flow*, 19(6):1093–1127, 1993.
- M. Sommerfeld, B. von Wachem, and R. Oliemans. Best practice guidelines for computational fluid dynamics of dispersed multiphase flows. In *SIAMUF, Swedish Industrial Association for Multiphase Flows, ERCOFTAC*, 2008. ISBN 978–91–633–3564–8.
- C. G. Speziale. On turbulent secondary flows in pipes of non–circular cross–section. *Int. J. Engng. Sci.*, 20(7):863–872, 1982.
- K. D. Squires and O. Simonin. LES–DPS of the effect of wall roughness on dispersed–phase transport in particle–laden turbulent channel flow. *Int. J. Heat Fluid Flow*, 27:619–626, 2006.
- H. L. Stone. Iterative solution of implicit approximations of multidimensional partial differential equations. *SIAM J. Num. Anal.*, 5:530–558, 1968.
- T. Strömberg, G. Brethouwer, G. Amberg, and A. V. Johansson. A modelling study of evolving particle–laden turbulent pipe–flow. *Flow Turbulence Combust.*, 86(3):477–495, 2011.

- S. Sundaram and L. Collins. Numerical considerations in simulating a turbulent suspension of finite-volume particles. *J. Comput. Phys.*, 124(2):337–350, 1996.
- S. Sundaram and L. R. Collins. Collision statistics in an isotropic particle-laden turbulent suspension. Part 1. Direct numerical simulation. *J. Fluid Mech.*, 335:75–109, 1997.
- M. Suzuki and M. Yamamoto. Numerical simulation of sand erosion phenomena in a single-stage axial compressor. *Journal Fluid Science Technology*, 6(1):98–113, 2011.
- T. Tanaka and Y. Tsuji. Numerical simulation of gas–solid two–phase flow in a vertical pipe: on the effect of inter–particle collision. In *4th Int. Symp. on Gas–Solid Flows, In: Gas–Solid Flows*, volume 121, pages 123–128. ASME, 1991.
- J. Tomas. Adhesion of ultrafine particles—A micromechanical approach. *Chemical Engineering Science*, 62(7):1997–2010, 2007.
- M. Uhlmann. An immersed boundary method with direct forcing for the simulation of particulate flows. *J. Comput. Phys.*, 209(2):448–476, 2005.
- M. Uhlmann. Interface–resolved direct numerical simulation of vertical particulate channel flow in the turbulent regime. *Phys. Fluids*, 20(5):053305, 2008.
- M. A. van der Hoef, M. van Sint Annaland, N.G. Deen, and J. A. M. Kuipers. Numerical simulation of dense gas–solid fluidized beds: A multiscale modeling strategy. *Annu. Rev. Fluid Mech.*, 40(1):47–70, 2008.
- E. R. Van Driest. On turbulent flow near a wall. *J. Aero. Sci.*, pages 1007–1011, 1956.
- B. G. M. Van Wachem, J. C. Schouten, C. M. Van den Bleek, R. Krishna, and J. L. Sinclair. Comparative analysis of CFD models of dense gas–solid systems. *AIChE Journal*, 47(5):1035–1051, 2001.
- J. M. C. van ’t Westende, R.J. Belt, L.M. Portela, R.F. Mudde, and R.V.A. Oliemans. Effect of secondary flow on droplet distribution and deposition in horizontal annular pipe flow. *Int. J. Multiphase Flow*, 33(1):67–85, 2007.
- G. Viccione, V. Bovolin, and E. Pugliese Carratelli. Defining and optimizing algorithms for neighboring particle identification in SPH fluid simulations. *Int. J. Numer. Meth. Fluids*, 58:625–638, 2008.
- I. Vinkovic, C. Aguirre, M. Ayrault, and S. Simoëns. Large–eddy simulation of the dispersion of solid particles in a turbulent boundary layer. *Boundary–Layer Meteorology*, 121(2):283–311, 2006.
- A. W. Vreman. Turbulence characteristics of particle–laden pipe flow. *J. Fluid Mech.*, 584:235–279, 2007.
- B. Vreman, B. J. Geurts, N. G. Deen, J. A. M. Kuipers, and J. G. M. Kuerten. Two– and four–way coupled Euler–Lagrangian large–eddy simulation of turbulent particle–laden channel flow. *Flow Turbulence Combustion*, 82(1):47–71, 2009.

- B. Wang. Inter-phase interaction in a turbulent, vertical channel flow laden with heavy particles. Part I: Numerical methods and particle dispersion properties. *Int. J. Heat Mass Transfer*, 53(11):2506–2521, 2010.
- L. P. Wang and M. R. Maxey. Settling velocity and concentration distribution of heavy particles in homogeneous isotropic turbulence. *J. Fluid Mech.*, 256:27–68, 1993.
- L. P. Wang, A. S. Wexler, and Y. Zhou. On the collision rate of small particles in isotropic turbulence, Part I: Zero-inertia case. *Phys. Fluids*, 10:266–276, 1998.
- L. P. Wang, A. S. Wexler, and Y. Zhou. Statistical mechanical description and modelling of turbulent collision of inertial particles. *J. Fluid Mech.*, 415:117–153, 2000.
- M. Wang, C. Lin, and Q. Chen. Advanced turbulence models for predicting particle transport in enclosed environments. *Building and Environment*, 47:40–49, 2012.
- H. Werner. *Grobstruktursimulation der turbulenten Strömung über eine querliegende Rippe in einem Plattenkanal bei hoher Reynolds-Zahl*. PhD thesis, München, Techn. Univ., 1991.
- H. Werner and H. Wengle. Large-eddy simulation of turbulent flow around a cube in a plane channel. In F. Durst, R. Friedrich, B. E. Launder, U. Schumann, and J. H. Whitelaw, editors, *Selected Papers from the 8th Symposium on Turbulent Shear Flows*, pages 155–168. New York: Springer, 1993.
- C. M. Winkler, S. L. Rani, and S. P. Vanka. Preferential concentration of particles in a fully developed turbulent square duct flow. *Int. J. Multiphase Flow*, 30(1):27–50, 2004.
- X. Wu and P. Moin. A direct numerical simulation study on the mean velocity characteristics in turbulent pipe flow. *J. Fluid Mech.*, 608:81–112, 2008.
- D. Wunsch, P. Fede, and O. Simonin. Development and validation of a binary collision detection algorithm for polydispersed particle mixture. In *Proc. of FEDSM 2008, ASME Fluids Eng. Conf., Aug. 10–14, 2008, Jacksonville, Florida, USA*, 2008.
- M. Xu, J. Yuan, C. Han, and C. Zheng. Investigation of particle dynamics and pulverized coal combustion in a cavity bluff-body burner. *Fuel*, 74(12):1913–1917, 1995.
- Y. Yamamoto, M. Potthoff, T. Tanaka, T. Kajishima, and Y. Tsuji. Large-eddy simulation of turbulent gas-particle flow in a vertical channel: Effect of considering inter-particle collisions. *J. Fluid Mech.*, 442:303–334, 2001.
- J. Yao and M. Fairweather. Inertial particle resuspension in a turbulent, square duct flow. *Phys. Fluids*, 22:033303–1–033303–15, 2010.
- J. Young and A. Leeming. A theory of particle deposition in turbulent pipe flow. *J. Fluid Mech.*, 340:129–159, 1997.
- M. V. Zagarola and A. J. Smits. Mean-flow scaling of turbulent pipe flow. *J. Fluid Mech.*, 373:33–79, 1998.
- M. M. Zdravkovich. *Flow Around Circular Cylinders, Vol. 1: Fundamentals*. Oxford University Press, 1997.

- L. Zeng, S. Balachandar, and P. Fischer. Wall-induced forces on a rigid sphere at finite Reynolds number. *J. Fluid Mech.*, 536:1–25, 2005.
- H. Zhong, J. Gao, C. Xu, and X. Lan. CFD modeling the hydrodynamics of binary particle mixtures in bubbling fluidized beds: Effect of wall boundary condition. *Powder Technology*, 230:232–240, 2012.